Spatiotemporally Resolved Proteomics and Dynamic Biomaterial Control through Bioorthogonal Photochemistry

Steven M. Adelmund

A dissertation
submitted in partial fulfillment of the
requirements for the degree of

Doctor of Philosophy

University of Washington
2019

Reading Committee:
Cole A. DeForest, Chair
James Carothers
Shaoyi Jiang

Program Authorized to Offer Degree:
Chemical Engineering

University of Washington

Abstract

Spatiotemporally Resolved Proteomics and Dynamic Biomaterial Control
through Bioorthogonal Photochemistry

Steven M. Adelmund

Chair of the Supervisory Committee:
Cole A. DeForest
Department of Chemical Engineering

Biological processes are staggeringly dynamic and heterogeneous, exhibiting regular change across a variety of time and length scales. Though all cells within an organism share a common genome, differential expression of genes into proteins regulate developmental processes, tissue morphogenesis and function, disease susceptibility and response, and a wide variety of intra- and extra-cellular signaling events. This thesis introduces the first tools for spatiotemporally resolved proteomics, enabling visualization and quantification of proteins produced *in vitro* and *in vivo* within user-defined regions of time and 3D space (i.e., 4D). Light-activated bioorthogonal non-canonical amino acid tagging (laBONCAT) exploits the photouncaging of a reactive amino acid prior to translational incorporation, while photoactivated *in vitro*/*vivo* tagging (PAINT) utilizes light to spatially tag proteins that were previously metabolically labeled. In both cases, affinity purification and quantitative mass spectrometric analysis permits 4D mapping of global protein production within living samples. Relying on bioorthogonal photochemistries that can be performed on demand and with single-micron resolution, this work demonstrates the ability to label newly synthesized proteins in 2D/3D

culture and in zebrafish models with subcellular resolution. This unique approach is likely to prove useful in determining new diagnostic markers for disease, as well as expanding our knowledge of fundamental biology.

Recognizing the precise 4D control that photochemistry affords, this thesis further expands the toolbox of photochemical reactions available, creating biomaterials whose chemical and physical properties can be modulated in a wavelength-dependent manner. Here, a photoorthogonal reaction scheme is introduced that combines photocleavable linkers based on *ortho*-nitrobenzyl ester (*o*NB) and a boron-dipyrromethene (BODIPY) that respond to UV and visible light, respectively. *o*NB remains undisturbed under 505 nm irradiation, while BODIPY undergoes rapid photolysis. Although BODIPY also cleaves with 365 nm irradiation, its comparative slow degradation kinetics permit reaction orthogonality with *o*NB under physiological conditions. This pair permits on-demand and spatially defined regulation of protein presentation within and degradation of hydrogel biomaterials, providing exciting opportunities for controlled drug delivery and tissue engineering applications.

Table of Contents

List of Figures vii
List of Tables ix
Chapter 1. Introduction 1
1.1 The heterogeneous and dynamic nature of biology 1
1.2 Current techniques for proteomic sampling 3
1.3 Current stimuli-responsive biomaterials 9
Chapter 2. Light-activated BioOrthogonal Non-Canonical Amino acid Tagging (laBONCAT) 13
2.1 Photocaged azidohomoalanine 14
2.2 Uncaging kinetics of NPPOC-Aha 16
2.3 laBONCAT *in vitro* activation and fluorescent labeling 16
2.4 NPPOC-Aha *in vitro* stability 18
2.5 laBONCAT *in vitro* activation and protein isolation 19
2.6 laBONCAT *in vitro* spatial activation 21
Chapter 3. PhotoActivated *IN vitro/vivo* Tagging (PAINT) 23
3.1 Synthesis of the small molecule click, photo-probe 25
3.2 Method demonstration on an azide-functionalized slide 26
3.3 Method demonstration through *in vitro* activation and photopatterning 27
3.4 Image-guided photoactivation *in vitro* 31
3.5 Protein isolation by affinity column chromatography 33
3.6 Zebrafish: an ideal model organism 35
3.7 Transgenic zebrafish breeding overview 36
3.8 PAINT demonstration in zebrafish 38
3.9 Image-guided 3D photomask generation in zebrafish 42
Chapter 4. Orthogonal photochemistry for dynamic materials 48
4.1 Light as a tool for interacting with biology 49
4.2 Selecting candidates for a photoorthogonal system 50
4.3 Synthesis of a coumarin photocage precursor 52
4.4 Synthesis of a BODIPY photocage 53
4.5 Selective release of proteins from hydrogels 56
4.6 Orthogonal release of proteins from multicomponent hydrogels 59
4.7 Small molecule patterning *via* photorelease from multicomponent materials 60

4.8 Crosslinker generation and photo-rheology 60
4.9 BODIPY pH sensitivity 62
4.10 Apoptosis as a model system for sequential biochemical signaling 63
4.11 A second chance for coumarin 65
Chapter 5. Conclusions & Future Work 70
Appendix A Supplementary Information A.1
Appendix B MATLAB® Code for Photomask Generation B.1

List of Figures

Figure 1. Techniques for sampling the proteome 4
Figure 2. Light-activated bioorthogonal non-canonical amino acid tagging (laBONCAT) 14
Figure 3. Chemical structures and reaction diagrams 15
Figure 4. *In vitro* analysis of light-activated bioorthogonal non-canonical amino acid tagging (laBONCAT) 17
Figure 5. Isolation of protein by laBONCAT 19
Figure 6. Irradiation of photocaged L-azidohomoalanine (NPPOC-Aha) yields free Aha for ncAA *in vitro* incorporation 20
Figure 7. Schematic overview of PhotoActivated IN vitro/vivo tagging (PAINT) 24
Figure 8. Small molecule tools for subcellular labeling 26
Figure 9. Selective protein labeling *in vitro* 28
Figure 10. *In vitro* patterning of labeled proteins 29
Figure 11. Sequential patterning of labeled cells *in vitro* 30
Figure 12. Fluorescence-based photomask generation. 32
Figure 13. Image-guided photoactivation of mixed cell culture. 33
Figure 14. SDS-PAGE of selective protein labeling and isolation *in vitro* 34
Figure 15. Transgenic fish breeding overview. 37
Figure 16. Zebrafish labeling by PAINT using collimated light. 40
Figure 17. Zebrafish labeling by PAINT using two-photon activation. 41
Figure 18. Antibody comparison after BLAST analysis. 44
Figure 19. 3D Images of Flk1-GFP and anti-Flk1 immunostaining 45
Figure 20. Image-guided photomask generation in zebrafish. 46
Figure 21. An orthogonal photochemical reaction pair 55
Figure 22. Photopatterning of protein-coupled hydrogels 57
Figure 23. Selective release of fluorescent proteins from PEG-based hydrogels 58
Figure 24. Rheological characterization of BODIPY and *o*NB-crosslinked hydrogels 61
Figure 25. HeLa response to sequential treatment with EGF, TNF-α, and birinapant 64
Figure 26. Potential expansion of orthogonal photochemistry 66
Figure 27. Proposed structural improvements to laBONCAT 73
Figure A1. ^{1}H NMR of benzaldehyde-functionalized 4-arm PEG A.10
Figure A2. Figure S7. ^{1}H NMR of alkoxyamine-functionalized 4-arm PEG A.12

Figure A3. Uncaging kinetics of NPPOC-Aha A.13
Figure A4. Spatially labeled 3D tissue culture A.16
Figure A5. Isolation of proteins by laBONCAT A.18
Figure A6. Photopatterning on a glass slide A.28
Figure A7. Activation and fluorescent labeling of proteins by PAINT. A.30
Figure A8. Resolution of protein activation by 2P microscopy A.32
Figure A9. Background staining of image-guided photoactivation in mixed cell culture. A.32
Figure A10. Treatments to reduce background labeling. A.36
Figure A11. BLAST comparison of EGFP and GRCFP A.36
Figure A12. BLAST comparison of zsYellow and GRCFP. A.37
Figure A13. Absorbance shift of NH_2-tCM-OH upon installation of the azide at position 7 ..... A.37
Figure A14. Photopatterning of fluorescent small molecules A.46
Figure A15. Kinetic analysis of N_3-BODIPY-OSu under 365 and 505 nm irradiation A.47
Figure A16. Kinetic analysis of N_3-*o*NB-OSu under 365 and 505 nm irradiation A.49
Figure A17. UV-vis of photocages and photocaged coupled proteins A.51
Figure A18. Solution-based photocleavage of N_3-BODIPY-mCherry A.52
Figure A19. Gel photopatterning of N_3-BODIPY-mCherry A.53
Figure A20. Photobleaching of mCherry at 365 and 505 nm A.54
Figure A21. Photobleaching of mCerulean at 365 and 505 nm A.55
Figure A22. Multiple release of fluorescent proteins from PEG-based hydrogels A.57
Scheme 1. Synthesis of N_3-tCM-OH 53
Scheme 2. Synthesis of N_3-BODIPY-NHS 54
Scheme 3. Proposed synthetic route to N_3-DEAC-NHS 67
Scheme A1. Synthesis of NPPOC-Aha and NPPOC-NO-NHS A.4
Scheme A2. Synthesis of BCN-NHS. A.19
Scheme A3. Synthesis of the heterobifunctional probe (NPPOC-NO-BCN) A.22
Scheme A4. Synthesis of L-azidohomoalanine A.24

List of Tables

Table 1. Genetic makeup of transgenic zebrafish lines 38
Table 2. Photochemical properties of select photocages 52
Table 3. Coumarin Heck coupling conditions 69
Table A1. Photokinetic properties of *o*NB and BODIPY A.50

Acknowledgements

John Donne wrote, “No man is an Iland, intire of itselfe” and that is especially true of scientific work. The accomplishments presented here were only possible through the concerted effort of a group of talented researchers that I had the honor of working alongside. With sincere gratitude I want to extend my thanks to Koichiro Uto, whose tireless synthetic efforts made all the BODIPY work possible; Payam Farahani who lent his expertise to the rheological characterization of these materials; Sebastian Kurniawan who worked tirelessly to make a coumarin-based photocage; Ivan Batalov who developed MATLAB® scripts that convert biological images into photomasks; and Emily Ruskowitz who proved invaluable in the isolation of activated proteins from complex lysate. Thanks to Barry Badeau for synthesizing and supplying N_3-*o*NB-NHS and Jared Shadish for providing fluorescent proteins and azide-functionalized slides. Thank you to Jeanot Muster and Stan Kim from the ISCRM aquatics core for patiently training me on zebrafish husbandry. Thank you, Dale Hailey, for lending your expertise with both two-photon microscopy and zebrafish handling. Another thanks is due to Dr. Cole DeForest for always having confidence in my abilities, even when I doubted myself. His unending patience and continuing support for my crazy ideas is the reason this work sits before you now. I want to extend my gratitude to my family for their patience as I followed my path through science. And I want to thank my wife. Without her support none of this would have been possible.

Dedication

This dissertation is dedicated to the love of my life, Tessa Adelmund. Her constant encouragement and support made this work possible.

Chapter 1. Introduction

When once it appeared that the decoding of the human genome would unlock the mysteries of biology[1], it has become increasingly clear that more information is necessary to truly understand the biological state of a system. An organism's genome provides a template for the potential RNA and protein the system can produce but communicates only one part of a complex state. Taken alone, each component of the system (DNA, RNA, and protein) provide an incomplete representation of the overall system. Though all cells within an organism share a common genome, differential expression of genes into proteins regulate developmental processes, tissue morphogenesis and function, disease susceptibility and response, and a diverse array of signaling events governed by a wide variety of intra- and extra-cellular cues. While each protein is encoded by a gene, protein quantity and activity cannot be determined through genomic or transcriptomic analysis[2,3]; such techniques are blind to post-transcriptional phenomena (*e.g.*, translational regulation, modification, protein-biomolecular interactions). Proteins represent the ultimate expression of the genome, provide crucial regulatory and structural support for the cell, and comprise roughly 50% of dry cellular composition[4]. Taken together, these emphasize the necessity of developing strategies that directly measure protein identity and abundance[5] and materials that are capable of recapitulating a degree of the complexity that we find.

1.1 The heterogeneous and dynamic nature of biology

From mitosis, to embryonic development[6,7], to disease[8–14], the dynamic and heterogeneous nature of biology is ubiquitous. Proper subcellular localization of proteins is essential in ensuring desired function, including signaling, interactions, or complexing. Misplaced proteins may indicate alternative function or disease by inclusion or omission[15,16].

Parkinson's disease (PD) and Alzheimer's disease (AD) are diseases of protein malfunction and both result in heterogeneous protein aggregation in the brain. AD is characterized by extracellular β-amyloid aggregation and tau hyper-phosphorylation resulting in neurite retraction and eventually neuronal death. In PD, α-synuclein aggregates inside neurons and is isolated to form a Lewy body inclusion. Despite the identification of several associated genes, little is known about the biochemical progression that give rise to PD[17,18] and AD[19,20]. The lack of biochemical understanding of the underpinnings of these diseases make them difficult to diagnose and treat. There is no cure; diagnoses and treatments are purely symptomatic. These diseases affect a large portion of the population and place a large financial burden through the cost of medical care. Combined treatment for these diseases costs over $280 billion in the US during 2017, and affect 1 in 6 Americans with 1 in 3 elderly Americans dying from dementia each year[21]. Developing a deeper understanding of these diseases alone has the potential to help millions of people through improved diagnoses and treatments.

Cancer is another disease that has a large societal impact[22] and is well known for its heterogeneity. Tumors are often mutagenic and display clear disparate features. Efforts to sequence tumors with the intention to identify more effective treatment options, while well intentioned, have produced mixed results[23–25]. These efforts ignore the fact that the genome is only one part of a complex and heterogeneous biochemical system. A better approach would be to categorize cancer type based on the proteins or biomolecules localized to certain areas and identify treatments that are likely to be effective from that analysis. The best approach will likely pair proteomic and genomic analysis to provide the most accurate picture of the state of disease and provide treatment accordingly.

These examples clearly highlight the important fact that biology is heterogeneous and dynamic. To develop a deeper understanding of biology, we need tools that are capable of sampling in a way that can productively probe biological samples in any area of interest for a given interval. Recent advances in mass spectrometry and genomic sequencing have enabled high-throughput proteomic analysis, whereby the abundance, turnover, modification, and interactions of thousands of proteins can be measured in minutes[26,27]. From this has emerged a growing appreciation of the exceptionally dynamic nature of the proteome, which undergoes large-scale biochemical shifts. Understanding this complexity will further the goal of addressing disease and realizing the promise of regenerative medicine, and this work makes a significant contribution towards those aims.

1.2 Current techniques for proteomic sampling

Techniques for sampling the proteome fall into two broad categories and, with the exception of whole proteome sampling[28], their purpose is to reduce sample complexity so that the signals of interest can shine through and be analyzed (Figure 1). The first broad category is label-free proteomics. This includes sampling of the entire proteome/secretome, organelle separation by sucrose density gradient[29,30], or by the sampling of proteins from fixed samples[13,31]. It is important to note that the use of fusion proteins is limited to a handful of proteins simultaneously and is not considered proteomics here, and that coupling of proteins in this way can alter their function and localization[32]. While each of these techniques has proved useful in uncovering some information about the biological state or condition, they all have clear deficiencies.

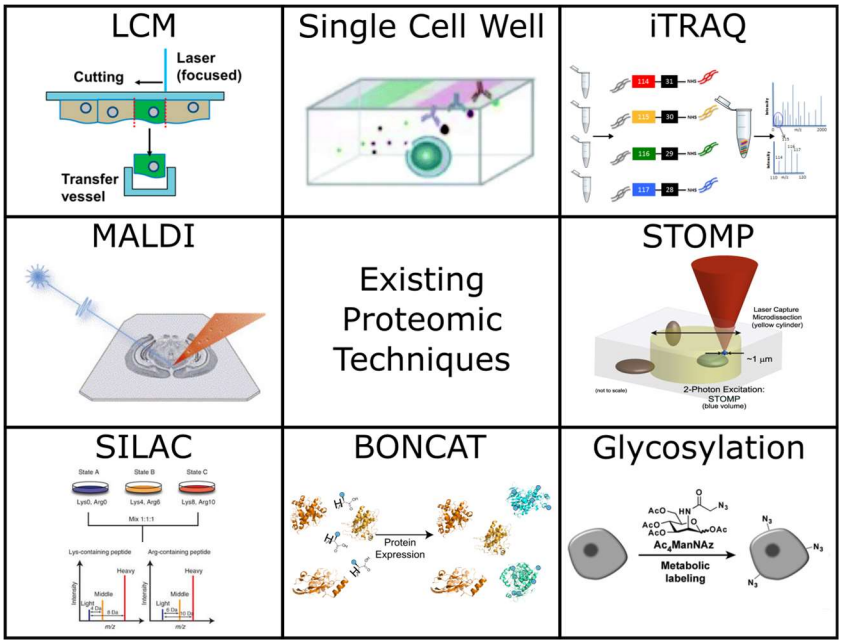

Figure 1. Techniques for sampling the proteome. Laser capture microdissection[33] (LCM) and single cell wells[34] can isolate individual cells for analysis. Isobaric tag for relative and absolute quantitation[35] (iTRAQ) uses tags for multiplexing of proteins in mass spectrometry. Matrix assisted laser desorption ionization[36] (MALDI) provides spatial resolution under mass spectrometry for samples from tissue culture. Spatially targeted optical microproteomics[13] (STOMP) uses two-photon excitation to activate a small molecule in fixed tissue to isolate proteins. Stable isotope labeling with amino acids in cell culture[37] (SILAC) labels newly synthesized proteins with heavy isotopes of canonical amino acids that can be differentiated during analysis. Bioorthogonal non-canonical amino acid tagging (BONCAT) labels newly synthesized proteins with useful functionality that is used for isolation or visualization. Glycosylation of proteins with azide-functionalized sugars[38] provides insight into a subset of protein interactions. Current techniques interrogate biological systems with temporal or spatial control, but not both.

The analysis of the whole proteome can provide some insight into biological processes, but since some proteins may be expressed in high number due to their function for generic housekeeping or structure, their inclusion in analysis has the potential to drown out other signals. This necessitates the separation of proteins in some way, and, as expected, much of the recent work in the field has utilized at least one form of protein isolation.

The use of sucrose gradients is one label-free method for isolating a subset of proteins based on their subcellular location in organelles. Typically, this work is limited to a handful of intercellular structures that can be isolated[29,39] and those gradients produce significant elution overlap[40], indicative of potential contamination. In addition, the field suffers from the fallacy of identifying proteins as organelle-specific, when proteins operate on a much more fluid basis with respect to their subcellular localization. This approach loses sight of the periphery; proteins near but outside an organelle may be lost and with it important information about the biological state. Knowing which proteins are localized to different organelles is valuable information, but at least as valuable is understanding the interactions taking place at those interfaces.

The most interesting of label-free proteomics methods are capable of physically removing material (e.g., tissue, cells, protein) from a sample for analysis. This work is exciting for its efforts to push the boundaries on the spatial resolution for protein sampling. This ranges from macroscopic organ dissection[41,42] to matrix assisted laser desorption ionization (MALDI) of protein from fixed samples with high resolution[43,44]. Laser capture microdissection (LCM) can pluck individual cells out of a culture and analyze their proteome[31,45]. It is possible to achieve a similar goal by culturing cells in separate channels, making it easier to isolate them for analysis[34,46], but this method removes the cell from native environmental signals, making the drawing of broad conclusions dubious. Of course, going from organs to organelles represents a

huge range in scale. Nanostructure-initiator mass spectrometry (NIMS) has dramatically improved upon the spatial resolution of MALDI using molecules that initiate ionization trapped in a clathrates matrix[47]. Since it is simply ejecting molecules from a substrate, NIMS can extend to the detection of biomolecules other than proteins (e.g., sugars, steroids)[48]. Although the spatial resolution of these approaches is impressive, they all fundamentally lack the ability to sample proteome response temporally, since the proteins identified from the sample are a mixture of all preceding states.

Proteome labeling, as an alternative to label-free proteomics, has several distinct manifestations and are often used in combination with the techniques described above to provide additional control (spatial or temporal) or signal reduction. Thiols are a special case in protein labeling, because their state provides information about the structure and activity of the protein. As nucleophiles they can be easily isolated from lysate[49], and applying iodoacetamide to cap free thiols followed by reducing conditions and labeling, the state of each thiol on a protein can be elucidated[50,51]. Although this technique is extremely powerful for these specific circumstances it is difficult to generalize to study other interactions. Likewise, biotinylation of organelles[52] or membranes[53] is a useful tool for exploring a limited subset of the proteome through specific interactions.

The use of isotopic labeling of proteins has generalized the tagging approach and has expanded dramatically in the last decade. Isotope-coded affinity tag (ICAT) labels amino acid side chains (Lys, Cys, Glu, and Asp) with tags that differentiate between labeled and unlabeled proteins when analyzed by MS. This allows for two samples to be analyzed simultaneously and the relative ratio for each expressed protein can be determined. A significant improvement on this process, isobaric tag for relative and absolute quantitation (iTRAQ), modifies the same side

chains, but the use of multiple linkers that result in known mass shifts, allows for the multiplexing of up to 8 different samples[54], increasing the complexity of possible experiments while simultaneously simplifying their analysis. Since these methods are applied post-lysis, all proteins in the sample are labeled even those present before the stimulus under study, effectively treating the sample as homogeneous. This has the potential to include signals that are irrelevant to the analysis, and fundamentally lacks temporal resolution.

Metabolic labeling, by the incorporation of specialized amino acids or sugars, has the advantage of being inherently temporal by labeling the proteome over a given time interval. It should be noted that the addition of external chemicals has the potential for perturbation of the proteome and must be taken with great care. Any chemical, including naturally occurring or native, might elicit a response and should be compared against proper controls wherever possible. Stable isotope labeling with amino acids in cell culture (SILAC) involves the use of isotopic amino acids that are heavy versions of their natural counterparts[55,56]. Since the substitutions are heavy isotopes of natural amino acids, their impact is assumed to be negligible. In addition, variations on isotopically labeled amino acids allows for post-lysis sample mixing and multiplexing, saving time and allowing for relative quantitation similar to iTRAQ.

Cell-surface glycoproteins have also been metabolically labeled by azide-containing sugars for visualization and proteomic analysis[38,57]. This method is more specific than amino acid incorporation, since it labels only glycosylated cell-surface proteins, and it monitors a different temporal space than other proteomic systems, specifically focusing on glycosylation. This is advantageous for probing only these interactions, removing extraneous proteins from analysis, but lacks the ability to be generalized.

One particularly powerful method for interrogating proteomic fluctuations in culture is known as bioorthogonal non-canonical amino acid tagging (BONCAT). In BONCAT, non-canonical amino acids (ncAA) are substitutions that are metabolically incorporated into newly synthesized proteins. The ncAAs are distinct from the naturally occurring 20 or so amino acids but are structurally similar to methionine (Met), such that they leverage the permissivity of the methionine aminoacyl-tRNA synthetases (aaRS) and are loaded onto the tRNA. In many cases it is useful to introduce chemical functionality through ncAA incorporation that can later be exploited. The most common of these are azidohomoalanine (Aha), homopropargylglycine (Hpg), and homoallylglycine (Hag)[58,59]. Pulsing cells with these ncAAs yields newly synthesized proteins that bear bioorthogonal reactive groups [60–62]. Metabolically labeled proteins can be covalently modified with an affinity tag that is then exploited for purification[63]. Installation of the azide group, for example, on the side chain of Aha into new proteins provides a unique bioorthogonal handle that can be captured via Staudinger [64] or the copper-catalyzed azide-alkyne cycloaddition (CuAAC)[65,66] ligations or the more recent strain-promoted azide-alkyne cycloaddition (SPAAC) reaction[38,67]. In most biological systems SPAAC is preferred due to its rapid[68] condensation and the relatively toxic conditions of Staudinger and CuAAC reactions. These reactions enable isolation of proteins synthesized over a short window of time and providing temporally resolved proteomics.

It is possible to extend the use of ncAAs further through the use of genetically engineered aaRSs to substitute ncAAs of choice into the position of any naturally occurring amino acid[69,70]. This must be done with great care to maintain cellular function without altering protein homeostasis. This idea could theoretically be expanded even further to the inclusion of 40 or more ncAAs which could be installed any desired position on one or more proteins, by breaking

codon redundancy[71] through the use of engineered tRNAs and/or aaRS. Although this could be a huge boon to proteomics, permitting vast multiplexing, it is hard to image how this could be done without a significant impact on the proteome not to mention the lack of supporting, orthogonal and bioorthogonal chemistries.

Many of the current techniques for sampling the proteome are described above. While each method is valuable, they all have shortcomings in one form or another; be that lacking spatial or temporal control, treating tissue culture as homogeneous, or being so specific that the technique cannot be generalized. These shortcomings highlight the need for a tool that can sample anywhere at user defined locations and times.

Inspired by the broad applicability and unobtrusive nature of metabolic Aha incorporation[72], we thought that a combination of ncAA labeling and light-activated photocages[73] would prove useful as a tool to probe the dynamic and heterogeneous nature of the proteome. The results of this hypothesis are two techniques for spatial and temporal proteome labeling, highlighted in Chapters 2 and 3 of this thesis.

1.3 Current stimuli-responsive biomaterials

The complexity of biology necessitates the development of increasingly complex materials that mimic the complexity found in a biological environment. If the dream of regenerative medicine is to be realized, it is essential that materials are developed that are capable of responding dynamically through user-defined inputs. From an engineering perspective, biology can be thought of as an incredibly complex control system using temperature, pH, stiffness, salinity, oxidative environment, and biochemical/biophysical cues. A few properly timed signaling cues

could place the system on a trajectory toward the desired outcome[6,7,74]. More biologically relevant materials will undoubtedly include multiple orthogonal cues so that stimuli can be introduced independently and reversibly. For some cues, complete spatiotemporal control will be essential.

Remarkable progress has recently been made with the introduction of a logic-based approach where crosslinkers are constructed from simple cleavable moieties to generate complex responses from multiple inputs including reductant, enzyme, and light[75]. Two different stimuli-responsive functionalities can be combined in series into a single crosslinker, such that only one is required to degrade the material, or in parallel where treatment with both stimuli is required to elicit degradation, but both are necessary. Using three independent stimuli, a total of 17 different responsive crosslinkers are possible. This level of complexity is necessary and likely to increase with time so that biomaterials can be tailored to meet the specific, dynamic, and heterogeneous requirements to imitate biology.

Light as a stimulus has many benefits in the arena of stimuli-responsive biology and biological sampling. It allows researchers to dictate the timing, location, and extent of the stimulus under investigation by controlling the duration, area, and intensity of light exposure. Molecular switches[76–78] might seem like a natural fit for biomaterials with the ability to propagate changes from the molecular level to the macroscopic, and in reverse, on demand and with spatial precision. Adoption of these motifs into the biomaterials space has been sluggish. The most prominent, but still relatively limited, example of these is the azobenzene[79] functional group that undergoes a *trans-cis* conformational change upon exposure to UV light (365 nm) and the reverse by blue light (445 nm) or through thermal relaxation[77,80]. Azobenzene has seen use in both 2D[81,82] and 3D[83–85] cell culture platforms. The primary reasons why these switches have not

seen more widespread application are likely due to cytotoxic wavelengths, photo-side products that render the switch inoperable, or the difficulty of propagating miniscule chemical changes to a biologically relevant scale. Biology is a harsh mistress, imposing a challenging environment on any chemistry operating within its domain. It is not too surprising that the introduction of these highly promising chemistries has lagged.

Far more prevalent are molecular photocages, or photolabile groups, that are used to mask function or serve as a crosslinker in materials. Though these are often used as a single input and response, there have been few examples[73,86] of combinatorial use of multiple photolabile groups together. Often these systems operate in a serial fashion where photocages must be removed in a specific order, severely limiting the biochemical topography of the material. For example, a material with 4 orthogonal inputs possesses a total of 16 possible outcomes. If instead the cages must be removed in a serial fashion, only five outcomes are possible. The current best example for orthogonal photocleavage from a biomaterial results in nearly 30% non-selective release[87], providing ample room for improvement.

An improved wavelength-orthogonal system would facilitate more precise control over a biomaterial platform. That is a system where two photosensitive molecules are used simultaneously in a material while maintaining selectively by controlling the wavelength of light used. If two photo-sensitive molecules could be synthesized with significantly different absorption maxima, then, in theory, they could be cleaved using two different wavelengths of light. This would provide a unique and flexible system capable of delivering unprecedent level of control over 4D tissue culture. Such a system is examined in Chapter 4 of this thesis.

In this thesis we will first explore the use of photochemistry and bioorthogonal chemistry for spatially-defined sampling of the metabolically labeled proteome both *in vitro* and *in vivo*.

Next, we will investigate the combination of two photolabile groups for the construction of a wavelength photoorthogonal system for spatial control over biomaterials.

Chapter 2. Light-activated BioOrthogonal Non-Canonical Amino acid Tagging (laBONCAT) (as published in ACS Chemical Biology, 2018[88])

The first technique was inspired by the permissivity of the methionine tRNA synthetase. Although the enzyme is remarkable tolerant to alternative sidechains[59], it was hypothesized that modifying an amino acid at the α-amine would prevent its inclusion in newly synthesized proteins. As protein expression, degradation, translocation, and post-translational modification occur at different rates depending on cellular and subcellular location within tissues[89], we sought to control BONCAT within user-defined regions of culture. Recognizing light's unique ability to initiate chemical reactions at a time and place of interest, this method is a modification to BONCAT termed light-activated BONCAT (laBONCAT) that enables the selective labeling, isolation, and identification of newly synthesized proteins at user-defined regions in tissue culture (Figure 2). By photocaging L-azidohomoalanine (Aha), metabolic incorporation into proteins is prevented. The caged compound remains stable for many hours in culture but can be photochemically liberated rapidly and on demand with spatial control. Upon directed light exposure, the uncaged amino acid is available for local translation, enabling downstream proteomic interrogation *via* bioorthogonal conjugation. Exploiting the reactive azide moiety present on Aha's amino acid side chain, we demonstrate that newly synthesized proteins can be purified for quantitative proteomics or visualized in synthetic tissues with a new level of spatiotemporal control. Shedding light on when and where proteins are translated within living samples.

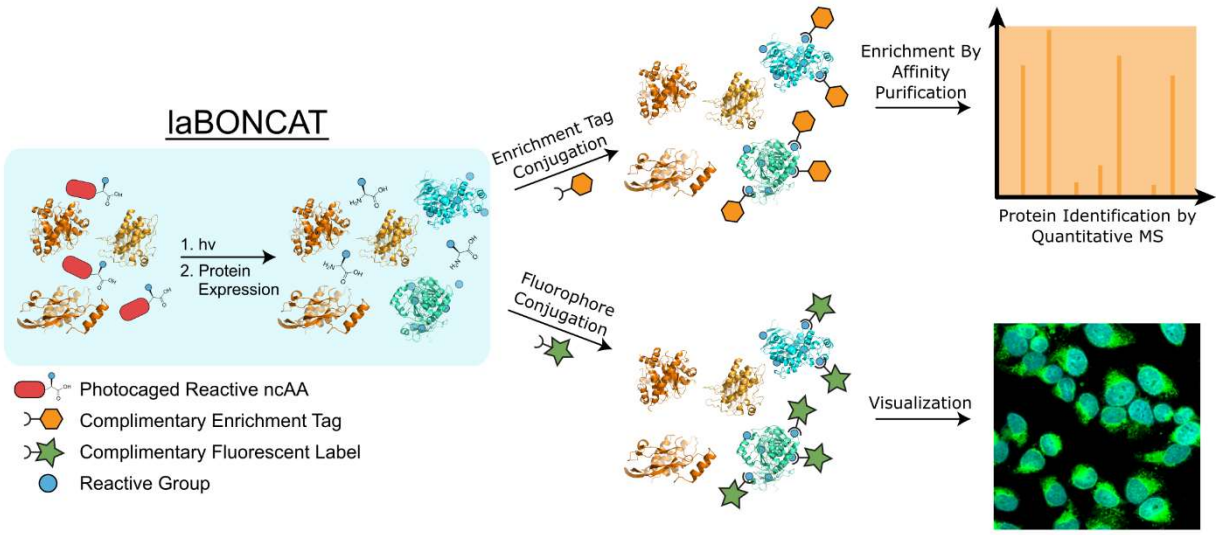

Figure 2. Light-activated bioorthogonal non-canonical amino acid tagging (laBONCAT). Photocaged non-canonical amino acids (ncAA) become available for stochastic incorporation into newly translated proteins following directed light exposure. Bioorthogonal handles installed by ncAAs can be exploited for protein purification prior to quantitative proteomics or fluorescent tagging for visualization.

While laBONCAT methodologies can be theoretically applied to any amino acid (including stable isotopes of natural amino acids, ncAAs, and other variants useful for quantitative proteomics), the first demonstration its utility was conducted with L-Azidohomoalanine (Aha).

2.1 Photocaged azidohomoalanine

Aha is an azide-bearing ncAA that is metabolically incorporated by endogenous cellular machinery as a methionine (Met) surrogate[58,90,91] whose low-level incorporation does not significantly alter protein expression[72,92] (Figure 3a). Aha's azido functionality represents a

useful bioorthogonal handle for subsequent labeling reactions, including the strain-promoted azide-alkyne cycloaddition[38] (SPAAC) (Figure 3b). We synthesized a photocaged Aha (NPPOC-Aha) through condensation of the α-amine of Aha[93] with the activated ester of 2,5-dioxopyrrolidin-1-yl (2-(2-nitrophenyl)propyl) carbonate[94] (NPPOC). As NPPOC-caged amines undergo irreversible β-elimination upon exposure to near-ultraviolet light[94] (λ = 365 nm; Figure 3c), Aha can be photochemically generated *in situ* in response to mild and cytocompatible light exposure[94–98]. This is the first example of an amino acid (canonical or otherwise) that has been photocaged at its N-terminus to prevent translation.

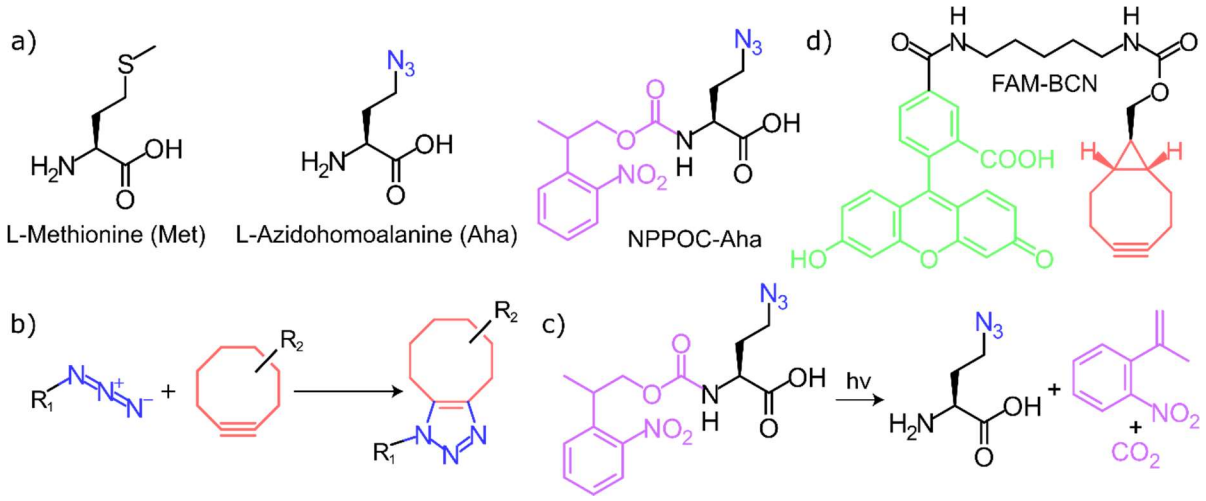

Figure 3. Chemical structures and reaction diagrams. (a) Structures of L-methionine (Met), L-azidohomoalanine (Aha), and photocaged Aha (NPPOC-Aha). (b) SPAAC is a bioorthogonal reaction for labeling azides incorporated into proteins with strained cyclooctynes. (c) Upon light exposure, photolysis of NPPOC-Aha yields free Aha for incorporation into newly synthesized proteins. (d) A carboxyfluorescein-labeled bicyclononyne (FAM-BCN) provides a fluorescent tag for labeling azide-functionalized proteins.

2.2 Uncaging kinetics of NPPOC-Aha

For this system to be effective, the kinetics of NPPOC uncaging should be rapid, such that the liberation of free Aha is not rate limiting compared with the biological processes under study. To determine its photolysis kinetics, NPPOC-Aha (in H_2O:CH_3CN, 50:50) was irradiated with collimated UV light[94] (λ = 365 nm, 10 mW cm^{-2}, 0 – 600 s exposure). Degradation products were quantitatively analyzed by HPLC, with elution fractions compositionally identified by mass spectrometry. A first-order decay constant of 0.0075 ± 0.0002 s^{-1} was observed for NPPOC photolysis (Figure A3); 90% of the NPPOC cleaved after 5 minutes of mild irradiation (10 mW cm^{-2}), a timescale suitable for many biological applications.

2.3 laBONCAT *in vitro* activation and fluorescent labeling

To demonstrate photomediated incorporation of Aha, Met-depleted HeLa cells were incubated with NPPOC-Aha (250 μM). Subsequent irradiation with UV light (λ = 365 nm, 10 mW cm^{-2}, 5 min) yielded photoliberated Aha for metabolic incorporation. Two hours after light exposure, cells were lysed and their proteins were treated with a bicyclononyne-modified fluorescein (FAM-BCN, 100 nM, Figure 3d) to introduce a fluorescent label by SPAAC. Protein fluorescence was then used to quantify the extent of Aha incorporation following protein separation by sodium dodecyl sulfate polyacrylamide gel electrophoresis (SDS-PAGE). Non-irradiated samples and the Met control exhibited a similar lack of fluorescence; the UV-treated NPPOC-Aha and Aha control displayed significant fluorescent enhancement (Figure 4a), indicating successful implementation of laBONCAT.

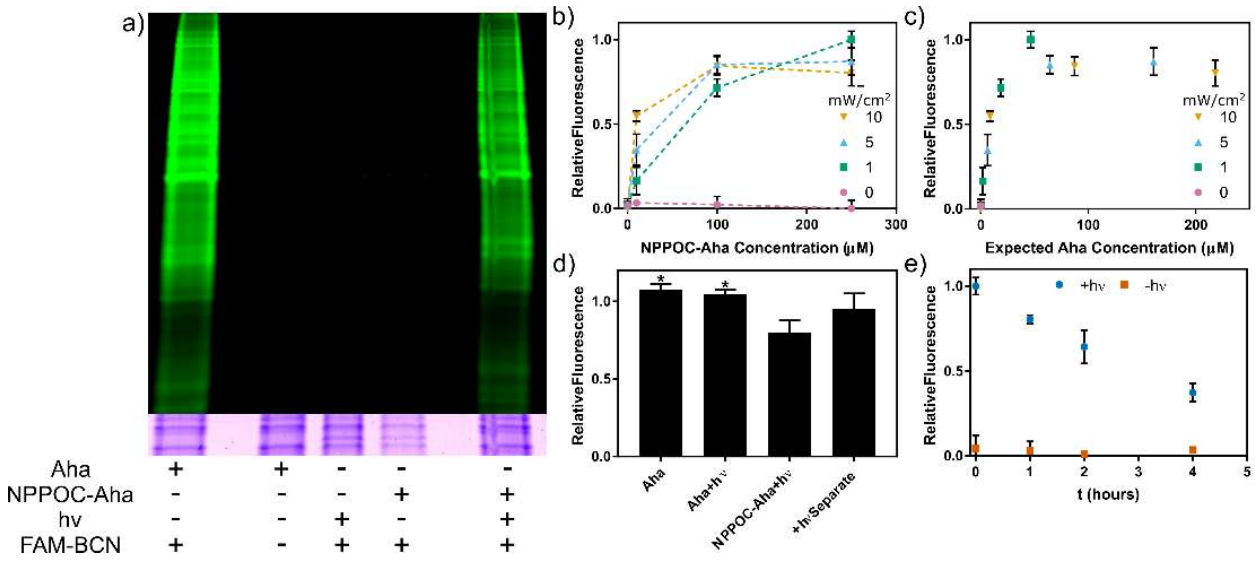

Figure 4. *In vitro* analysis of light-activated bioorthogonal non-canonical amino acid tagging (laBONCAT), stability, and isolation. (a) Analysis of fluorescently labeled protein lysate by SDS-PAGE. *In vitro* incorporation of free L-azidohomoalanine (Aha) and Aha after photoliberation provides azide-functionalized proteins for fluorescent tagging by carboxyfluorescein-labeled bicyclononyne (FAM-BCN). Only samples incubated with free Aha or light-treated photocaged Aha (NPPOC-Aha) are fluorescently labeled. Coomassie staining indicates near-uniform protein loading. (b) The effect of light intensity and NPPOC-Aha concentration on azide incorporation into newly synthesized proteins was investigated, based on protein fluorescence. (c) The degree of incorporation from part b normalized for expected free Aha concentration. (d) Light irradiation itself does not impact ncAA incorporation of Aha (*$p<0.05$ by one-way ANOVA followed by Tukey's test). (e) A significant amount of NPPOC-Aha remains stable over several hours in media and in contact with live cells suitable for labeling new proteins in tissue culture.

To control the extent of ncAA incorporation into newly synthesized proteins, we varied NPPOC-Aha concentration (0 – 250 μM) and the intensity of light irradiation (0 – 10 mW cm^{-2}) employed during photo-uncaging. As expected, Aha incorporation increased with NPPOC-Aha

concentration for a given exposure condition; for low NPPOC-Aha concentrations, metabolic labeling increased with light intensity (Figure 4b). When the extent of incorporation was normalized for the expected concentration of liberated Aha, based on values predicted by the photokinetics and assuming no side reactions accompanying photolysis, the result was a smooth, continuous curve that plateaus above ~50 μM free Aha (Figure 4c). To determine the potential effects of UV irradiation on metabolic incorporation, labeled protein fluorescence was compared for samples treated with Aha (50 μM) +/– light (10 mW cm^{-2}, 5 min) (Figure 4d). Finding no statistical difference in protein labeling following UV irradiation, we compared incorporation between Aha and irradiated NPPOC-Aha cultures (each at 100 μM). NPPOC-Aha + light gave rise to slightly less incorporation than Aha alone, which we attribute to incomplete photoconversion of NPPOC-Aha to Aha. This is supported by data that protein labeling does not depend on whether NPPOC-Aha is irradiated separately or during incubation with cells (Figure 4d).

2.4 NPPOC-Aha *in vitro* stability

To assess its *in vitro* stability, NPPOC-Aha (100 μM) was incubated in media with HeLa cells for 0 – 4 hr prior to light exposure (10 mW cm^{-2}, 5 min) and subsequent metabolic labeling (2 hr). Aha incorporation was observed for all irradiated samples, though its extent decreased over time. This was attributed to unknown cellular processing of NPPOC-Aha; simple hydrolysis yielding free Aha does not explain this behavior, as non-irradiated samples do not show increased incorporation over time. While the >4 hours of working time is likely sufficient for many applications, we anticipate that different photocages and/or ncAAs may exhibit increased

long-term stability. Such stability is useful in sampling biological systems, as it decouples media swaps from proteome labeling, allowing researchers to standardize their experimental conditions.

2.5 laBONCAT *in vitro* activation and protein isolation

After demonstrating the ability to label newly synthesized proteins, we sought to extend the laBONCAT methodologies to their affinity purification. After NPPOC-Aha uncaging and metabolic incorporation of the ncAA, proteins were biotinylated *via* SPAAC with a dibenzocyclooctyne-modified biotin probe. Biotinylated proteins were captured on a streptavidin resin prior to protein elution by streptavidin denaturation. Eluents were subjected to SDS-PAGE and silver stained for visualization (Figure 5). Results highlight the capability to selectively isolate newly synthesized proteins from irradiated samples.

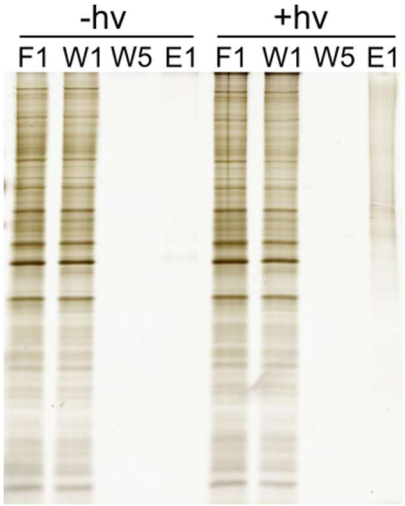

Figure 5. Isolation of protein by laBONCAT. Following photomediated Aha incorporation, newly synthesized proteins can be isolated by affinity purification for downstream proteomic analysis. Fractions from left to right: flow through 1 (F1), wash 1-5 (W1-5), and elution 1 (E1).

Building on the capability to fluorescently tag cellular lysates as well as isolate species of interest *via* laBONCAT, the technique's unique ability to label newly synthesized proteins *in vitro* with spatial control was explored; it is anticipated that this method could be applied to the isolation of proteins transcribed at user-specified times and locations from heterogeneous features in tissue culture, especially tissue slices. HeLa cells were treated with NPPOC-Aha (100 μM) and exposed to light (λ = 365 nm, 10 mW cm^{-2}, 5 min). Two hours after exposure, cells were fixed, permeabilized, and treated with FAM-BCN (100 nM) to introduce a fluorescent label *via* SPAAC. The extent of fluorescent labeling of cells treated in this method was similar to free Aha, while NPPOC-Aha in the absence of light exhibited low-level labeling similar to Met (Figure 6a).

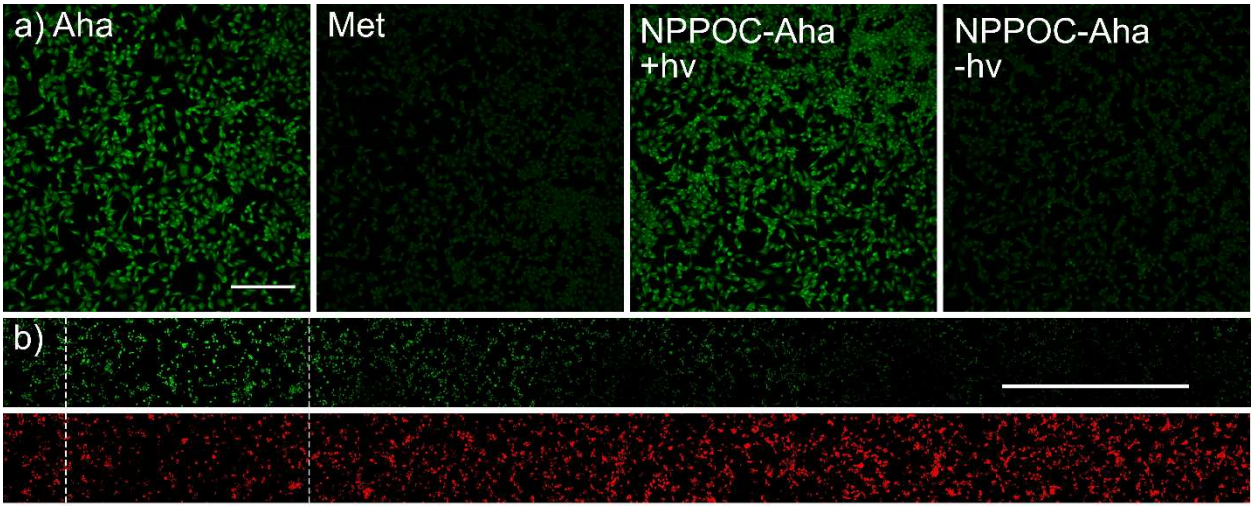

Figure 6. Irradiation of photocaged L-azidohomoalanine (NPPOC-Aha) yields free Aha for ncAA *in vitro* incorporation. (a) Fluorescent tagging of fixed cells demonstrates similar fluorescent labeling (green) of Aha and irradiated NPPOC-Aha, but not L-methionine (Met) and unexposed NPPOC-Aha. (scale bar = 100 μM). (b) Metabolic labeling of cells in synthetic tissue is confined to regions near

user-defined exposure (hashed area). Actin staining (red) remains uniform across sample (scale bar = 1 mm).

2.6 laBONCAT *in vitro* spatial activation

Next, we demonstrated the ability to control Aha incorporation spatially within synthetic tissues. Cells were encapsulated in oxime-based poly(ethylene glycol) hydrogels (7 wt%), treated with NPPOC-Aha and selectively irradiated through a slitted photomask. Cells were fixed and fluorescently labeled with FAM-BCN, phalloidin, and Hoechst. The observed cellular FAM signal was localized near exposed regions, corresponding to patterned Aha incorporation. FAM fluorescence decreased exponentially away from exposed regions in a diffusion-predicted manner (Figure 6). Actin and DNA staining lack substantial patterning (Figure A4).

This technique provides an inherent improvement to traditional BONCAT by allowing for precise timing in metabolic incorporation. In addition, the photochemical nature of the system provides a degree of spatial control for the investigation of heterogeneous biological systems. While not the focus of this manuscript, we anticipate that laBONCAT could be readily combined with strategies for pulsed stable isotope labeling by amino acids in cell culture[99] (pSILAC) to purify, identify, and quantify proteins expressed at user-defined regions in culture. This newfound ability is expected to prove particularly useful in the investigation of heterogeneous protein-related disease (e.g., Alzheimer's), potentially yielding new diagnostic markers and therapeutic targets. While the method has been initially validated using NPPOC-Aha responsive to near-UV light, facile extension of the technique to control incorporation of different amino acids using different photocage/light combinations is expected.

While this strategy demonstrates unique promise towards the visualization and characterization of newly synthesized proteins at user-defined time and places of interest, blocking the α-amine of the amino acid results in a negatively charged molecule. Since the cellular membrane bears a slightly negative charge, and the photocaged-Aha is no longer actively transported into the cell, it is hypothesized that the molecule remains in the extracellular space until it has been liberated, which was supported by subsequent experiments. When cells were treated with NPPOC-aha then rinsed before irradiation no significant labeling was observed. Further, when Aha was coupled to a fluorescent coumarin molecule, no intercellular fluorescence was observed, while the coumarin dye on its own did produce significant cellular staining (data not shown). Several alternative systems were devised to circumvent this issue. For example, the carboxylate could be masked with an ester that is selectively cleaved inside the cell[100], or the masked ncAA could be coupled to a cell penetrating peptide[101,102]. Nevertheless, since this technique relies on preventing the metabolic incorporation of the ncAA, the resolution of any improvement based in this method can be no better than single cell under most conditions. While other improvements to laBONCAT will be discussed later, a promising alternative was developed using a small-molecule, heterobifunctional probe.

Chapter 3. PhotoActivated *IN vitro/vivo* Tagging (PAINT)

Instead of photocaging the amino acid, as in the previous experiments, a heterobifunctional probe with a bicyclononyne (BCN) on one side and a photocaged hydroxylamine on the other could be used to label azide-containing proteins. The hydroxylamine can be subsequently liberated upon exposure to tissue culture-compatible light (λ = 365 nm)[103]. This strategy decouples the photo-uncaging event from metabolic labeling, permitting improved resolution. Since light is used as the trigger for uncaging, the resolution is theoretically limited only by the instrument and the diffraction wavelength of light. Proteins containing the activated probe are biotinylated through an oxime coupling to a biotin-benzaldehyde and then immobilized on a streptavidin-bound resin. Since inactivated proteins do not have an exposed hydroxylamine, they are not biotinylated and flow through the column. The retained proteins would then be selectively eluted by denaturing streptavidin, and can be subjected to tandem mass spectrometry (Figure 7).

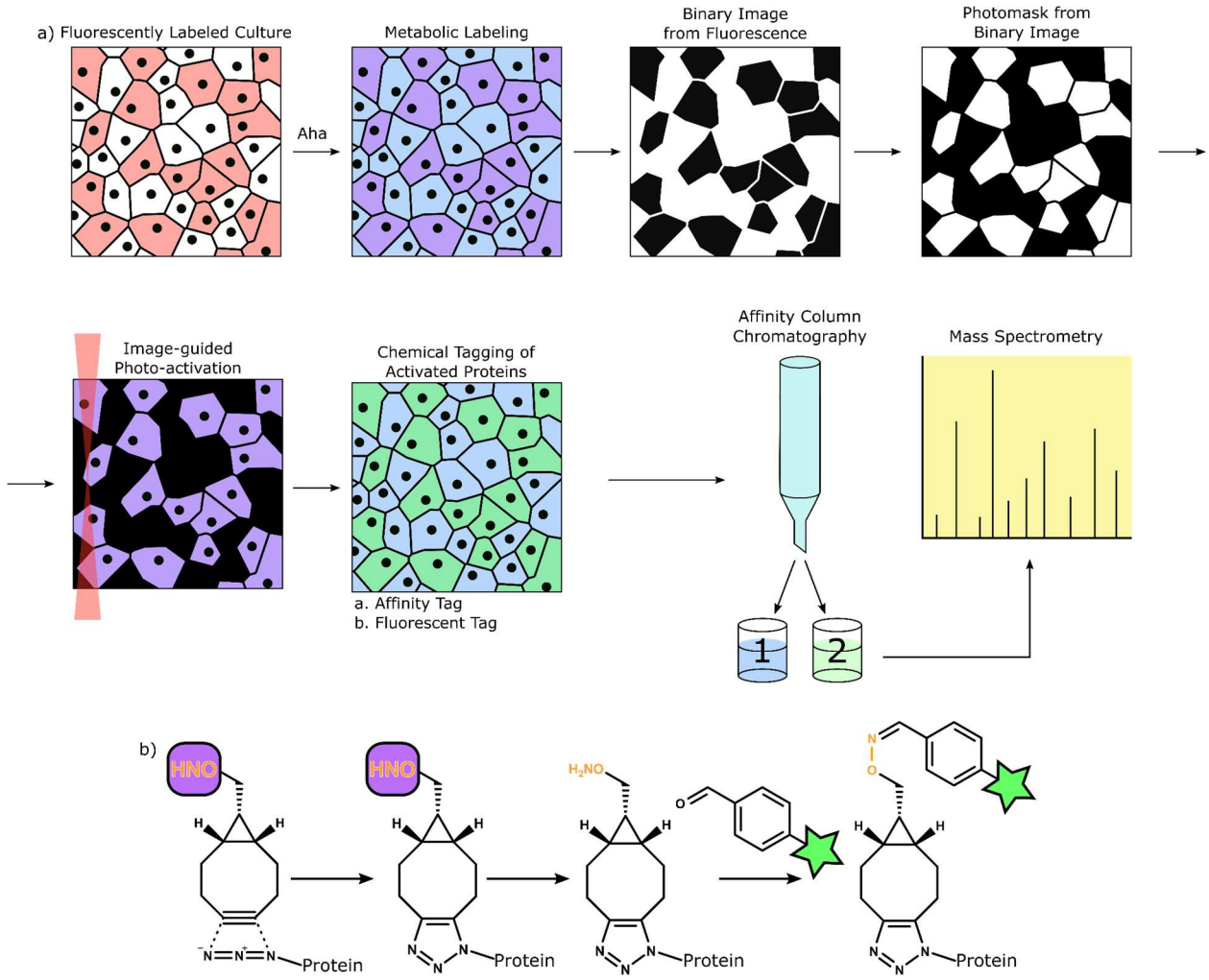

Figure 7. Schematic overview of PhotoActivated IN vitro/vivo tagging (PAINT). (a) Cells are cultured with Aha and treated with the small molecule probe, NPPOC-NHO-BCN. Areas of interest are identified through imaging or fluorescent labeling. A photomask is generated from this imaging and the areas of interest are irradiated with light (1P λ=365 nm; 2P λ=770 nm). Next, activated proteins can be coupled to a fluorescent label for imaging or coupled to an affinity probe for isolation. After affinity column chromatography, the resin is subjected to multiple washes to remove non-activated proteins. Then immobilized proteins are eluted by denaturing streptavidin before being subject to tandem mass spectrometry. (b) Metabolically labeled proteins are coupled to a heterobifunctional probe through a SPAAC reaction. A photocaged hydroxylamine is liberated upon light exposure. The free hydroxylamine will

condense with a benzaldehyde group in the presence of catalytic aniline. This benzaldehyde can be functionalized with a dye for visualization or an affinity tag for isolation, indicated by a green star.

3.1 Synthesis of the small molecule click, photo-probe (NPPOC-NHO-BCN)

For this method the small molecule probe, NPPOC-NHO-BCN, was synthesized by coupling an N-hydroxysuccinimide-activated (2-nitrophenyl)propoxycarbonyl (NPPOC-NHS) to a diamine-polyethylene glycol (PEG), then coupling the remaining free amine to an NHS-activated BCN. Additionally, an agarose amine resin was functionalized with a benzaldehye *via* an NHS-activated 4-formylbenzoic acid (4FBA), and a benzaldehyde functionalized carboxyfluorescein (FAM-BA) was graciously provided by Cole DeForest (Figure 8). Detailed synthetic procedures for all molecules generated in this work are available in the appendix.

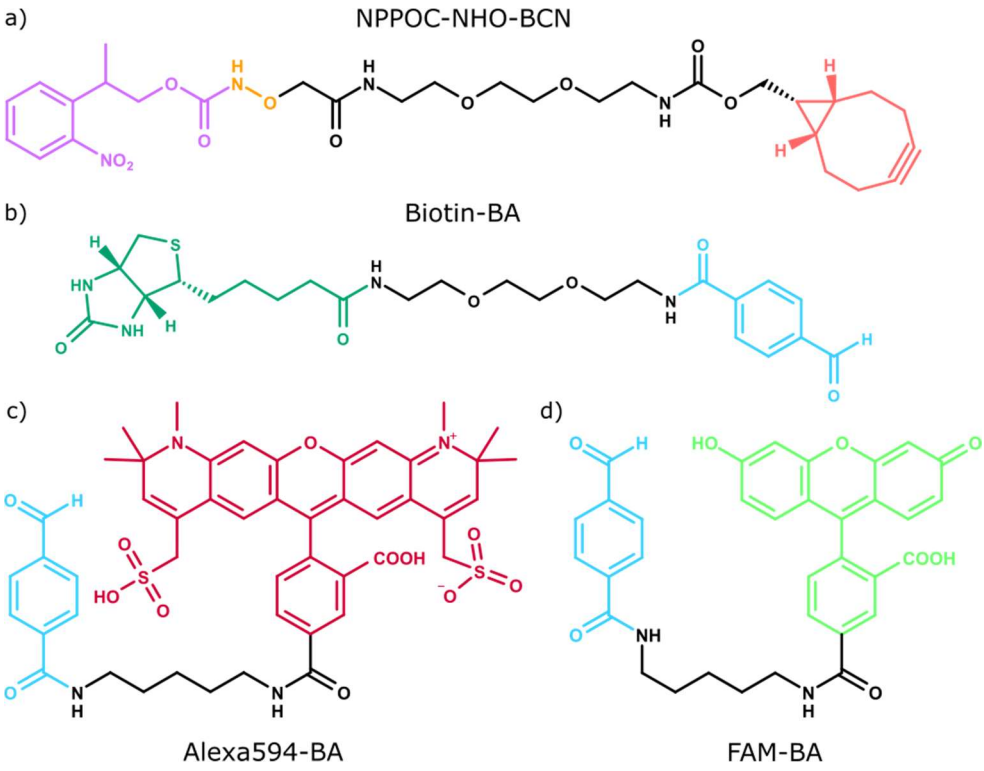

Figure 8. Small molecule tools for subcellular labeling. (a) A heterobifunctional probe with a bicyclononyne on one end and a photocaged hydroxylamine on the other (NPPOC-NHO-BCN) is capable of coupling to azide-functionalized proteins and exposes a hydroxylamine upon light irradiation. (b) Biotin functionalized with benzaldehyde (Biotin-BA) couples to liberated hydroxylamines for affinity column chromatography using immobilized streptavidin. (c,d) benzaldehyde functionalized fluorophores, FAM-BA (c) and Alexa594-BA (d) fluorescently label liberated hydroxylamines for visualization.

3.2 Method demonstration on an azide-functionalized slide

The first demonstration of this system was conducted by the addition and spatially resolved activation of NPPOC-NHO-BCN on a 2D surface. To test the basic chemistry and function of the system, NPPOC-NHO-BCN, was exposed to an azide-functionalized glass slide, serving as a

surrogate for azide-labeled proteins. The slide was irradiated with light (λ = 365 nm, 10 mW cm^{-2}, 5 min), using a photomask with 400 μm wide lines and spaces to allow light exposure only in select regions. As a result, the hydroxylamine is liberated only in the irradiated areas. FAM-BA (100 μM) and aniline (100 mM) were added as a droplet to the slide (1xPBS, 1 hr, RT). The slide was rinsed with DIH_2O before imaging on a fluorescent microscope. Clear patterning of 400 μm lines is visible, demonstrating that both the chemistry and spatial targeting of the system function as designed (Figure A6).

3.3 Method demonstration through *in vitro* activation and photopatterning

The method then demonstrated specific labeling in a biologically relevant environment. HeLa cells are grown on glass-bottom tissue culture plates (Cellvis; D60-30-1.5-N) to a confluency of 90%. Next, cells are labeled with an azide through the pulsed addition of Aha (1 mM, 2 hr), coupled to NPPOC-NHO-BCN (100 μM, 1 hr, 1xPBS) *via* SPAAC, and irradiated with light (λ = 365 nm, 10 mW cm^{-2}, 5 min). The negative controls received a subset of the treatments or none. After lysis, activated proteins were coupled to FAM-BA (100 nM; 5 hr; RT, 1xPBS) and were then subjected to separation by SDS-PAGE. Only the lane corresponding to all four treatment conditions (FAM-BA, NPPOC-NHO-BCN, hν, and Aha), showed enhanced fluorescence. Coomassie staining indicates that the difference in fluorescence is not correlated with protein concentration (Figure 9).

As a further increase in the level of complexity, the labeling of subfractions of cells in tissue culture was conducted. HeLa cells were cultured and treated as described above. Subfractions of tissue culture labeled protein is then activated with light (λ = 365 nm, 10 mW

cm^{-2}, 5 min), using rubber photomasks that block a fraction of the light impinging the sample (0-100%). After cell lysis and collection, the labeled proteins are coupled to FAM-BA for visualization and subjected to SDS-PAGE. The resulting fluorescent gels were quantified with FIJI and normalized. The data fits well to the 45-degree line, as expected (Figure 9).

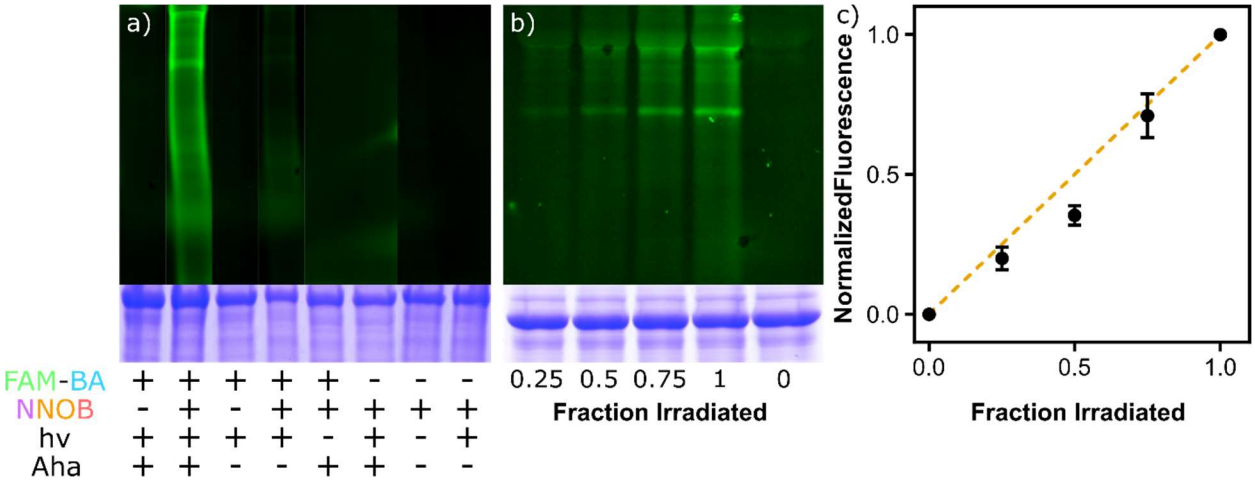

Figure 9. Selective protein labeling *in vitro*. (a) All four treatments (FAM-BA, NPPOC-NHO-BCN, light, and Aha) are necessary for the visualization of labeled proteins. The absence of any treatment results in loss of signal. (b) Irradiation of subfractions of tissue culture leads to a corresponding amount of protein labeling. (c) When quantified, the amount of labeling agrees well with the expected signal (orange dotted line).

To visualize the spatial labeling afforded by the system *in vitro*, cells were cultured and labeled as described, but activated with light through a chrome photomask with 400 µm lines or a 300 µm x 300 µm University of Washington 'W' logo, containing features as small as 50 µm (Figure 10). The broad application of this technique was highlighted by its successful application to both living and fixed cells (MeOH, 10 min, –20 °C). To demonstrate subcellular labeling a

two-photon microscope (Olympus FV1000 MPE BX61) using infrared light (λ = 730 nm or 800 nm) to activate the labeled proteins in fixed cells. The subcellular patterning is remarkably sharp (Figure 10) with resolution on the order of 1 μm (Figure 10f) from the initial testing. Cells are clearly bisected, demonstrating the capability to spatially activate subcellular proteins. This indicates that isolation of proteins from subcellular features is feasible. Optimization, through improving light exposure conditions and magnification, could improve the resolution to near the wavelength diffraction limit (~0.3 μm).

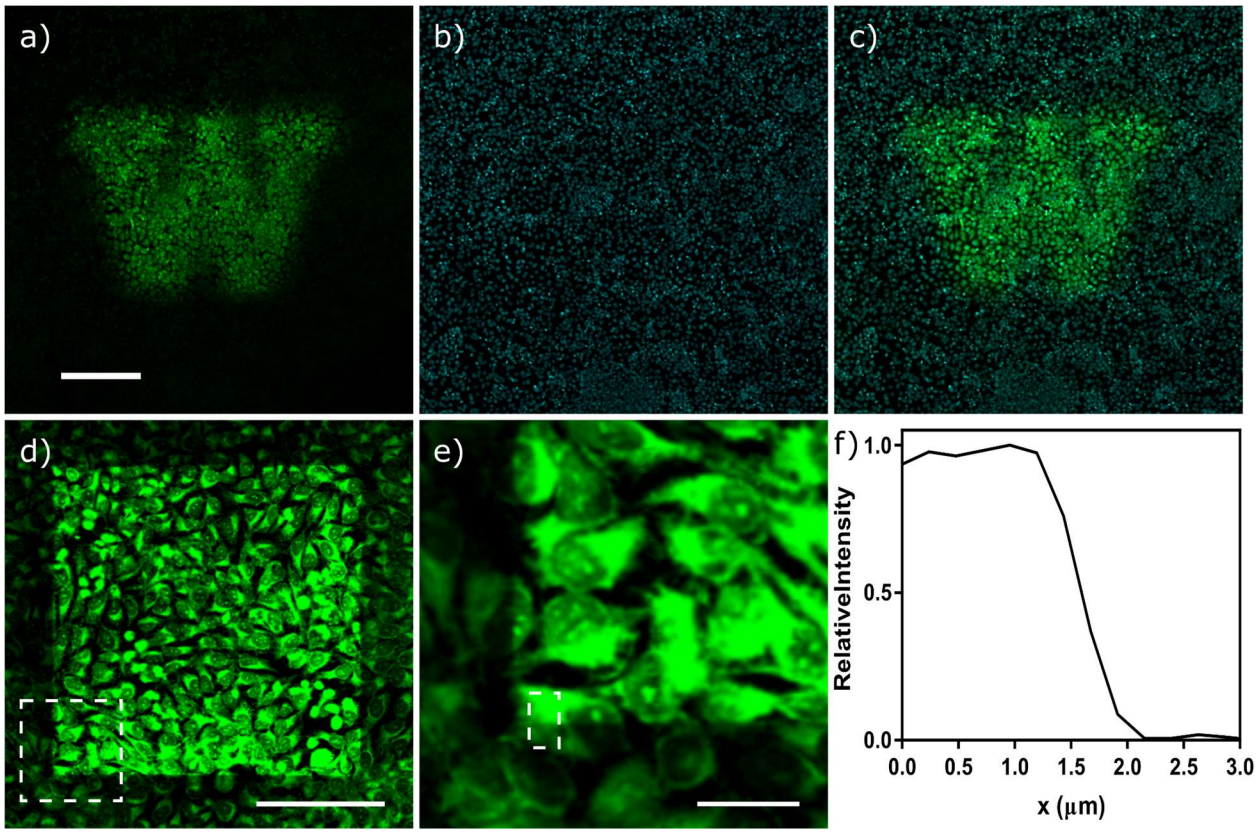

Figure 10. *In vitro* patterning of labeled proteins. (a) Labeled proteins activated through a photomask and labeled with FAM-BA. (b) DAPI staining of the same cells. (c) Combined image of (a) and (b). (d) two-photon (λ = 770 nm) activation of proteins in a square pattern. (e) inset of (d). (f) quantification of the interface in

(e) demonstrates spatial patterning on the order of 1 μm. Cells are clearly bisected in (e), demonstrating the feasibility of subcellular protein isolation. (Scale bar (a)=(b)=(c)=100 μm; (d)=50 μm; (e)=10μm)

The same method can be applied sequentially to activate multiple areas from the same tissue culture (Figure 11). This application would be useful for investigating systems with multiple features of interest. Alternatively, it could be used to measure the heterogeneous response to stimuli by comparing proteomic differences in discrete regions of culture.

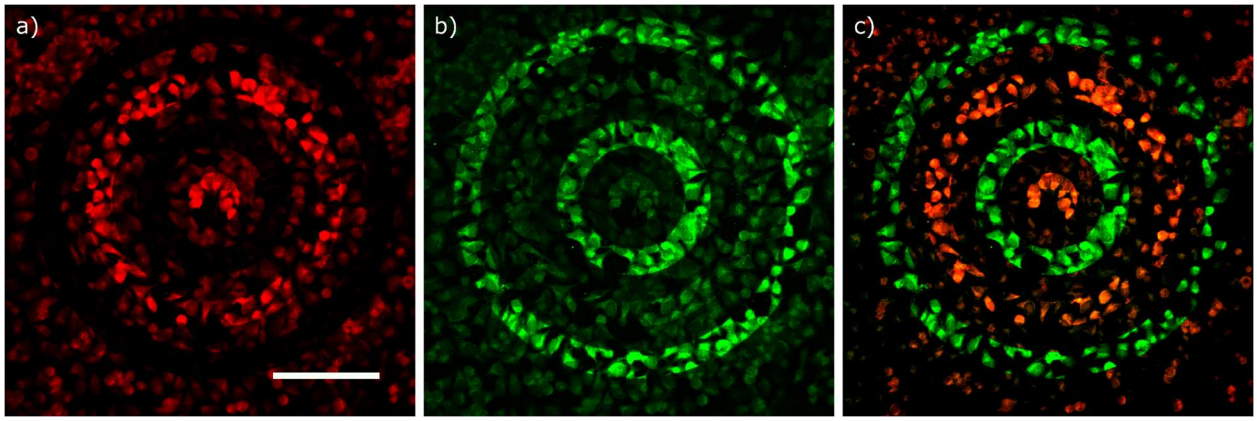

Figure 11. Sequential patterning of labeled cells *in vitro*. Cells are metabolically labeled with Aha and chemically labeled with NPPOC-NHO-BCN as described then activated using a two-photon microscope. Any arbitrary shape can be used. Here a series of rings are patterned. a) First a circle and ring are defined as the areas for irradiation. The activated proteins are then labeled with Alexa594-BA, resulting in the activated areas appearing red. (b) a second round of irradiation can be conducted to activate a different region of the culture. Two additional rings are defined as the areas for irradiation. The activated proteins are then labeled with FAM-BA, resulting in the newly activated areas appearing green. (c) composite of (a) and (b). (Scale bar (a)=(b)=(c)= 50 μm).

3.4 Image-guided photoactivation *in vitro*

We were inspired by some other work in our group using binary and grayscale images to impart patterns and gradients on protein-coupled hydrogels through the use of a MATLAB® script that converts an image into a region of interest (ROI) on the two-photon microscope. It was hypothesized that this same technique, with minor modifications, could be used to generate binary photomasks based on an image generated from biology itself. This would automate the selection and activation of tissue culture subfractions. Antibodies can be used to localize processes of interest and an image generated using fluorescent secondary antibodies from which a corresponding photomask is generated.

Here, a coculture of HS5a cells endogenously expressing either GFP or mCherry were plated onto glass-bottom well plates. The cells can be imaged directly, but without a tissue culture chamber, the cells are not amenable to an extended duration outside of a temperature and pH-controlled environment required by the procedure. Instead antibodies against GFP and mCherry were employed to visualize the subfractions of cells in the coculture after fixation with methanol (Figure 12). From these images two photomasks were generated, one for GFP expressing cells and one for mCherry expressing cells. These photomasks were then compared against each other to determine the degree of undesired capture. By controlling confluency and reducing photomask area through the removal of two pixels from the perimeter of each ROI both photomasks resulted in less than 5% capture of the opposite channel (Figure 12g,f).

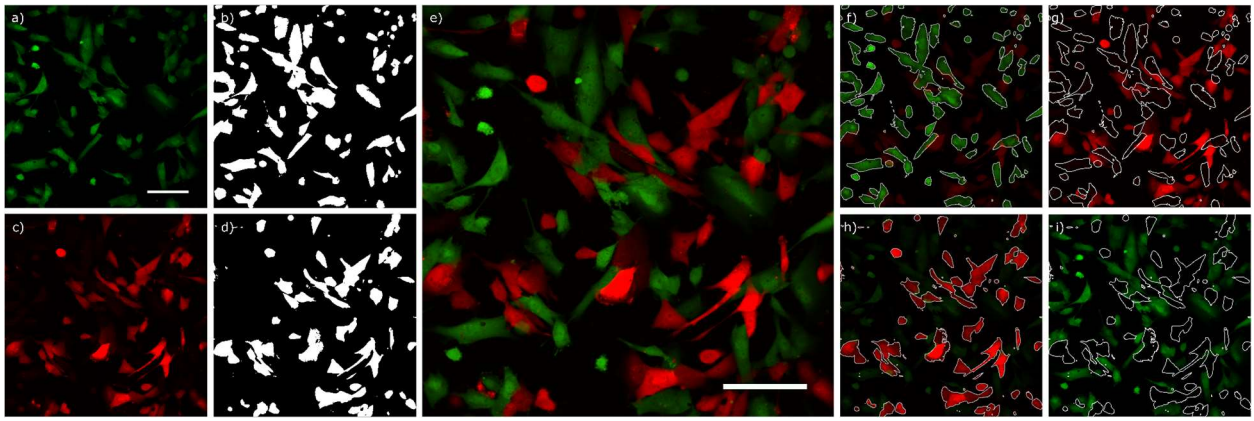

Figure 12. Fluorescence-based photomask generation. A coculture of HS5a cells endogenously expressing (a) GFP or (c) mCherry is imaged. Photomasks based on either the (b) green or (d) red channel is generated. (e) Overlay of (a) and (b). Each mask is applied to both channels to determine how well it captures the desired signal (f, h) and the opposing signal (g, i). (Scale bar (a-d), (f-i) = 50 µm; (e) = 50 µm).

Employing this technique in a mixed coculture is incredibly effective as a tool for activating metabolically labeled proteins features from a heterogeneous sample (Figure 13). A coculture of HS5a cells expressing GFP and mCherry are metabolically labeled with Aha over a 2-hour period as described. The culture is then coupled to the small molecule probe (NPPOC-NHO-BCN) before fixing in methanol. Antibody labeling against mCherry gives an image that is used to generate a photomask (Figure 13b,f). This is then employed to activate labeled proteins only in the areas where cells are expressing mCherry. Finally, these activated areas are visualized by coupling to FAM-BA. The activated areas correlate well with the features of interest (Figure 13d,h).

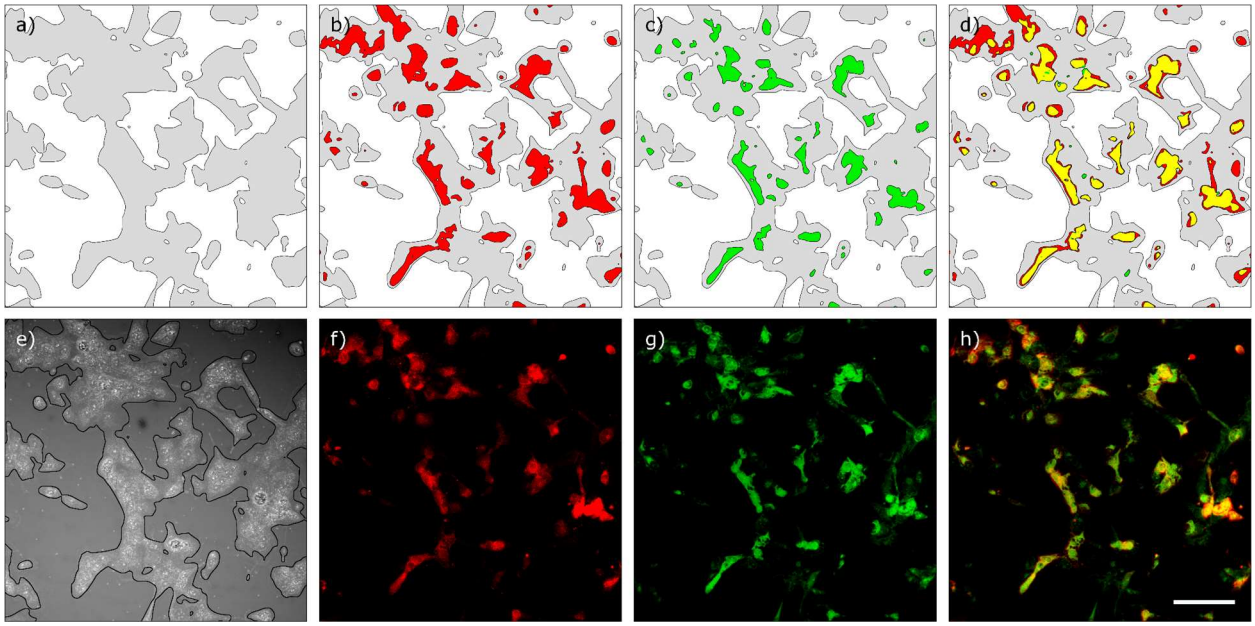

Figure 13. Image-guided photoactivation of mixed cell culture. The total cell area (a) of an HS5a coculture brightfield image (e; perimeter indicated for emphasis). Cells endogenously express either GFP or mCherry. (b) A photomask, indicated by red areas, is generated using immunohistochemistry against mCherry (f). This photomask is imparted by two-photon lithography to activate metabolically labeled proteins in those areas. The activation is visualized by coupling through an oxime condensation between activated proteins and FAM-BA (c,g). (d) A comparison of (b) and (c) illustrates the intersection (yellow) of the areas of interest and the labeled areas. (h) Overlay of (f) and (g). (Scale bar (a-h) = 50 µm)

3.5 Protein isolation by affinity column chromatography

The next step is to isolate activated proteins from these areas by affinity column chromatography for subsequent tandem mass spectrometry (MS/MS). The labeled proteins are functionalized with a biotin-aldehyde (100 mM aniline, RT, pH 7.2, 5 hrs, 1xPBS); excess biotin is removed by desalting column. The biotin-functionalized proteins are then immobilized on a streptavidin

column while the unlabeled proteins flow through the column during multiple washes. The bound proteins are selectively cleaved by the denaturation of streptavidin (6 M urea, 3 M thiourea, 30 mM biotin, 1% SDS, RT, 15 min; 90 °C, 15 min)[51]. By irradiating subfractions of the sample with light (0 – 100%), a known fraction of the labeled proteins is activated. Isolating the proteins as described and subjecting them to SDS-PAGE followed by silver staining yields scaled amounts of protein recovery, demonstrating that the system functions as intended (Figure 14).

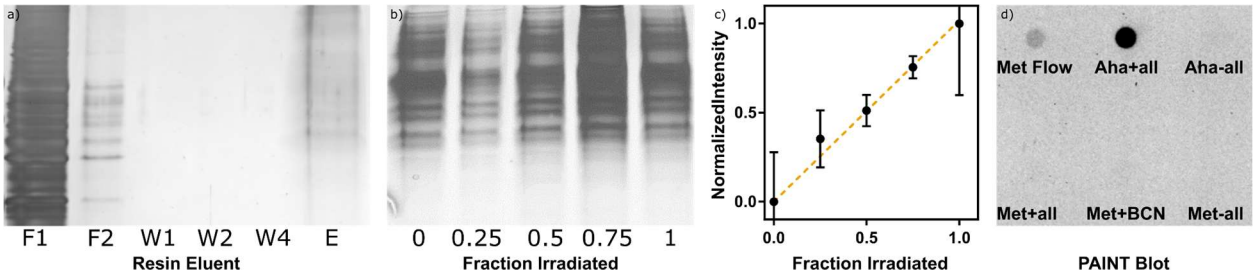

Figure 14. SDS-PAGE of selective protein labeling and isolation *in vitro*. (a) After protein immobilization on streptavidin non-labeled protein flows through the column (F1 and F2). Several washes (W1: urea, W2: NaCl, W4: HEPES) ensure no unselective binding occurs. Wash 3 (CH_3CN, TFA, H_2O) does not run on SDS-PAGE. Gels are stained with silver for visualization (b) Irradiation of subfractions of tissue culture leads to a corresponding amount of protein labeling and isolation. (c) When quantified, the amount of labeling agrees well with the expected signal (orange dotted line), but the variance is much higher than expected.

Although the system works as described, the background level was much higher than expected. It is essential to remove as much background noise as possible for this technique to successfully identify a small subset of proteins from a large, complex mixture. To address this

issue, two alternatives were identified. The first was to use more rigorous washing steps to remove non-selective adsorption of proteins to the resin. The second was to functionalize an amine resin with 4FBA-NHS and couple the proteins directly to the resin. This approach reduces post-lysis processing by removing a coupling reaction. Unfortunately, synthesizing and purchasing an aldehyde-functionalized resin did not significantly improve the results. The best results were achieved by prewashing the resin in coupling buffer (1xPBS, 2 M NaCl, 0.5% SDS) and proceeding as described above. With these improvements, it is estimated that the total background signal was reduced by roughly 80%. It is expected that proteins isolated using this technique can be identified by tandem mass spectrometry, culminating in a new tool for the investigation of molecular biology.

3.6 Zebrafish: an ideal model organism

After thoroughly demonstrating the PAINT method *in vitro*, we sought to challenge the system further using an *in vivo* model. Zebrafish represent an ideal candidate as the system has been used to study embryonic development[104–106] and many diseases[107]. In addition, several transgenic lines have been developed that lack nearly all pigmentation[108,109], offering an ideal platform for a method where photoactivation is essential. Wild-type zebrafish remain almost entirely transparent for several days after fertilization, while transgenic lines, lacking pigmentation, remain transparent for several weeks and are still semi-transparent as adults. Another transgenic line has been developed where Flk-1 (VEGF2, Kdrl), an angiogentic protein localized to the cardiovascular system, has been fused to GRCFP, a reef coral green fluorescent protein, to fluorescently label the entire organ system[110,111]. There are several fusion protein pairs that have been developed to image a variety of organ systems[112,113].

We envisioned using the intrinsic fluorescence of the Flk1-GFP zebrafish as a guide for photoactivation. Here, an image would be generated using the fluorescent protein, which would then be converted into a photomask using a program developed in our group (Appendix B). This mask is then used to selectively irradiate the sample to active proteins in spatiotemporally defined regions through small molecule probe photo-uncaging and subsequent fluorescent/affinity tagging.

3.7 Transgenic zebrafish breeding overview

The transgenic zebrafish lines Flk1-GFP and Casper (nacre$^{-/-}$, Roy$^{-/-}$) were available in the ISCRM aquatics center. The Crystal line (nacre$^{-/-}$, Roy$^{-/-}$, alb$^{-/-}$) was a generous gift from Christian Laurence at Boston Children's Hospital. We sought to generate a transparent, fluorescently labeled fish line for the application of image-guided PAINT (Figure 15). First Casper was crossed with Flk1-GFP to give the first generation (F1a). This generation is heterozygous for the pigmentation and fluorescence alleles (Table 1). Next, this generation was crossed with itself and sorted for the desired phenotype: green fluorescence in the cardiovascular system and a lack of pigmentation with dark black eyes (Slimer). This outcome was the result of at least two genetic recombination events, so only about 5% of larvae displayed the desired traits.

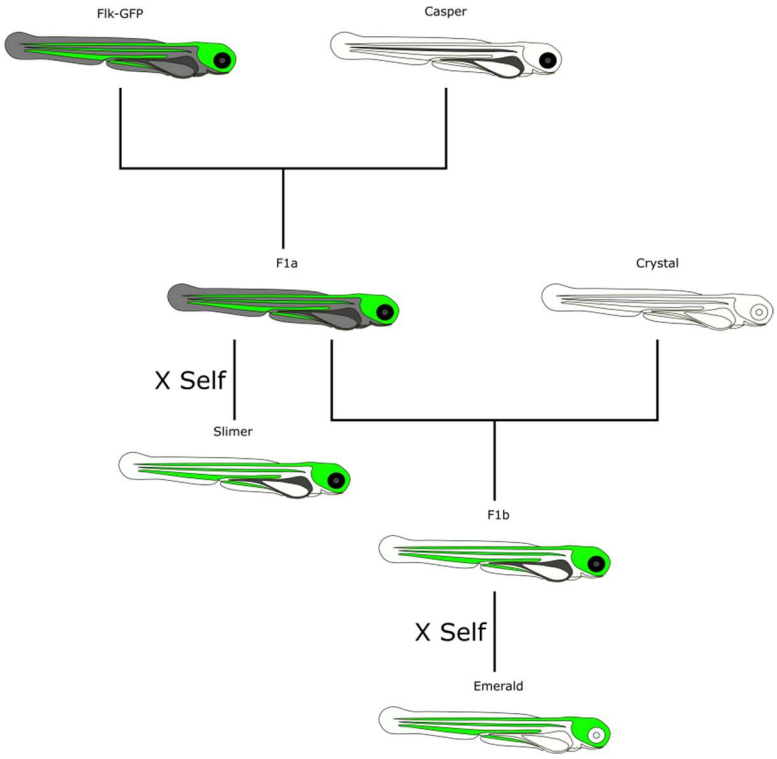

Figure 15. Transgenic fish breeding overview. The Flk1-GFP line was bred against the Casper line to produce a fluorescently labeled line lacking pigmentation (Slimer). The F1 generation from this breeding was bred against the Crystal line to produce a novel, fluorescently labeled line that is even more transparent (Emerald).

Table 1. Genetic makeup of transgenic zebrafish lines.

	Gene			
Zebrafish Line	Flk1-GFP	Nacre	Roy	Alb
Flk1-GFP	+/+	+/+	+/+	+/+
Casper	−/−	−/−	−/−	+/+
F1a	+/−	+/−	+/−	+/+
Slimer	+/?	−/−	−/−	+/+
Crysal	−/−	−/−	−/−	−/−
F1b	+/−	−/−	−/−	+/−
Emerald	+/?	−/−	−/−	−/−

Note: + denotes that the associated gene is present

- denotes that the associated gene is not present

? denotes ambiguous genetics due to the presence of a dominant allele

The crystal embryos were obtained after F1a became mature. As Crystal and Casper share many of the same genes, we chose to breed the crystal line against F1a to increase the odds of obtaining the desired features. This first generation (F1b) was sorted for Casper features, which include a lack of pigmentation and dark black eyes, and a fluorescently labeled cardiovascular system. Larvae with these traits represented roughly 50% of the brood. Next, this generation was crossed with itself and sorted for the desired phenotype, green fluorescence in the cardiovascular system and a complete lack of pigmentation including the eyes.

3.8 PAINT demonstration in zebrafish

After zebrafish breeding embryos were collected and placed into larvae medium (0.1 mg methylene blue, 1.2 g Instant Ocean®, 1 L DIH_2O). After 7 days post fertilization (dpf), larvae

were immersed in larvae medium containing Aha (4 mM, 4 mL, 3 larvae) to metabolically label proteins with the azide functional group. The Aha-containing medium was replaced daily for 3 days. The larvae were placed in 35 mm-diameter untreated polystyrene plates prior to anesthetization (1xPBS, 0 °C, 5 min) and fixation (MeOH, 0 °C, 5 min x3; MeOH -20 °C, overnight). After rehydration (75, 50, 25, 0%, 3 mL, MeOH in PBST, 5 min, RT), specimens were reduced (DTT, 10 mM, PBST, 3 mL, 5 hrs) to decrease background labeling. Azide-functionalized proteins were then labeled with the small-molecule probe (NPPOC-NHO-BCN, 100 μM, PBST, 3 mL, 2 hrs). The chemically labeled zebrafish were then transferred to glass-bottom plates and activated by collimated light (λ=365 nm) using a photomask that exposes only the tail of the zebrafish to light prior to coupling with the small molecule benzaldehyde (FAM-BA, 10 μM, aniline, 100 mM, PBST, 100 μL, 2 hrs) for imaging. We observed a remarkable fluorescent image (Figure 16), where the irradiated tail section fluoresced brightly with excellent signal to noise (the eye exhibits known autofluorescence).

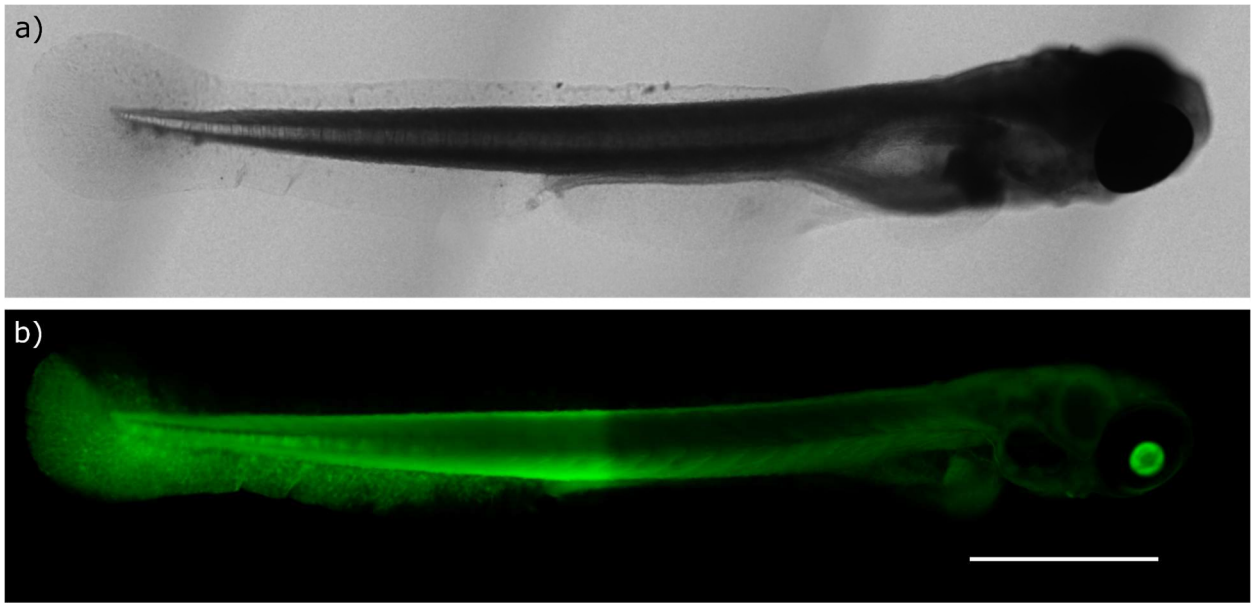

Figure 16. Zebrafish labeling by PAINT using collimated light. (a) Brightfield image of labeled 7 dpf zebrafish. (b) Fluorescent image of labeled zebrafish. After metabolic labeling, the tail section was irradiated (λ=365 nm) and coupled to a fluorescent benzaldehyde (FAM-BA) for visualization. (Scale bar (a)=(b)= 250 μm). The eye exhibits known autofluorescence.

Alternatively, zebrafish embryos (24 hpf) were injected with Aha (10 nL, 70 mM, DIH_2O, pH 7.5) and immersed in Aha embryo media until after emergence (72 hpf). The larvae were then fixed, reduced, and labeled with NPPOC-NHO-BCN as described above. Next, larvae were immobilized in agar (1.4%) for irradiation. A photomask-based on the PAINT logo (Figure 17c) was used to create regions of interest (ROIs) for two-photon activation for proteins within the fish body (λ = 770 nm). After irradiation, the larvae were removed from agar for coupling to FAM-BA (10 μM, aniline, 100 mM, PBST, 2 hrs), and then returned to agar for imaging (Figure 17). Pattern fidelity was observed to be exceptionally high, where the PAINT logo was effectively photopatterned onto newly synthesized proteins throughout 3D space within the fish

body. The culmination of this work is a clear demonstration of the capability to metabolically label proteins in an organism, activate a subset of those proteins in a user-defined region of interest, and visualize that activation with micron-level spatial resolution.

Figure 17. Zebrafish labeling by PAINT using two-photon activation. (a) Brightfield image of labeled zebrafish. (b) Fluorescent image of labeled zebrafish. After metabolic labeling with Aha and the probe (NPPOC-NHO-BCN), a photomask was generated using the PAINT logo (c), and imported into the

microscope as regions of interest for photoactivation. Subsequent two-photon irradiation (λ = 770 nm) was followed by coupling to benzaldehyde (FAM-BA) for visualization. (d) Inset of (b). (Scale bar (a)=(b)= 100 μm; (d)=25 μm). The eye and yolk exhibit known autofluorescence.

Some background staining was observed during these experiments for the methionine negative control (Met, +NPPOC-NHO-BCN, +hν, +FAM-BA), and it was hypothesized that this undesired labeling was due to the well-known but poorly characterized thiol-yne reaction[114]. As this undesired labeling places some limitations on the sensitivity of the PAINT approach, we tested a variety of reducing, alkylating, and blocking conditions to minimize background staining (Figure A10). Reduction converts highly oxidized sulfurs (sulfenic acids, disulfides) to less reactive thiols; alkylation converts thiols into thioethers; and blocking with bovine serum albumin and/or goat serum prevents non-specific binding. Eventually, it was found that treating with blocking solution or alkylating agents did not significantly improve the signal to noise (Figure A10). The best results were obtained by reducing with DTT prior to treatment with the probe, resulting in a signal-to-noise ratio of roughly 2:1 of Aha:Met along with significantly reduced background staining.

3.9 Image-guided 3D photomask generation in zebrafish

Based on the initial success of this technique, we felt it prudent to develop a protocol that couples fluorescent antibodies that stain for heterogeneous proteins of interest to the photolysis of the small molecule probe. For example, an antibody targeting β-amyloid could be designed to fluoresce orthogonally to the photocage (e.g. ex: 561 nm; em: 594 nm), and custom software

would subsequently identify areas that exceed a user-defined threshold and activate the probe in those areas for protein isolation. We envisioned that such a process could be utilized to automate protein activation, greatly reducing the time required for a labor-intensive process while opening up the potential to sample heterogeneities that are not visible otherwise.

Though the initial vision was to utilize the fluorescent proteins expressed as fusion pairs in transgenic fish, it was observed that methanol fixation extinguishes GFP fluorescence in larval zebrafish. Several alternatives were attempted to preserve this intrinsic fluorescence, including reducing the duration of fixation, reducing the concentration of methanol in PBST, and euthanizing larvae and placing them in PBST without fixatives. Unfortunately, all attempted fixation protocols utilizing methanol resulted in a complete loss of fluorescence. Placing larvae in solutions without fixatives did not adequately preserve the specimens during the days of processing that are required.

To overcome these challenges, we attempted to utilize an anti-GFP antibody (Abcam, ab1218) to visualize Flk1 after fixation. When no antibody staining was observed, we discovered that Flk1 appeared to be expressed as a fusion with GRCFP[111], sourced from reef coral instead of jellyfish. BLAST analysis indicated low sequence homology between these proteins (30%; Figure A11), providing an explanation for the lack of staining. Another antibody which was developed against zsYellow (Clontech, 632475) may be effective at targeting this GFP variant, because they were generated from the same source fluorescent protein as verified by a BLAST comparison (Figure A12). To check this hypothesis, a basic local alignment search tool (BLAST) comparison was conducted between zsYellow and all the other proteins for which this antibody has been validated, looking for potential epitopes the antibody utilizes. These sequences were

compared to GRCFP (Figure 18) and it seems likely that the antibody will function with this protein.

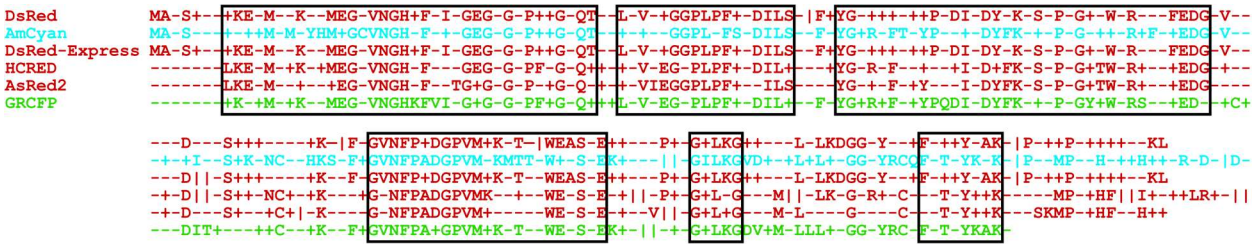

Figure 18. Antibody comparison after BLAST analysis. The sequences of fluorescent proteins (DsRed, AmCyan, DsRed-Express, HCRED, AsRed2) that have been validated against the zsYellow antibody (Clontech, 632475) were compared to zsYellow. Several potential epitopes for this antibody were discovered by identifying conserved sequences. It appears that the reef coral green fluorescent protein (GCRFP) in the Flk1-GFP zebrafish shares many of these sequences, making it a likely target for this antibody.

After initial struggles utilizing genetically encoded fluorescent reporters for image-guided PAINT, we expanded our approach to include the direct antibody labeling of desired proteins. A distinct advantage of this strategy is to rapidly target any protein and/or organ system for which antibodies have been previously developed, sidestepping the need for genetic manipulation. Putting this strategy into practice, we obtained an antibody against Flk1 (Kerafast, ES1003) with the intention of localizing Flk1 and using it to guide photoactivation, with the isolation, and identification of GFP as a positive control. The areas and features should appear similar to those imaged of Flk-GFP. Though additional tissue clearing techniques are likely to prove beneficial in this regard, initial efforts demonstrated poor antibody penetration for fixed

fish at 7 dpf (Figure 19). This lack of penetration was found to be antibody-dependent, as one against α-tubulin (Cell Signaling, 5335S) worked surprisingly well (Figure 20). As a high degree of immunohistochemical staining was observed throughout the fish, we sought to demonstrate image-guided PAINT with anti-α-tubulin. After fluorescent antibody imaging, the z-stack image was converted to a series of z-position correlated photo masks (Figure 20b) using a MATLAB® script (Appendix B) with the intention of using these z-stacked photomasks as a template for 3D photoactivation. Unfortunately, though the import of these photomasks has been automated, the software has consistently failed while attempting to execute this procedure. Recent upgrades to the microscope software may be responsible for these errors during photomask import. Though future efforts will be needed to troubleshoot these errors, the established workflow is expected to support 3D image-guided PAINT in zebrafish and other model systems.

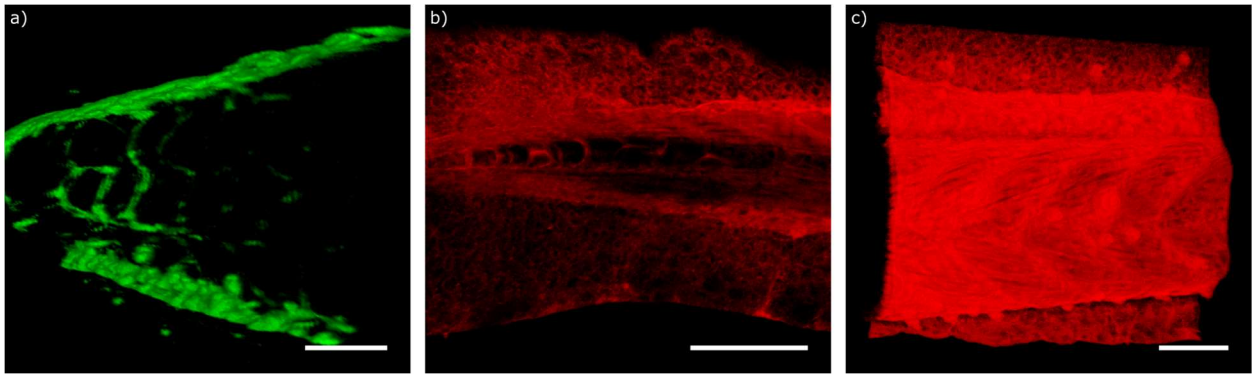

Figure 19. 3D Images of Flk1-GFP and anti-Flk1 immunostaining by two-photon microscopy. (a) Imaging of GFP reveals the zebrafish cardiovascular system. (b) Antibody staining (α-Flk1, α-rabbit-594) of a zebrafish tail section displays some features associated with the cardiovascular system, but a high degree of non-selective labeling. (c) Antibody staining of the zebrafish body cavity did not produce any features associated with the cardiovascular system.

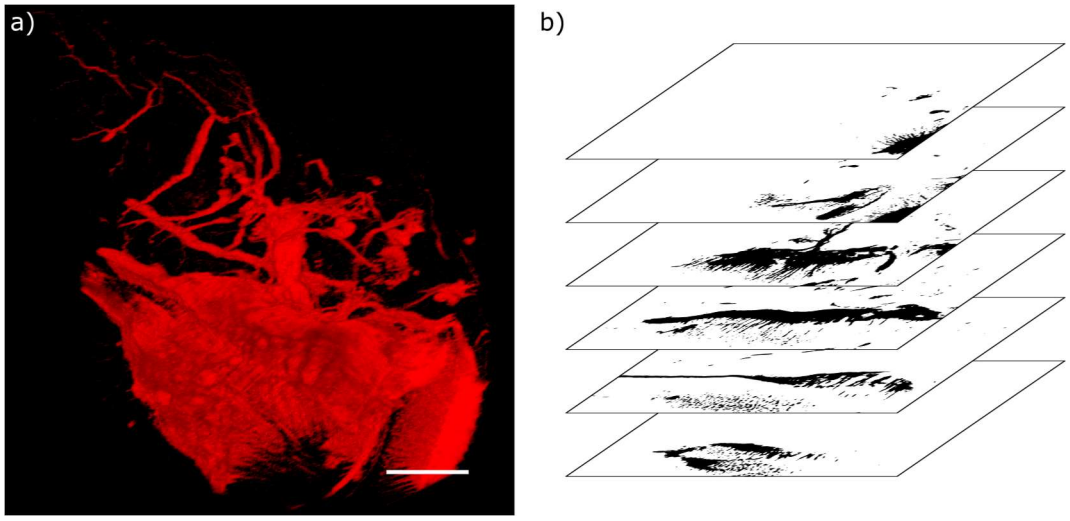

Figure 20. Image-guided photomask generation in zebrafish. (a) A 3D zebrafish image is created using antibodies (anti-α-tubulin, α-rabbit-594). (b) Each z-plane is converted into a photomask using a MATLAB® script. These can be used to photoactivate labeled proteins in these areas.

Here a demonstration of PAINT in zebrafish larvae was demonstrated using user-defined ROIs for activation and labeling and an antibody against α-tubulin to illustrate the feasibility of biologically driven photomask generation. Antibodies against other proteins will have to be validated for their use under the conditions detailed here, so targeting specific proteins with their respective antibody may carry their own limitations. Different models will certainly all have their individual challenges and exhaustive testing here would be prohibitive.

Although this method currently reduces background signal by roughly 80%, based on silver staining of isolated proteins, successful implementation of this method will push that enhancement further, enabling the identification of proteins from ever decreasing subvolumes of culture or specimen. Current state-of-the-art mass spectrometry for proteomics have successfully identified proteins from as little as picograms of complex lysate[115–117]. Further assisted by the

chemical coupling of the probe to Aha, replacing methionine residues, algorithms for processing mass spectrometry data will assist in further screening non-labeled protein using the known difference in mass between methionine and Aha-labeled peptidic fragments.

The PAINT approach provides remarkable flexibility and broad applicability. It demonstrated the ability to activate proteins from user-defined arbitrary regions of interest both *in vitro* and *in vivo*. By using antibody labeling for image-guided photoactivation, the location of any protein of interest can be used to sample spatially defined proteome subset, enhancing the signal for processes of interest. These maps can alternatively be used to create an inverted ROI map to activate areas that are not associated with the selected protein, giving information about a different subset of the proteome. By providing specific information about the proteome in time and space, this technique has major implications for addressing clinical needs in disease diagnostics and treatment and expanding our fundamental understanding of biochemistry.

Chapter 4. Orthogonal photochemistry for dynamic materials

The ability to probe and direct biology's dynamic heterogeneity necessitates the development of bioorthogonal chemistries that can be initiated on-demand with spatiotemporal control in living systems. Though light-based chemistries have excelled in this regard, independent modulation of 2 or more photochemical reactions within a common environment remains largely elusive. Towards this goal, we developed a photoorthogonal reaction scheme consisting of an ortho-nitrobenzyl ester (*o*NB) and a boron-dipyrromethene (BODIPY) that photodegrade in response to λ = 365 nm and 505 nm light, respectively. With negligible absorbance above 425 nm, *o*NB remains undisturbed under 505 nm irradiation while BODIPY undergoes rapid photolysis. Although BODIPY also cleaves with 365 nm irradiation, its comparative slow degradation kinetics permit reaction orthogonality with *o*NB under physiological conditions. Coupling distinct proteins to hydrogel biomaterials through each photolabile moiety, spatiotemporal control over gel biochemical patterning and biomacromolecule release is achieved. When the pair of photosensitive moieties are incorporated into hydrogel crosslinkers, dynamic materials that degrade in response to ultraviolet (UV) and/or visible light are created. Wavelength-selective control over photocleavage reactions will enable expanded applications in 4D cell culture and next-generation drug delivery.

By uncovering new spatial information about biological systems, we hope, eventually, that that information will go towards improving patient outcomes, but it may also prove useful in the field of regenerative medicine. For this goal to be realized it is important to develop increasingly complex biomaterials that can deliver cues at a desired time and location. The stimuli for controlling those cues can vary from pH, reductive environments, enzymes, light, etc.

As demonstrated here, light is especially useful, because it can be activated in precise locations and times, for a specific duration, and without perturbing the biology under study[103].

4.1 Light as a tool for interacting with biology

Light is an excellent stimulus for initiating chemistry as it affords precise control over the reaction by manipulating the duration, location, intensity, and wavelength of irradiation. Photolabile groups have found use in synthesis by providing an independent protecting group with which sensitive groups can be masked while other chemistry takes place. This concept finds purchase in the fields of materials development and biology by providing spatiotemporal control over material properties[118,119] and biomolecule release and/or activation[88,120]. Although the development of a photoorthogonal chemical pair represents a dramatic increase in functionality, only a handful of systems have been reported[73,86] in the decades since they were first discovered[121,122]. Possibly due to their infrequency, the reporting of photo-properties away from a molecule's absorption maximum is sparse, making the construction of a photoorthogonal system even more difficult.

Unfortunately, biology imposes several additional restrictions when these concepts are translated into its domain. Photocaged moieties and their photolysis side-products should be inert such that they ellicit no biological response. Additionally, low-wavelength UV is incompatible with biological systems[123], necessitating the use of molecules sensitive to longer wavelengths. Although the most common biocompatible photolabile groups[77] are sensitive at high-wavelength UV (~365 nm), one would need to be paired with a molecule that has significantly red-shifted sensitivity so that the overlap between the two absorption spectra is minimized.

Since the energy of light is inversely proportional to its wavelength, higher wavelength light carries less energy. Therefore, a molecule that is sensitive to higher wavelengths responds to a proportionally smaller energy than one at lower wavelengths. As a molecule is tuned to a higher wavelength, the energy barrier decreases, and it becomes inherently less stable. This difference in energy is roughly 30% lower at 500 nm compared to 365 nm according to the Plank-Einstein relation. For these reasons, it is difficult to engineer photocages to respond only to high wavelength, making it likely that they will also cleave at lower wavelengths, further complicating the development of a photoorthogonal system. Indeed, the systems reported to date have been designed with this limitation in mind providing a degree of selectivity, although only in a specific order[73].

A system that could deliver omnidirectional orthogonality where two photosensitive molecules are used simultaneously in a material while maintaining selectively by controlling the wavelength of light would be exceptionally useful. This would provide a unique and flexible system capable of delivering unprecedent level of control over 4D tissue culture. The ability to deliver multiple stimuli at a desired time and location has great potential in many different applications. For example, it would be capable of differentiating stem cells in a spatially defined manner[94], selectively changing phenotypes by softening underlying material[124], or sequentially releasing therapeutic molecules that treat disease[125].

4.2 Selecting candidates for a photoorthogonal system

Ideal photolabile groups for this system would have high quantum yield and sufficiently distinct absorption profiles, such that each molecule would remain intact while irradiating wavelengths significantly different than their maximum absorption. Table 2 contains a list of potential

photocages and their properties. Towards the goal of developing a photoorthogonal system, several potential photolabile molecules were identified that might fit these criteria. The first was an ortho-nitrobenzyl ester (*o*NB), a staple in photo-protecting strategies that has been exploited extensively in the development of photoresponsive biomolecules and materials. The molecule has shown remarkable flexibility, finding use in the liberation of bio-active small molecules[126–130], release of bio-active cargo from materials[131–135], and control over material mechanical properties through selective degradation[136] or stiffening[119]. The culmination of these advances have been applied in the development of next generation tissue culture platforms through spatial control over architecture and presentation of biomolecules[94,97,137–140]. *o*NB readily cleaves at 365 nm (Figure 21f) through a quinonoid intermediate and cyclization, arriving at the nitroso photolysis product through rearrangement, while simultaneously liberating the protected group at the benzylic position[141]. Importantly, the molecule possesses little or no absorbance above 425 nm (Figure 21e).

Table 2. Photochemical properties of select photocages.

Compound	λ_{max} (nm)	ϕ (λ=365 nm)	$\varepsilon\,\phi$ ($M^{-1}\,cm^{-1}$)	ϕ (λ=470 nm)*	$\varepsilon\,\phi$ ($M^{-1}\,cm^{-1}$)	ϕ (λ=505 nm)	$\varepsilon\,\phi$ ($M^{-1}\,cm^{-1}$)
*o*NB	327	0.02	10	ND	ND	ND	0
BODIPY	503	4×10^{-4}	3	ND	ND	4×10^{-4}	3.4
DEAC450[142]	454	ND	ND	0.78	33,500	ND	ND
CM-OH[143]	325	0.2	430	0.14	20	ND	ND
tCM-OH[144]	430	6×10^{-3}	12	5×10^{-3}	120	ND	ND

Note: DEAC, 7-diethylaminocoumarin;
CM-OH, 7-amino-(4-hydroxymethyl)-coumarin;
tCM-OH, 7-amino-(4-hydroxymethyl)-thiocoumarin;
λ_{max}, maximum absorption wavelength; ϕ, quantum yield; ε, molar absorptivity.
*values for DEAC450 and CM-OH were obtained at 450 nm and 430 nm, respectively.

4.3 Synthesis of a coumarin photocage precursor

This work began with the synthesis of a coumarin derivative, containing thioester and azide functional groups. The oxidation of the methyl at position four, by SeO_2, provides an essential chemical handle for downstream functionalization. It was hypothesized that installing the thioester at position two and the azide at position seven (Scheme 1) would provide a compound that would be photosensitive at ~450 nm, could be easily functionalized with relevant biomolecules, and coupled into PEG-based hydrogels *via* a SPAAC reaction. Unfortunately, the conversion of the amine to the azide at position 7 blue-shifted the absorption by about 100 nm (Figure A13), making the compound unsuitable to serve along *o*NB in an orthogonal photochemical system.

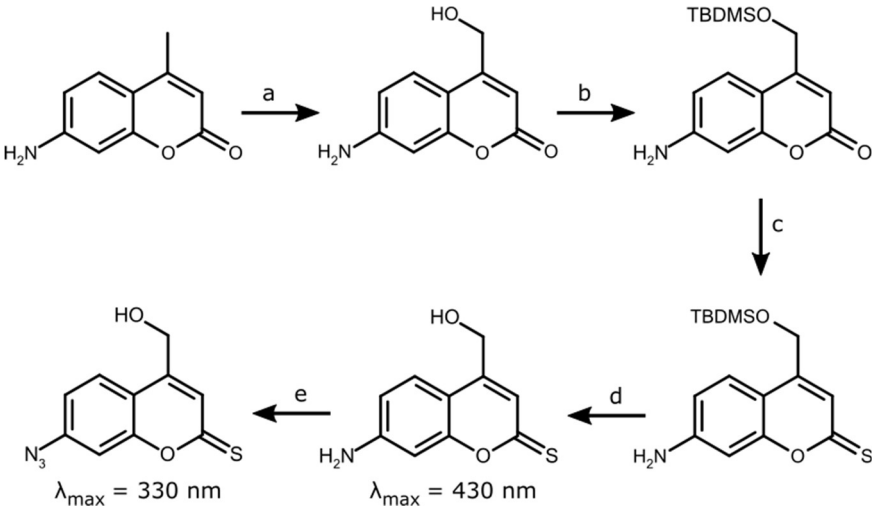

Scheme 1. Synthesis of N_3-tCM-OH. (a) SeO_2. (b) TBDMSCl (c) Lawesson's reagent. (d) TBAF. (e) $NaNO_2$, H_2SO_4, NaN_3.

4.4 Synthesis of a BODIPY photocage

It was recently discovered that a common class of biological dyes known as boron-dipyrromethenes (BODIPY) could be used as a photocage through substitution of an aryloxy at the borate[145]. Upon light irradiation the B-O bond is cleaved resulting in a quinone methide and the corresponding fluoroborane, which are subsequently hydrolyzed by solvent. Although this novel photocaging technique has been used for the selective uncaging of active biomolecules in vitro[146], the work presented here represents the first instance where it is used for the wavelength-selective release of biomolecules from a biomaterial and the wavelength-selective degradation of biomaterial upon light exposure. The use of the BODIPY core is an important innovation because the dyes typically have an absorption that is significantly red-shifted to around 500 nm, potentially making them useful in a two-component photoorthogonal system in combination with an *o*NB photocage.

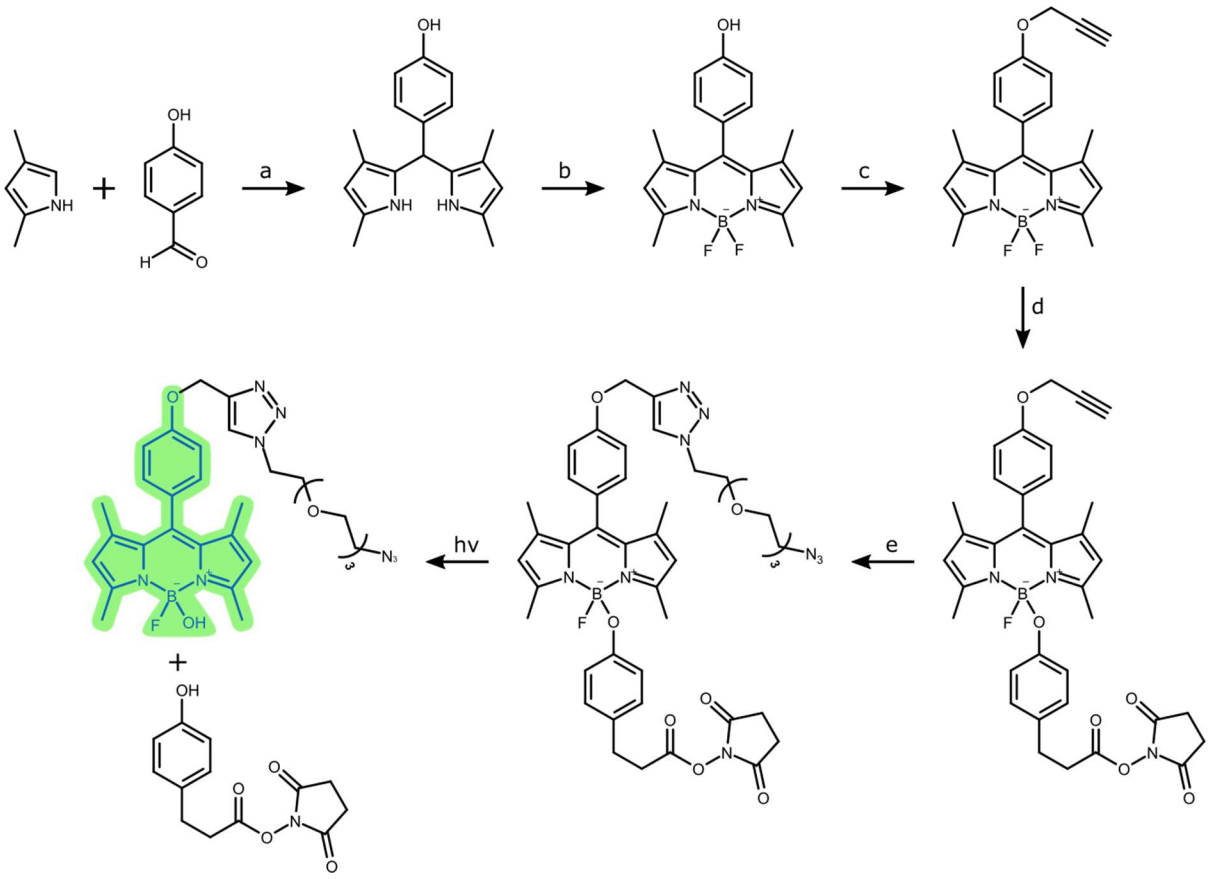

Scheme 2. Synthesis of N_3-BODIPY-NHS. (a) TFA. (b) (i) DDQ, (ii) BF_3-OEt_2. (c) Propargyl bromide. (d) $AlCl_3$. (e) Triethylene glycole diazide. Uncaging by light irradiation (λ = 505 nm) produces a dye that is significantly more fluorescent than the intact BODIPY construct.

The BODIPY core was synthesized as described[145]. An azide functional group was added through a copper-catalyzed azide-alkyne cycloaddition, and an activated ester was added through an aryloxy substitution with $AlCl_3$. In a parallel synthesis that has been described previously[97], an *o*NB molecule was generated that contains an azide and an activated ester but cleaves instead at 365 nm (Figure 21f). The activated ester is a useful reactive center for coupling any molecule of interest while the azide provides a functional handle for incorporation into click-based hydrogels. The measured absorption profiles of each molecule indicate the plausibility of their

use in a photoorthogonal system. A kinetic analysis of these molecules revealed that BODIPY responds to both 365 and 505 nm light. Interestingly, the fluorescence of the BODIPY dye that is quenched by the addition of the aryloxy[147] is restored upon photocleavage (Figure A15g). Fortunately, the response of BODIPY was much slower than *o*NB at 365 nm (Figure A15a, Table A1) and *o*NB did not respond to irradiation at 505 nm (Figure 21g, Figure A16b).

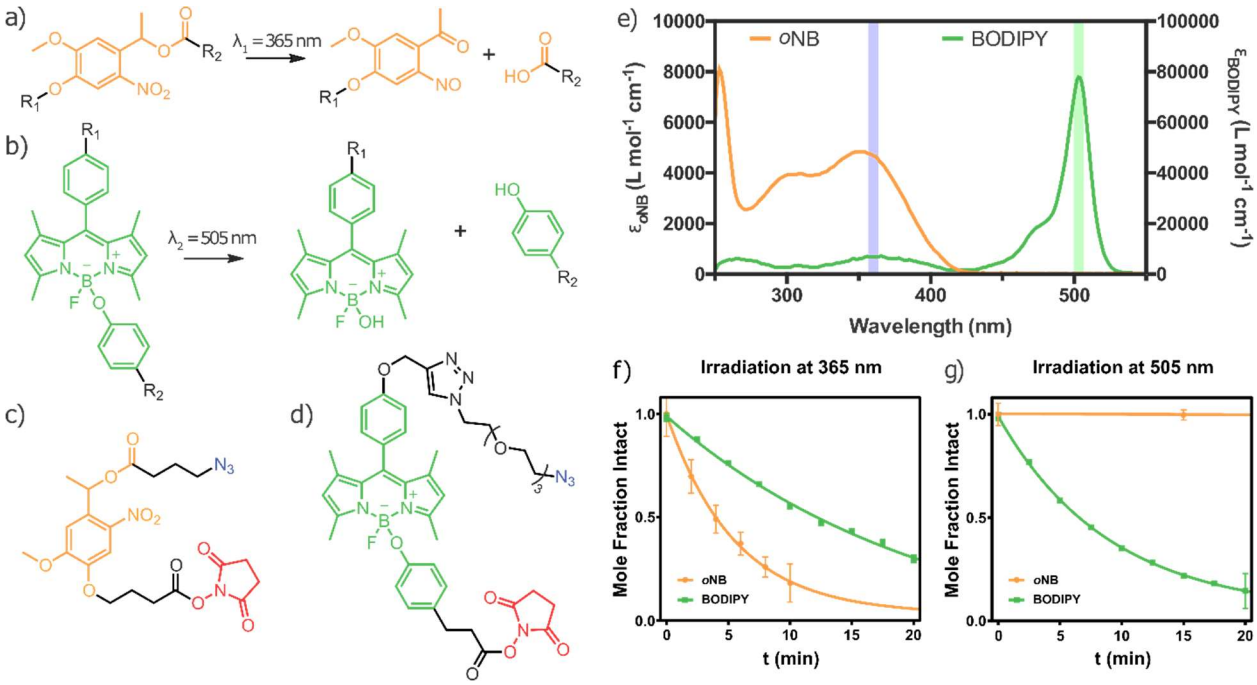

Figure 21. An orthogonal photochemical reaction pair. (a) On exposure to 365 nm light, the ester bond of *o*NB cleaves, resulting in the nitroso and carboxylate. (b) On exposure to 505 nm light the boron-oxygen bond cleaves, resulting in the borate and phenol. (c) Structure of N_3-*o*NB-OSu. (d) Structure of N_3-BODIPY-OSu. (e) Absorbance profiles of *o*NB and BODIPY demonstrate a large gap between their respective maximum absorbance wavelengths, and *o*NB displays low absorption above 425 nm. The Purple bar indicates 365 nm light, while the green bar represents 505 nm. (f) BODIPY and *o*NB are both photosensitive at 365 nm (data for *o*NB reproduced with permission[97]). (g) *o*NB is unaffected by

irradiation at 505 nm light, while BODIPY cleaves readily under irradiation at this wavelength.

4.5 Selective release of proteins from hydrogels

To demonstrate the utility of this system in a biological context, BODIPY was coupled to mCherry and *o*NB was coupled to mCerulean and the extent of protein labeling was estimated using the known molar absorptivity for each photocage and protein (Figure A17). Single component hydrogels were created containing mCherry coupled BODIPY (or mCerulean coupled *o*NB), a diazide poly(ethylene glycol) (PEG) crosslinker (3 kDa), and a 4-arm PEG tetra-bicyclononyne (BCN) (20 kDa). Gels were formed between two Rain-X® coated glass slides with 1 mm rubber spacers (1.5 hr). The gels were then placed into glass scintillation vials and washed (1xPBS, pH 7.2, 48 hrs) to remove any unbound protein. Hydrogels containing only BODIPY-mCherry were subjected to patterned irradiation (505 nm, 20 mW cm^{-2}, 30 min). Imaging revealed protein release only in the irradiated areas and green fluorescence in the irradiated areas, indicating cleaved BODIPY (Figure A19). In other words, the restoration of BODIPY fluorescence upon irradiation could be used to identify where protein had been removed from the material. A mixed hydrogel, containing both BODIPY-mCherry and *o*NB-mCerulean was then subjected to sequential, patterned irradiation (505 nm, 20 mW cm^{-2}, 30 min; 365 nm, 10 mW cm^{-2}, 30 min) using a chrome photomask to impart a pattern and demonstrating the capability to selectively cleave BODIPY-mCherry in the presence of *o*NB-mCerulean (Figure 22). Negligible photobleaching was observed for either mCherry or mCerulean under extended irradiation at λ = 365 nm and 505 nm (Figure A20, Figure A21).

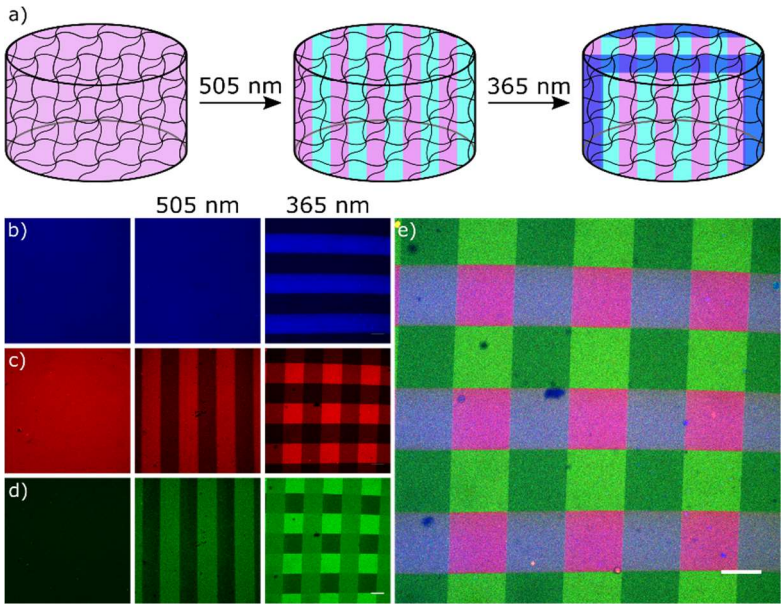

Figure 22. Photopatterning of protein-coupled hydrogels. (a) BODIPY-mCherry and *o*NB-mCerulean coupled hydrogels are exposed to 505 nm light through a photomask to impart a pattern. mCherry diffuses out of the material while *o*NB-mCerulean remains unaffected. Exposure at 365 nm releases both mCherry and mCerulean. (b) Before irradiation all three channels (blue:mCerulean, red:mCherry, green:cleaved BODIPY) appear uniform and BODIPY fluorescence remains low. (c) After irradiation at 505 nm through a photomask *o*NB mCerulean remains intact. mCherry is released in the exposed areas (400 μm parallel lines), while BODIPY becomes more fluorescent in the same region. (d) After irradiation at 365 nm through a photomask both *o*NB mCerulean and mCherry are released in the exposed areas (400 μm lines orthogonal to the first exposure), and BODIPY becomes more fluorescent in all exposed regions. (e) Overlay of all three channels. Scale bar = 200 μm.

Next, the release of fluorescent protein from the material upon irradiation was quantified. Photocage-protein coupled hydrogels were irradiated with light (BODIPY-mCherry:505 nm, 20 mW cm^{-2}, 1 hr; *o*NB-mCerulean: 365 nm, 10 mW cm^{-2}, 4 min) to release protein into solution.

The proteins were allowed to diffuse out of the hydrogels over the next 4 hours and the fluorescence of the solutions was monitored (mCherry ex: 550 nm, em: 610 nm; mCerulean ex: 433 nm, em: 475 nm) with a spectrophotometer (Figure 23). Triggered release of each protein was successfully achieved and was proportional to intensity of light exposure. Little background release was observed in either case.

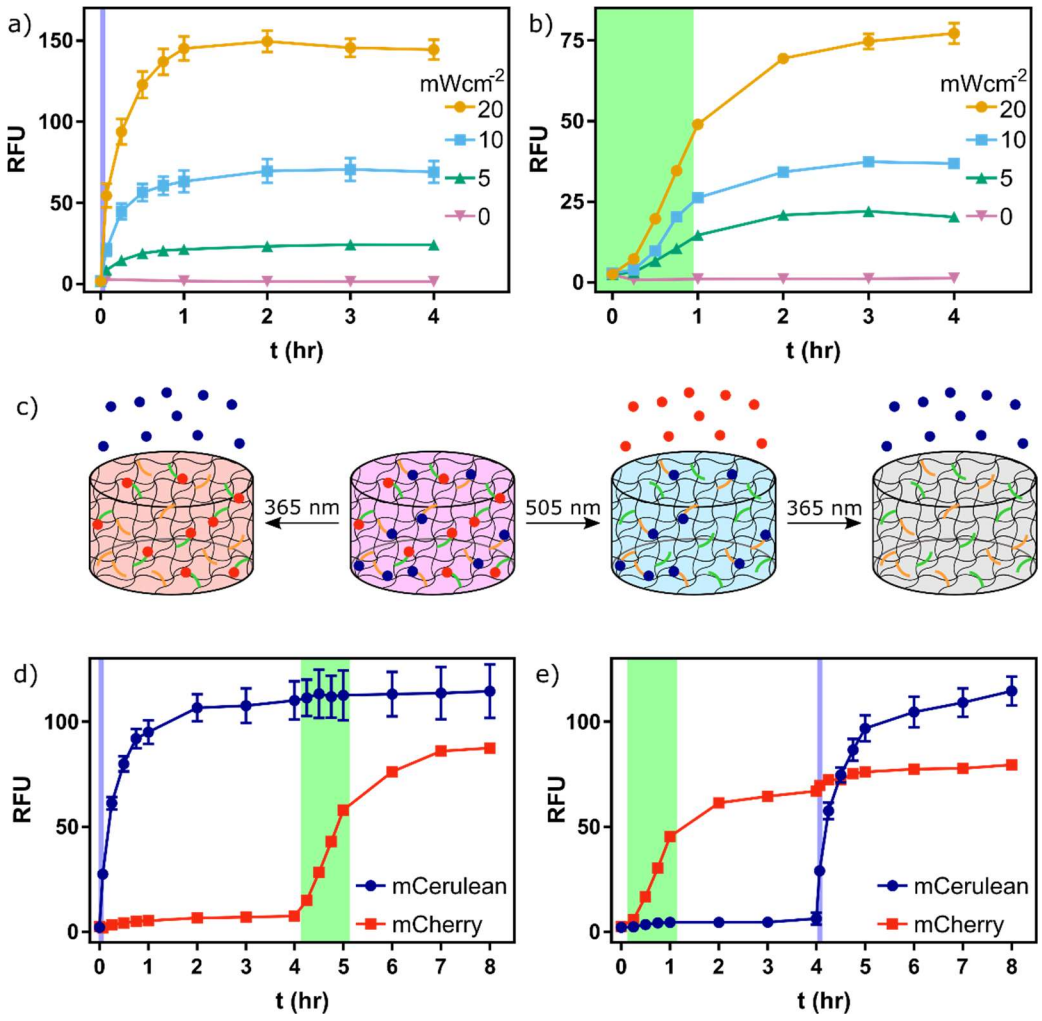

Figure 23. Selective release of fluorescent proteins from PEG-based hydrogels upon light exposure. (a) Release of mCerulean after light exposure (365 nm), indicated by a vertical purple line. The release was monitored over several hours.

(b) Release of mCherry after light exposure (505 nm), indicated by a vertical green band. The photocleavage appears much slower than that of the *o*NB coupled mCerulean. (c) By combining both photocaged proteins into the same gel it is possible to selectively cleave the desired protein by controlling the wavelength of light used for the exposure. 365 nm light releases mCerulean from the material (blue circles) and 505 nm releases mCherry (red squares). (d) and (e) Multiple component gels selectively release the desired fluorescent protein after light irradiation. Subsequent light irradiation selectively releases the other protein from the hydrogel. The system operates as expected irrespective of the light exposure order; (d) 365 nm, followed by 505 nm; (e) 505 nm, followed by 365 nm. Overall protein release appears consistent for both conditions.

4.6 Orthogonal release of proteins from multicomponent hydrogels

During these experiments it was observed that the BODIPY-photocaged mCherry required much longer exposure times than expected for effective protein release from the material. It is hypothesized that this was due to fluorescence resonance energy transfer (FRET) between the BODIPY molecule and the mCherry fluorophore (Figure A18), which has also been observed between GFP and mCherry[148,149]. Although the BODIPY molecule photocleaves under 365 nm irradiation, it was hypothesized that this reduced response to irradiation might allow kinetic control over protein release by limiting the irradiation time at 365 nm.

Next, mixed gels were constructed that contained both fluorescent proteins coupled to photolabile groups in the manner described above. The gels were exposed to one wavelength followed by four hours to allow diffusion of the proteins out of the gel, then they were irradiated with the other wavelength. In both cases selective release of a single fluorescent protein was

observed with low levels of non-selective release (Figure 23). Further, the gels can be exposed to another dose of light to selectively release additional protein (Figure A22).

4.7 Small molecule patterning *via* photorelease from multicomponent materials

As an extension on this work, BODIPY was coupled to the small-molecule-dye Cy7, while *o*NB was coupled to Cy5, with the intention to spatially pattern a hydrogel upon light exposure at different wavelengths. The two photosensitive groups were individually coupled to a four-arm 20 kDa molecular weight PEG-tetraBCN *via* a SPAAC reaction. They were then incorporated into a PEG-hydrogel by the addition of a bifunctional azide crosslinker. The gels were then irradiated with either 365 nm light (*o*NB; 10 mW cm^{-2}, 10 min) or 505 nm light (BODIPY, 20 mW cm^{-2}, 30 min) through a slitted photomask (400 μm parallel lines with 400 μm spacing) to selectively release the fluorophores in the irradiated area (Figure A14a,b). Next, both fluorophore-coupled photocleavable groups were coupled into the same gel and irradiated sequentially with 505 nm through a slitted photomask and 365 nm light through a slitted photomask rotated 90 degrees to provide perpendicular patterning (Figure A14e).

4.8 Crosslinker generation and photo-rheology

Biological systems respond to both chemical and mechanical cues. To demonstrate the generality of this photoorthogonal system, each photolabile group was converted to a crosslinker for use in hydrogels. The selective degradation of these crosslinkers would allow for the independent, controlled change in mechanical and biochemical cues simultaneously or sequentially. Since these molecules contain an NHS-activated ester, they can be conveniently coupled to any desired

molecule or biomolecule that contains an amine functional group. To develop degradable crosslinks, each was coupled to a 3 kDa bifunctional amino-azido polyethylene glycol. Hydrogels were formed using the photodegradable PEG constructs as the sole crosslinkers in the system in combination with four-arm 20 kDa PEG-tetraBCN; gels were made containing a single crosslinker (BODIPY or *o*NB) or an equal mixture of both crosslinkers. The materials were then subjected to rheological analysis (Figure 24).

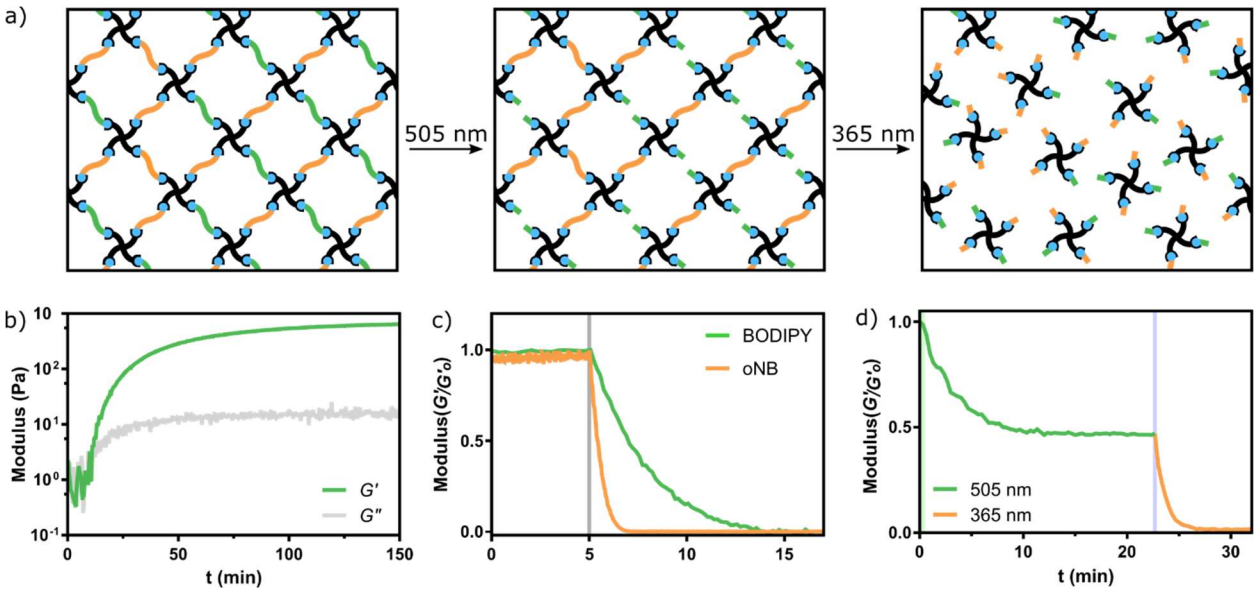

Figure 24. Rheological characterization of BODIPY and *o*NB-crosslinked hydrogels. (b) Typical rheological profile of the PEG-based hydrogel system. (c) Rheological profile illustrating degradation upon light irradiation (BODIPY, 505 nm; *o*NB, 365 nm). Light exposure begins at t = 5 min, indicated by a vertical line. (d) Degradation profile of the BODIPY and *o*NB multicomponent gels. Light exposures begin at t = 0 min (505 nm) and t = 22 min (365 nm) indicated by vertical lines. A reduction of roughly 50% of the storage modulus is observed after the first light exposure followed by complete gel degradation after the second exposure.

The hydrogels typically reached 90% of their maximum storage modulus, after about 1.5 hours (Figure 24b) at which time they were subjected to irradiation with light. Both *o*NB- and BODIPY-based gels responded as expected to irradiation with light at their respective wavelength (*o*NB: 365 nm, 10 mW cm^{-2}; BODIPY: 505 nm, 20 mW cm^{-2}; Figure 24c). The material response was roughly an order of magnitude faster than what was expected based on the in-solution kinetics, indicating the BODIPY photodegradation may be highly context dependent. In any case, the mixed materials, containing an equivalent amount of *o*NB and BOIDPY crosslinkers, behaved as expected when exposed to sequential light irradiation. The material slowly degrades under 505 nm light (20 mW cm^{-2}) over the course of several minutes, reaching about half the initial storage modulus. After 20 minutes, the wavelength was switched to 365 nm and the *o*NB crosslinker rapidly cleaved, reducing the storage modulus to its minimum value as the gel completely degraded (Figure 24d).

4.9 BODIPY pH sensitivity

During synthesis, it was discovered that the BODIPY molecule is extremely sensitive to changes in pH. The typical coupling method consists of dialysis in DIH_2O against a 3 kDa membrane for 48 hours. Unbuffered water resulted in cleavage of the small molecule over that interval. Further exploration of this observation BODIPY-based hydrogels, containing 100% BODIPY crosslinker were incubated in 1xPBS over 48 hours. No material degradation was observed. Upon the addition of acetic acid to lower the pH, the hydrogel rapidly degraded in less than 5 minutes (data not shown). This could be viewed as a drawback or an advantage. If explored further this sensitivity may find utility in situations where biomolecule release or material degradation under acidic conditions is desired.

4.10 Apoptosis as a model system for sequential biochemical signaling

Several model systems come to mind for demonstrating this system in a complex biological environment. Stem cell differentiation[150,151] and instigating angiogenesis with sequential treatment of vascular endothelial growth factor (VEGF) and sphingosine 1-phosphate (S1P)[152] are prime examples, but these are intricate systems with many inputs and it can be difficult to evaluate their success. The most straightforward approach would seem to be one in which cells could be counted as alive or dead, since assays to measure this output are readily available. It was hypothesized that treating cells with of epidermal growth factor (EGF) or tumor necrosis factor (TNF)-α would promote growth or induce apoptosis, respectively[153], and a combination treatment might rescue cells from death[154]. For TNF-α to effectively trigger the apoptotic pathway a cofactor must be added that stabilizes the TNF receptor and blocks inhibition of apoptosis proteins (XIAP). For this, birinapant was used[155].

HeLa cells were treated with EGF (10 ng/mL), TNF-α (10 ng/mL), birinipant (100 nM), or a combination of those treatments. Cellular activity was measured using a luciferase-based ATP assay[153] and monitored over 48 hours after treatment (Figure 25). As expected, EGF treatment increased cellular metabolism, and a combination of TNF-α and birinapant reduced cellular activity. Interestingly when treating with all three factors (EGF, TNF-α, and birinapant), EGF appears to stave off the reduction of cellular activity for 24 hours, but then a large reduction is observed. When cells are first treated with TNF-α and birinapant followed by EGF, their activity is reduced over the first 24 hours, but does not recover. Surprisingly treating with EGF first followed by TNF-α and birinipant, there is a huge reduction in cellular activity after 48 hours, suggesting that EGF somehow potentiates HeLa cells to apoptosis. This was a very

interesting result because it indicated that the result was not simply the sum of previous treatments but the order in which those treatments were administered influenced the result.

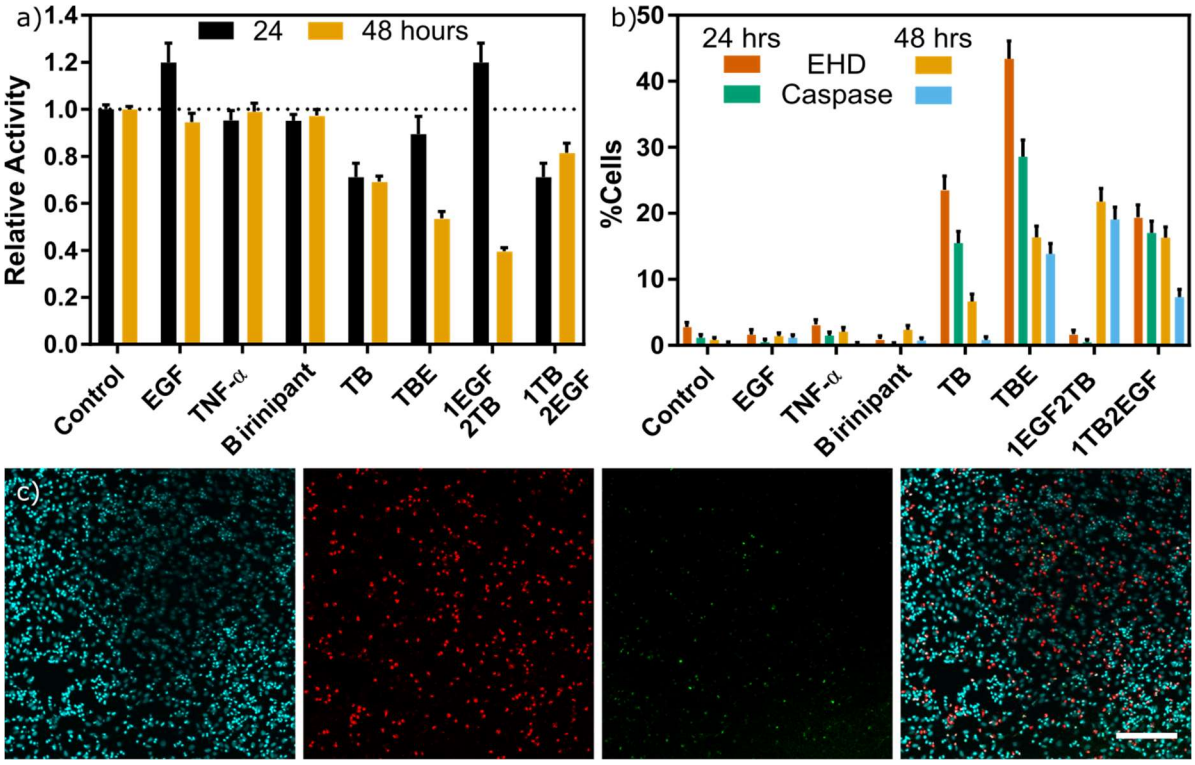

Figure 25. HeLa response to sequential treatment with EGF, TNF-α, and birinapant. (a) The metabolic activity of the cells was measured using an ATP assay under various treatment conditions. Interestingly pretreatment with EGF followed by TNF-α and birinapant elicited a greater response than TNF-α and birinapant alone. (b) Analysis of images in (c). The same general trends were observed as in (a), but this illustrates that the reduction in metabolic activity is the result of cellular death through the apoptotic pathway. Again, pretreatment with EGF appears to potentiate the cells to treatment with TNF-α and birinapant. Error bars in (b) represent the 95% CI about the mean. (c) Cellular response of HeLa cells treated with EGF for 24 hours followed by TNF-α and birinipant for 24 hours. From left to right: DAPI staining of nuclei, caspase 3/7 activity staining,

EHD staining for dead cells, and an overlay of all 3 channels (Scale bar = 100 μm).

These experiments were followed with ethidium homodimer (EHD) and caspase 3/7 assays to determine if the change in cellular activity was due to apoptosis and cell death. Cells were stained *in vitro* and imaged by confocal microscopy. Nuclear stain was used to count total cell number and the fraction of cells that exhibited death (EHD) or caspase activity was determined. The negative controls (no treatment and single inputs) exhibited very low activity, as expected, but the combinatorial treatments were more revealing. Although the difference in outcomes due to the order of treatments was less dramatic under these assays, it is interesting to note that the combination treatment (EGF, TNF-α, and birinapant) displayed significantly higher apoptosis and cell death. In addition, this experiment verified that at least some of the reduction in cellular activity is due to apoptosis and cell death as the treatments bear similar trends in both assays.

So far, the combination of this work with the selective protein release has proved difficult to implement. The coupling of small molecules to proteins has a modest impact on their activity and we suspect the sensitivity of BODIPY is resulting in the non-selective release of protein in a more complex environment.

4.11 A second chance for coumarin

After the orthogonal photochemistry demonstrated in the *o*NB/BODIPY system, we sought to improve on the system by searching for an additional, orthogonal photocage. This would necessitate the synthesis of an additional photocage and could be done to further other associated

research goals. A molecule that absorbs light between 400 and 480 nm would be useful in this regard, especially since the current system does not function in a biological context. The advantages of adding another molecule to our arsenal are twofold. First, it could enable a three-component orthogonal (or semi-orthogonal) system when combined with *o*NB and BODIPY. Second, it could be a more stable alternative to BODIPY for photoorthogonal *in vitro/vivo* work.

Candidates for this work were based on the previous synthesis and analysis of tCM-OH and influenced by other work in the field[142–144] (Table 1). An ideal molecule would have absorbance between 400-480 nm, high quantum yield at that wavelength, but low reactivity at 365 nm. DEAC450[142] has been identified as the most promising molecule for this purpose (Figure 26) and a synthetic approach has been outlined (Scheme 3). The molecule offers an additional advantage in that, similar to NPPOC, it is a tagless photocage, releasing the photocaged molecule in its native state without additional functionalization. By isolating different products of this synthesis, molecules can be made for photocaging small molecules, coupling molecules into hydrogels, or acting as a photodegradable crosslinker in hydrogels.

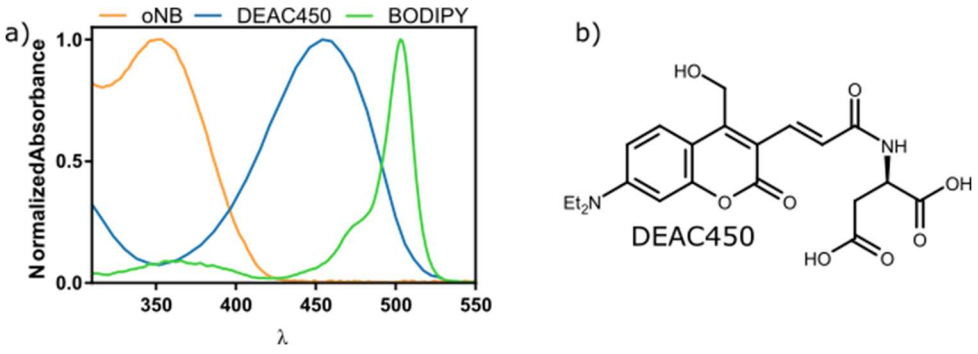

Figure 26. Potential expansion of orthogonal photochemistry. (a) Absorbance profiles of BODIPY, DEAC450, and *o*NB. The maximum absorptions are

different enough that it may be possible to create an orthogonal three component system. (b) Structure of DEAC450.

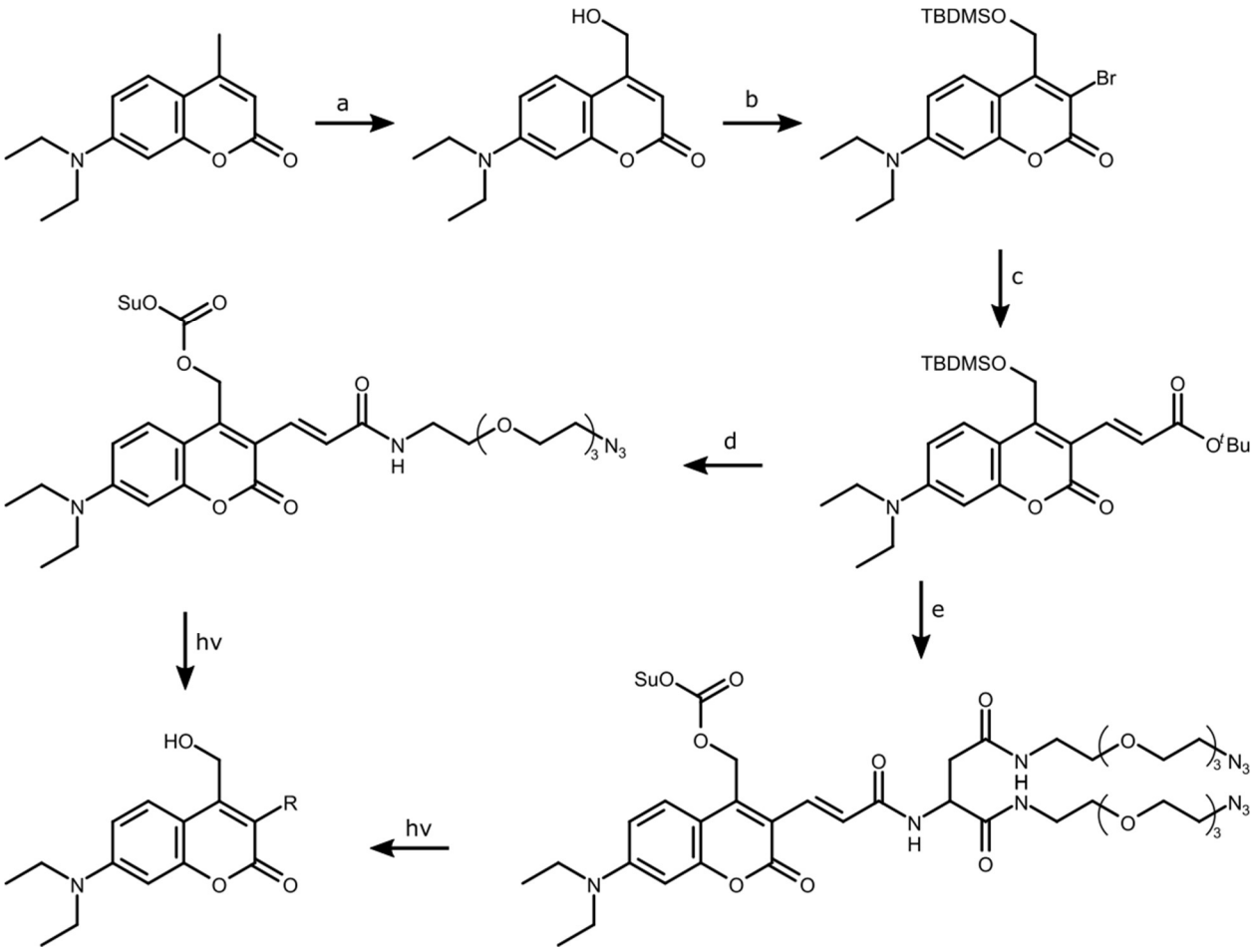

Scheme 3. Proposed synthetic route to N_3-DEAC-NHS[142]. (a) SeO_2. (b) (i) TBDMSCl; (ii) NBS, NaOAc. (c). $Pd(Ph_3)_2$ ^{t}Bu-acrylate. (d) (i) TFA (ii) NHS, EDAC; (iii) 11-Azido-3,6,9-trioxaundecan-1-amine, (iv) TBAF, (v) DSC (e) (i) TFA (ii) Boc-L-glutamate, EDAC, DMAP (iii) 11-Azido-3,6,9-trioxaundecan-1-amine, (iv) TBAF, (v) DSC. Upon light exposure (450 nm) this molecule is expected to cleave, releasing any cargo coupled at position 4.

Unfortunately, after a promising small-scale synthesis that appeared to produce (2E)-N-(2-{2-[2-(2-azidoethoxy)ethoxy]ethoxy}ethyl)-3-[7-(diethylamino)-4-(hydroxymethyl)-2-oxochromen-3-yl]prop-2-enamide (CMOH-PEG-N_3) by mass spectrometry analysis (data not shown), a considerable effort to scale up the synthesis was not successful (Table 3). Many different conditions were attempted based on literature reports of this transformation on this exact substrate[120] or similar substrates[156–158].

When the initial attempts resulted in no reaction, subsequent attempts were made with the intention of forcing the reaction to proceed by increasing catalyst load or increasing temperature, but to no avail. Additional attempts to increase the reactivity of the substrate using more polar solvents or through salt additives proved equally futile as the starting material decomposed under these conditions. Alternative routes were proposed using the 4-methyl instead of the protected alcohol with the thought that perhaps the functionalization either was too bulky, sterically inhibiting the reaction, or the oxidation state made the material too reactive under the more polar conditions. Unfortunately, these attempts also resulted in no reaction. Using an alternative aryl bromide, 3-bromobenzaldehyde, the Heck coupling reaction (^{t}Bu-acrylate, 1.5 eq; benzene; $Pd(OAc)_2$, 0.02 eq; $P(o\text{-}tol)_3$, 0.05 eq; NEt_3, 5 eq; N_2; 80 °C; 4 hrs)[157] proceeded as expected providing the expected product tert-butyl (2E)-3-(3-formylphenyl)prop-2-enoate. Under these same conditions the brominated coumarin did not react and, with the options seemingly exhausted, the project was abandoned.

Table 3. Coumarin Heck coupling conditions

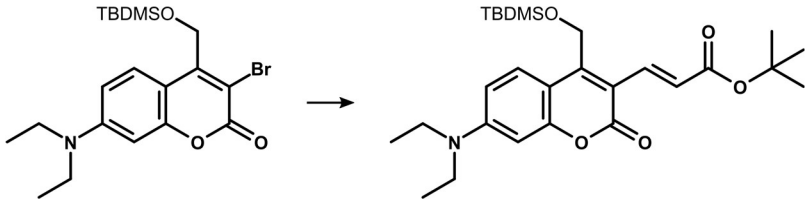

Condition*	Alkene** (eq)	Solvent	Catalyst (eq)	Base (eq)	Salt (eq)	Reductant (eq)	T (°C)	Duration (hrs)	Result
1	1.5	Benzene	$Pd(OAc)_2$ (0.05) $P(o\text{-tol})_3$ (0.06)	NEt_3 (5)	-	CuI (0.05)	80	4	NR
2	1.5	Benzene	$Pd(OAc)_2$ (0.04) $P(o\text{-tol})_3$ (0.06)	NEt_3 (5)	-	CuI (0.03)	80	4	NR
3	1.5	Benzene	$Pd(OAc)_2$ (0.08) $P(o\text{-tol})_3$ (0.12)	NEt_3 (5)	-	CuI (0.03)	80	4	NR
4	3.0	DMF	$Pd(OAc)_2$ (0.05)	$NaHCO_3$ (3)	LiCl (1.7) TBACl (1.1)	-	110	0.5	Degradation
5	3.0	DMF	$Pd(OAc)_2$ (0.05) $P(o\text{-tol})_3$ (0.06)	$NaHCO_3$ (3)	LiCl (1.7) TBACl (1.1)	-	110	0.5	Degradation
6	1.5	NEt_3	$Pd(OAc)_2$ (0.02) $P(o\text{-tol})_3$ (0.03)	NEt_3 (7)	-	-	120	10	Degradation
7	1.0	DMF	$Pd(OAc)_2$ (0.0025) $P(o\text{-tol})_3$ (0.005)	K_2CO_3 (1)	-	-	100	1	Degradation
8	1.5	DMF	$Pd(OAc)_2$ (0.02) $P(o\text{-tol})_3$ (0.05)	NEt_3 (2)	-	-	100	3	Degradation

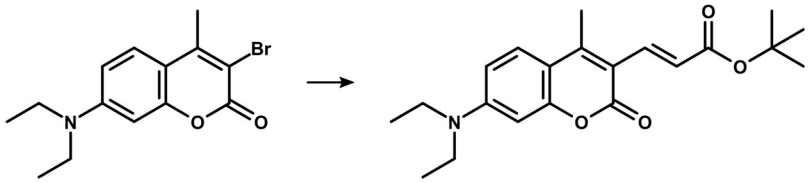

9	1.5	Benzene	$Pd(OAc)_2$ (0.04) $P(o\text{-tol})_3$ (0.06)	NEt_3 (5)	-	CuI (0.034)	80	4	NR
10	1.5	Benzene	$Pd(OAc)_2$ (0.08) $P(o\text{-tol})_3$ (0.12)	NEt_3 (5)	-	CuI (0.034)	80	4	NR

Notes: *See references [120,156–158]

**all reactions used tBu acrylate as alkene substrate.

TBACl - tetrabutyl ammonium chloride;

NR - no reaction

Chapter 5. Conclusions & Future Work

This work presents a clear demonstration of the power of photochemistry applied to biological systems. Although there are two facets to this research, a two proteome sampling approaches and a materials approach, they both rely on photochemistry for spatial control over a sample. In the first case laBONCAT and PAINT offer a deeper, granular understanding of biology, providing spatiotemporal information about the biochemical state of living samples. The second leverages this information to generate dynamic and increasingly complex biomimetic materials.

There is a clear need for more complex materials to apply what we have learned about the complexity of biology to material systems. Yet despite this clear impetus, the development of multifunctional, stimuli-responsive systems has not been forthcoming. To our knowledge, the BODIPY/*o*NB system presented here is the most selective biological demonstration of orthogonal photochemistry to date. Furthermore, the flexibility of this approach allows for any pair of chemicals or biomolecules of interest to be selectively removed or introduced to culture with spatiotemporal control, providing a dramatic improvement to the level of potential complexity when compared with single-input systems.

Using light as a stimulus is a powerful handle that researchers can use with precise control over material interactions with biology. The architecture presented here could also be used to simultaneously control mechanical properties and biochemical cues at any arbitrarily defined interval and location. It is our hope that photoorthogonal systems, such as the work describe here, will unlock new possibilities for future work in the fields of drug delivery and tissue engineering by providing an unprecedented level of control for delivering biochemical cues.

By illustrating the plausibility of creating a photoorthogonal system for biomaterials applications, our hope is that this work with BODIPY and *o*NB will inspire improved designs for wavelength-selective chemistries. Clearly there are more dynamic and heterogeneous signals present in biology than we can currently replicate in materials, so the development of ever more independent stimuli-responsive chemicals remains of utmost importance. The applications for even a simple two-component system like the one described here are extensive. This could include relatively simple systems like the selective release of chemotherapies in response to drug resistance development in tumors or similarly sequential release of antibiotics in response to the emergence of bacterial resistance. Alternatively, we envision making increasingly complex cell culture platforms that offer dynamic biochemical tailorability. Using the information garnered from studying organoid development[159] and building on the work here could provide the next step towards the ultimate goal of regenerative medicine.

The apoptotic system explored here deserves additional investigation. Although the interaction between TNF-α and EGF pathways is well documented[160–163], here an apoptotic response was only elicited upon co-treatment of TNF-α with the SMAC mimetic, birinapant. In addition, pre- or co-treatment with EGF appeared to result in increased cell death when compared with the TNF-α and birinapant treatment. This interaction warrants further investigation.

Two proteomic techniques are described here, laBONCAT and PAINT. The primary unique aspect of these methods is the capability to label the proteome in both time and space. In addition, both can be conducted on living systems. Clearly, PAINT displays enormous advantages over laBONCAT under most situations, especially with respect to spatial resolution, but there are some circumstances where the latter method may be preferential. Since metabolic

incorporation and spatial resolution are coupled in laBONCAT, it has the unique benefit of only labeling proteins in the vicinity of the liberated amino acid. This might be useful in systems with very large cells or cells with long protrusions (e.g., neurons) to differentiate between proteins made in one area of the cell compared to another. Still to be utilized in this regard the basic method requires improvements.

Additional functionalization of amino acids to improve the laBONCAT system is another possible avenue for additional research. This has the potential to expand to multiple wavelengths, as described above, to liberate different amino acids at different positions in culture simultaneously. It would then be possible to locally introduce isotopically labeled amino acids at these locations for simultaneous SILAC analysis, making a direct comparison of different areas in the same culture. Similarly, the laBONCAT method could be expanded by including another ncAA, specifically homopropargyl glycine (Hpg) (Figure 27). Protected Hpg was graciously provided by the Baran group[164], and could be quickly functionalized, but would require the synthesis of another protecting moiety. The stimulus for uncaging does not have to be light, although light is useful for demonstrating the spatial control of the technique, other triggers (e.g., pH[63], oxidative environment, enzymes[100,135], ultrasound[165–167]) could be used to liberate amino acids in cell culture. This would be especially useful for labeling selective areas in heterogeneous tissue samples or *in vivo*.

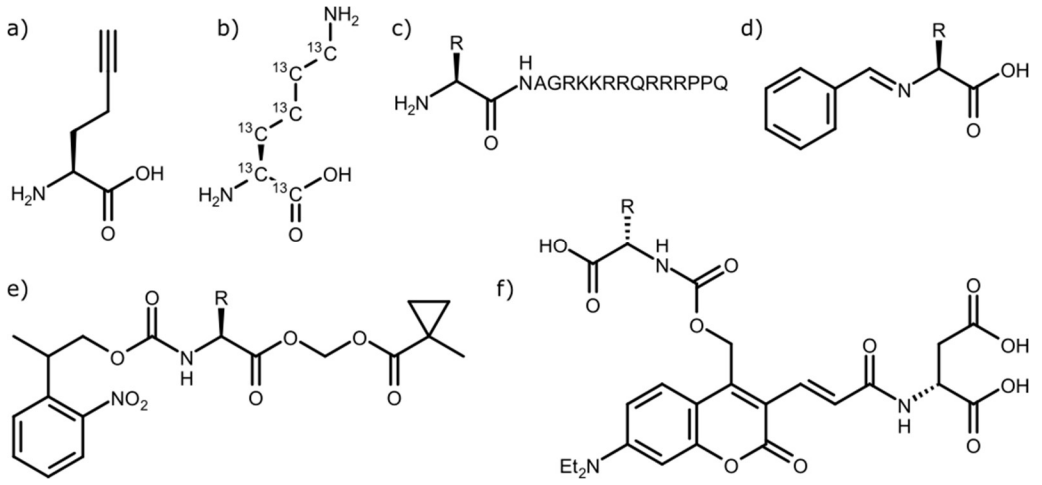

Figure 27. Proposed structural improvements to laBONCAT. (a) Homopropargylglycine (Hpg) is an alternative ncAA that could be used in combination with Aha. (b) Lysine $^{13}C_6$, a heavy isotope amino acid used in SILAC (c) A cell-penetrating peptide[101,102] at the carboxylate would facilitate internalization and prevent incorporation until enzymatic cleavage by peptidases[168]. (d) An imine masking the α-amine would cleave under reduced pH. (e) Additional masking of the carboxylate with an enzymatically cleavable ester[100] is hypothesized to improve cell permeability of the masked amino acid. (f) Photoprotection of amino acids at the α-amine could be accomplished with DEAC450[142] to open an orthogonal wavelength for simultaneous liberation of multiple amino acids in tissue culture. Combinations of these improvements could provide simultaneous sampling in distinct areas *via* multiple uncaging conditions in the same culture.

One additional improvement that is suggested for this system is the masking of both the carboxylate and α-amine to prevent a formal charge on the molecule. It is hypothesized that the formal charge of the carboxylate *in vitro* is responsible for the lack of cell permeability, since cell membranes bear a slightly negative charge and it is difficult for charged molecules to penetrate the bilayer. Masking the carboxylate with an ester that can be selectively cleaved by

endogenous, intercellular esterases[100] might alleviate this problem (Figure 27e). This should facilitate internalization of the ncAA and provide a dramatic improvement to the spatial resolution. This might also be achieved by the addition of a cell-penetrating peptide to the carboxylate[101,102]. If followed by alanine, the ncAA could be selectively cleaved by peptidases after internalization[114].

PAINT, in contrast to laBONCAT, seems to be a more generalizable method. It is a powerful technique leveraging both metabolic pulsing and photoactivation for spatiotemporal labeling of the proteome. The work presented here is a basic demonstration of the method *in vitro* and *in vivo* as a preliminary exploration of the plausibility of such a technique. Our hope is that the method finds utility in helping answer innumerable biological questions.

It follows that the general method can be expanded to include the investigation of new diseases or biological questions, where visible features of interest can be investigated. This may prove especially powerful when measuring proteomic changes associated with features over a treatment duration.

Coupling to fluorescent channels using fluorescent fusions to proteins of interest or through fluorescent antibody labeling, as described here, would provide spatial information about subcellular localization of proteins or processes of interest. This could be achieved by defining an area, structure, object, or protein of interest, creating a fusion protein or selecting an appropriate antibody, then labeling the proteome over the time interval of interest. Using a fluorescent microscope (DMD or two-photon), selective activation of the probe in areas that exhibit fluorescence exceeding a threshold can be used to tag/isolate proteins for analysis.

Parkinson's disease is a logical first model disease for interrogation with this method. The disease state can be modeled *in vitro* with the L84V SOD1-expressing SK-N-SH cell line,

inducing with tunicamycin[169], although alternative methods are also available[170–172]. Using a 2D tissue culture PD model[169–172], a sampling of the proteins associated with Lewy body formation can be investigated over time and the response after treating with stimuli that affect their formation. Despite the poor understanding of disease progression[173], it is often characterized by intracellular α-synuclein aggregation and ubiquitination[11] among other indiators[171]. These markers could be used as positive controls to corroborate other findings of these experiments and it is possible that this demonstration could resolve an ongoing dispute about the role of inclusions and α-synuclein in neurodegenerative disorders[174].

Alternatively (or in addition to), the PAINT method could be applied to other *in vitro* models for disease or expanded into tissue slice culture. Moving into models outside those examined as part of this thesis here may face unforeseen challenges, but may provide a further enhanced understanding of disease in a more native-like environment. In one example, thin slices of brains from disease mice[13,176] or other organisms[177] (~100 μm[175] thick) could be used to study Alzheimer's disease (AD) progression. AD is characterized by extracellular β-amyloid plaque deposition and tau protein hyper phosphorylation, both producing clearly visible features in culture. We anticipate that sampling the proteome via PAINT in a spatially and temporally resolved manner will help establish a better understanding of disease development that can be translated into clinically actionable information.

References

(1) Lander, E. S., Linton, L. M., Birren, B., Nusbaum, C., et al. (2001) Initial sequencing and analysis of the human genome. *Nature 409*, 860–921.

(2) Taniguchi, Y., Choi, P. J., Li, G., Chen, H., et al. (2010) Quantifying E. coli Proteome and Transcriptome with Single-Molecule Sensitivity in Single Cells. *Science 329*, 533–538.

(3) Vogel, C., and Marcotte, E. M. (2012) Insights into the regulation of protein abundance from proteomic and transcriptomic analyses. *Nat. Genet. Rev. 13*, 227–232.

(4) LOWRY, O. H., ROSEBROUGH, N. J., FARR, A. L., and RANDALL, R. J. (1951) Protein measurement with the Folin phenol reagent. *J. Biol. Chem. 193*, 265–275.

(5) Pandey, A., and Mann, M. (2000) Proteomics to study genes and genomes. *Nature 405*, 837–846.

(6) Shahbazi, M. N., Jedrusik, A., Vuoristo, S., Recher, G., et al. (2016) Self-organization of the human embryo in the absence of maternal tissues. *Nat. Cell Biol. 18*, 700–708.

(7) Deglincerti, A., Croft, G. F., Pietila, L. N., Zernicka-Goetz, M., et al. (2016) Self-organization of the in vitro attached human embryo. *Nature 533*, 251–254.

(8) Alizadeh, A. A., Aranda, V., Bardelli, A., Blanpain, C., et al. (2015) Toward understanding and exploiting tumor heterogeneity. *Nat. Med. 21*, 846–853.

(9) Gerdes, M. J., Sood, A., Sevinsky, C., Pris, A. D., et al. (2014) Emerging Understanding of Multiscale Tumor Heterogeneity. *Front. Oncol. 4*, 1–12.

(10) Kim, W. S., Kågedal, K., and Halliday, G. M. (2014) Alpha-synuclein biology in Lewy body diseases. *Alzheimers. Res. Ther. 6*, 73.

(11) Shimohama, S., Sawada, H., Kitamura, Y., and Taniguchi, T. (2003) Disease model: Parkinson's disease. *Trends Mol. Med. 9*, 360–365.

(12) Osterberg, V. R., Spinelli, K. J., Weston, L. J., Luk, K. C., et al. (2015) Progressive Aggregation of Alpha-Synuclein and Selective Degeneration of Lewy Inclusion-Bearing Neurons in a Mouse Model of Parkinsonism. *Cell Rep. 10*, 1252–1260.

(13) Hadley, K. C., Rakhit, R., Guo, H., Sun, Y., et al. (2015) Determining composition of micron-scale protein deposits in neurodegenerative disease by spatially targeted optical microproteomics. *Elife 4*, 1–21.

(14) Sarro, L., Senjem, M. L., Lundt, E. S., Przybelski, S. A., et al. (2016) Amyloid-β deposition and regional grey matter atrophy rates in dementia with Lewy bodies. *Brain 139*, 2740–2750.

(15) Park, S., Yang, J. S., Shin, Y. E., Park, J., et al. (2014) Protein localization as a principal feature of the etiology and comorbidity of genetic diseases. *Mol. Syst. Biol. 7*, 494–494.

(16) Laurila, K., and Vihinen, M. (2009) Prediction of disease-related mutations affecting protein localization. *BMC Genomics 10*, 122.

(17) Funayama, M., Ohe, K., Amo, T., Furuya, N., et al. (2015) CHCHD2 mutations in autosomal dominant late-onset Parkinson's disease: a genome-wide linkage and sequencing study. *Lancet Neurol. 14*, 274–282.

(18) Nalls, M. A., Pankratz, N., Lill, C. M., Do, C. B., et al. (2014) Large-scale meta-analysis of

genome-wide association data identifies six new risk loci for Parkinson's disease. *Nat. Genet. 46*, 989–993.

(19) Karch, C. M., and Goate, A. M. (2015) Alzheimer's disease risk genes and mechanisms of disease pathogenesis. *Biol. Psychiatry 77*, 43–51.

(20) Steinberg, S., Stefansson, H., Jonsson, T., Johannsdottir, H., et al. (2015) Loss-of-function variants in ABCA7 confer risk of Alzheimer's disease. *Nat. Genet. 47*, 445–447.

(21) Alzheimer's Association. (2017) 2017 Alzheimer's disease facts and figures. *Alzheimer's Dement. 13*, 325–373.

(22) Siegel, R. L., Miller, K. D., and Jemal, A. (2017) Cancer statistics, 2017. *CA. Cancer J. Clin. 67*, 7–30.

(23) Cummings, C. A., Peters, E., Lacroix, L., Andre, F., et al. (2016) The Role of Next-Generation Sequencing in Enabling Personalized Oncology Therapy. *Clin. Transl. Sci. 9*, 283–292.

(24) Damodaran, S., Berger, M. F., and Roychowdhury, S. (2015) Clinical Tumor Sequencing: Opportunities and Challenges for Precision Cancer Medicine. *Am. Soc. Clin. Oncol. Educ. B. 35*, 175–182.

(25) Tan, O., Shrestha, R., Cunich, M., and Schofield, D. J. (2018) Application of next-generation sequencing to improve cancer management: A review of the clinical effectiveness and cost-effectiveness. *Clin. Genet.* 1–12.

(26) Aebersold, R., and Mann, M. (2003) Mass spectrometry-based proteomics. *Nature 422*, 198–207.

(27) Domon, B., and Aebersold, R. (2006) Mass spectrometry and protein analysis. *Science 312*, 212–217.

(28) Higgs, R. E., Knierman, M. D., Gelfanova, V., Butler, J. P., et al. (2005) Comprehensive Label-Free Method for the Relative Quantification of Proteins from Biological Samples. *J. Proteome Res. 4*, 1442–1450.

(29) Qattan, A. T., Mulvey, C., Crawford, M., Natale, D. A., et al. (2010) Quantitative organelle proteomics of MCF-7 breast cancer cells reveals multiple subcellular locations for proteins in cellular functional processes. *J. Proteome Res. 9*, 495–508.

(30) Tolbert, N. E. (1974) Isolation of subcellular organelles of metabolism on isopycnic sucrose gradients, in *Methods in Enzymology*, pp 734–746.

(31) Mueller, C., DeCarvalho, A. C., Mikkelsen, T., Lehman, N. L., et al. (2014) Glioblastoma cell enrichment is critical for analysis of phosphorylated drug targets and proteomic-genomic correlations. *Cancer Res. 74*, 818–828.

(32) Snapp, E. (2005) Design and use of fluorescent fusion proteins in cell biology. *Curr. Protoc. Cell Biol. Chapter 21*, 21.4.1-21.4.13.

(33) Gross, A., Schoendube, J., Zimmermann, S., Steeb, M., et al. (2015) Technologies for Single-Cell Isolation. *Int. J. Mol. Sci. 16*, 16897–16919.

(34) Lu, Y., Xue, Q., Eisele, M. R., Sulistijo, E. S., et al. (2015) Highly multiplexed profiling of single-cell effector functions reveals deep functional heterogeneity in response to pathogenic

ligands. *Proc. Natl. Acad. Sci. 112*, 607–615.

(35) Vélez-Bermúdez, I. C., Wen, T. N., Lan, P., and Schmidt, W. (2016) Isobaric Tag for Relative and Absolute Quantitation (iTRAQ)-Based Protein Profiling in Plants, in *Methods in Molecular Biology*, pp 213–221.

(36) Rohner, T. C., Staab, D., and Stoeckli, M. (2005) MALDI mass spectrometric imaging of biological tissue sections. *Mech. Ageing Dev. 126*, 177–185.

(37) Geiger, T., Wisniewski, J. R., Cox, J., Zanivan, S., et al. (2011) Use of stable isotope labeling by amino acids in cell culture as a spike-in standard in quantitative proteomics. *Nat. Protoc. 6*, 147–157.

(38) Baskin, J. M., Prescher, J. A., Laughlin, S. T., Agard, N. J., et al. (2007) Copper-free click chemistry for dynamic in vivo imaging. *Proc. Natl. Acad. Sci. 104*, 16793–16797.

(39) Sandin, M., Antberg, L., Levander, F., and James, P. (2015) A Breast Cell Atlas: Organelle analysis of the MDA-MB-231 cell line by density-gradient fractionation using isotopic marking and label-free analysis. *EuPA Open Proteomics 8*, 68–77.

(40) Foster, L. J., de Hoog, C. L., Zhang, Y., Zhang, Y., et al. (2006) A mammalian organelle map by protein correlation profiling. *Cell 125*, 187–99.

(41) Abramsson, A., Westman-Brinkmalm, A., Pannee, J., Gustavsson, M., et al. (2010) Proteomics profiling of single organs from individual adult zebrafish. *Zebrafish 7*, 161–168.

(42) Kislinger, T., Cox, B., Kannan, A., Chung, C., et al. (2006) Global Survey of Organ and Organelle Protein Expression in Mouse: Combined Proteomic and Transcriptomic Profiling. *Cell 125*, 173–186.

(43) Luxembourg, S. L., Mize, T. H., McDonnell, L. A., and Heeren, R. M. A. (2004) High-Spatial Resolution Mass Spectrometric Imaging of Peptide and Protein Distributions on a Surface. *Anal. Chem. 76*, 5339–5344.

(44) Chaurand, P., Schwartz, S. A., and Caprioli, R. M. (2002) Imaging mass spectrometry: a new tool to investigate the spatial organization of peptides and proteins in mammalian tissue sections. *Curr. Opin. Chem. Biol. 6*, 676–681.

(45) Renaut, P., Boros, S., Loo, D., and Hill, M. (2013) Diagnosis Of Amyloidosis Subtype By Laser-Capture Microdissection (LCM) and Tandem Mass Spectrometry (MS) Proteomic Analysis. *Blood 122*, 5295.

(46) Xue, Q., Lu, Y., Eisele, M. R., Sulistijo, E. S., et al. (2015) Analysis of single-cell cytokine secretion reveals a role for paracrine signaling in coordinating macrophage responses to TLR4 stimulation. *Sci. Signal. 8*, 1–12.

(47) Northen, T. R., Yanes, O., Northen, M. T., Marrinucci, D., et al. (2007) Clathrate nanostructures for mass spectrometry. *Nature 449*, 1033–1036.

(48) Patti, G. J., Woo, H. K., Yanes, O., Shriver, L., et al. (2010) Detection of carbohydrates and steroids by cation-enhanced nanostructure-initiator mass spectrometry (NIMS) for biofluid analysis and tissue imaging. *Anal. Chem. 82*, 121–8.

(49) Zhang, D., MacInkovic, I., Devarie-Baez, N. O., Pan, J., et al. (2014) Detection of protein S-sulfhydration by a tag-switch technique. *Angew. Chemie Int. Ed. 53*, 575–581.

(50) Slade, W. O., Werth, E. G., McConnell, E. W., Alvarez, S., et al. (2015) Quantifying Reversible Oxidation of Protein Thiols in Photosynthetic Organisms. *J. Am. Soc. Mass Spectrom. 26*, 631–640.

(51) Guo, J., Gaffrey, M. J., Su, D., Liu, T., et al. (2014) Resin-assisted enrichment of thiols as a general strategy for proteomic profiling of cysteine-based reversible modifications. *Nat. Protoc. 9*, 64–75.

(52) Rhee, H. W., Zou, P., Udeshi, N. D., Martell, J. D., et al. (2013) Proteomic mapping of mitochondria in living cells via spatially restricted enzymatic tagging. *Science 339*, 1328–1331.

(53) Hörmann, K., Stukalov, A., Müller, A. C., Heinz, L. X., et al. (2016) A Surface Biotinylation Strategy for Reproducible Plasma Membrane Protein Purification and Tracking of Genetic and Drug-Induced Alterations. *J. Proteome Res. 15*, 647–658.

(54) Choe, L., D'Ascenzo, M., Relkin, N. R., Pappin, D., et al. (2007) 8-Plex quantitation of changes in cerebrospinal fluid protein expression in subjects undergoing intravenous immunoglobulin treatment for Alzheimer's disease. *Proteomics 7*, 3651–3660.

(55) Ong, S. E., Blagoev, B., Kratchmarova, I., Kristensen, D. B., et al. (2002) Stable isotope labeling by amino acids in cell culture, SILAC, as a simple and accurate approach to expression proteomics. *Mol. Cell. Proteomics 1*, 376–386.

(56) Larance, M., Ahmad, Y., Kirkwood, K. J., Ly, T., et al. (2013) Global Subcellular Characterization of Protein Degradation Using Quantitative Proteomics. *Mol. Cell. Proteomics 12*, 638–650.

(57) Laughlin, S. T., Agard, N. J., Baskin, J. M., Carrico, I. S., et al. (2006) Metabolic Labeling of Glycans with Azido Sugars for Visualization and Glycoproteomics. *Methods Enzymol. 415*, 230–250.

(58) Kiick, K. L., Saxon, E., Tirrell, D. A., and Bertozzi, C. R. (2002) Incorporation of azides into recombinant proteins for chemoselective modification by the Staudinger ligation. *Proc. Natl. Acad. Sci. 99*, 19–24.

(59) Ngo, J. T., and Tirrell, D. A. (2011) Noncanonical Amino Acids in the Interrogation of Cellular Protein Synthesis. *Acc. Chem. Res. 44*, 677–685.

(60) Dieterich, D. C., Link, A. J., Graumann, J., Tirrell, D. A., et al. (2006) Selective identification of newly synthesized proteins in mammalian cells using bioorthogonal noncanonical amino acid tagging (BONCAT). *Proc. Natl. Acad. Sci. 103*, 9482–9487.

(61) Dieterich, D. C., Lee, J. J., Link, A. J., Graumann, J., et al. (2007) Labeling, detection and identification of newly synthesized proteomes with bioorthogonal non-canonical amino-acid tagging. *Nat. Protoc. 2*, 532–540.

(62) Sletten, E. M., and Bertozzi, C. R. (2009) Bioorthogonal chemistry: fishing for selectivity in a sea of functionality. *Angew. Chemie Int. Ed. 48*, 6974–6998.

(63) Szychowski, J., Mahdavi, A., Hodas, J. J. L., Bagert, J. D., et al. (2010) Cleavable biotin probes for labeling of biomolecules via azide-alkyne cycloaddition. *J. Am. Chem. Soc. 132*, 18351–18360.

(64) Saxon, E. (2000) Cell Surface Engineering by a Modified Staudinger Reaction. *Science (80-*

.). *287*, 2007–2010.

(65) Tornøe, C. W., Christensen, C., and Meldal, M. (2002) Peptidotriazoles on solid phase: [1,2,3]-Triazoles by regiospecific copper(I)-catalyzed 1,3-dipolar cycloadditions of terminal alkynes to azides. *J. Org. Chem. 67*, 3057–3064.

(66) Rostovtsev, V. V., Green, L. G., Fokin, V. V., and Sharpless, K. B. (2002) A Stepwise Huisgen Cycloaddition Process: Copper(I)-Catalyzed Regioselective "Ligation" of Azides and Terminal Alkynes. *Angew. Chemie Int. Ed. 41*, 2596–2599.

(67) Agard, N. J., Prescher, J. A., and Bertozzi, C. R. (2004) A Strain-Promoted [3 + 2] Azide−Alkyne Cycloaddition for Covalent Modification of Biomolecules in Living Systems. *J. Am. Chem. Soc. 126*, 15046–15047.

(68) Dommerholt, J., Schmidt, S., Temming, R., Hendriks, L. J. a, et al. (2010) Readily accessible bicyclononynes for bioorthogonal labeling and three-dimensional imaging of living cells. *Angew. Chemie - Int. Ed. 49*, 9422–9425.

(69) O'Donoghue, P., Ling, J., Wang, Y.-S., and Söll, D. (2013) Upgrading protein synthesis for synthetic biology. *Nat. Chem. Biol. 9*, 594–598.

(70) Neumann, H., Slusarczyk, A. L., and Chin, J. W. (2010) *De Novo* Generation of Mutually Orthogonal Aminoacyl-tRNA Synthetase/tRNA Pairs. *J. Am. Chem. Soc. 132*, 2142–2144.

(71) Link, A. J., Mock, M. L., and Tirrell, D. A. (2003) Non-canonical amino acids in protein engineering. *Curr. Opin. Biotechnol. 14*, 603–609.

(72) Bagert, J. D., Xie, Y. J., Sweredoski, M. J., Qi, Y., et al. (2014) Quantitative, Time-Resolved Proteomic Analysis by Combining Bioorthogonal Noncanonical Amino Acid Tagging and Pulsed Stable Isotope Labeling by Amino Acids in Cell Culture. *Mol. Cell. Proteomics 13*, 1352–1358.

(73) Hansen, M. J., Velema, W. a., Lerch, M. M., Szymanski, W., et al. (2015) Wavelength-selective cleavage of photoprotecting groups: strategies and applications in dynamic systems. *Chem. Soc. Rev. 44*, 3358–3377.

(74) Czerniecki, S. M., Cruz, N. M., Harder, J. L., Menon, R., et al. (2018) High-Throughput Screening Enhances Kidney Organoid Differentiation from Human Pluripotent Stem Cells and Enables Automated Multidimensional Phenotyping. *Cell Stem Cell 22*, 929–940.

(75) Badeau, B. A., Comerford, M. P., Arakawa, C. K., Shadish, J. A., et al. (2018) Engineered modular biomaterial logic gates for environmentally triggered therapeutic delivery. *Nat. Chem. 10*, 251–258.

(76) Szymański, W., Beierle, J. M., Kistemaker, H. A. V., Velema, W. A., et al. (2013) Reversible Photocontrol of Biological Systems by the Incorporation of Molecular Photoswitches. *Chem. Rev. 113*, 6114–6178.

(77) Ruskowitz, E. R., and DeForest, C. A. (2018) Photoresponsive biomaterials for targeted drug delivery and 4D cell culture. *Nat. Rev. Mater. 3*, 17087.

(78) Pianowski, Z. L. (2019) Recent Implementations of Molecular Photoswitches into Smart Materials and Biological Systems. *Chem. – A Eur. J. 25*, 5128–5144.

(79) Griffiths, J. (1972) Photochemistry of Azobenzene and its Derivatives. *Chem. Soc. Rev.*

481–493.

(80) Fedele, C., Netti, P. A., and Cavalli, S. (2018) Azobenzene-based polymers: emerging applications as cell culture platforms. *Biomater. Sci. 6*, 990–995.

(81) Rianna, C., Calabuig, A., Ventre, M., Cavalli, S., et al. (2015) Reversible Holographic Patterns on Azopolymers for Guiding Cell Adhesion and Orientation. *ACS Appl. Mater. Interfaces 7*, 16984–16991.

(82) Baac, H., Lee, J.-H., Seo, J.-M., Park, T. H., et al. (2004) Submicron-scale topographical control of cell growth using holographic surface relief grating. *Mater. Sci. Eng. C 24*, 209–212.

(83) Rosales, A. M., Rodell, C. B., Chen, M. H., Morrow, M. G., et al. (2018) Reversible Control of Network Properties in Azobenzene-Containing Hyaluronic Acid-Based Hydrogels. *Bioconjug. Chem. 29*, 905–913.

(84) Lee, I. N., Dobre, O., Richards, D., Ballestrem, C., et al. (2018) Photoresponsive Hydrogels with Photoswitchable Mechanical Properties Allow Time-Resolved Analysis of Cellular Responses to Matrix Stiffening. *ACS Appl. Mater. Interfaces 10*, 7765–7776.

(85) Rosales, A. M., Mabry, K. M., Nehls, E. M., and Anseth, K. S. (2015) Photoresponsive Elastic Properties of Azobenzene-Containing Poly(ethylene-glycol)-Based Hydrogels. *Biomacromolecules 16*, 798–806.

(86) Onica, V., Miguel, S., Bochet, C. G., and Anzazu Del Campo, A. (2011) Wavelength-Selective Caged Surfaces: How Many Functional Levels Are Possible? *J. Am. Chem. Soc 133*, 5380–5388.

(87) Azagarsamy, M. A., and Anseth, K. S. (2013) Wavelength-Controlled Photocleavage for the Orthogonal and Sequential Release of Multiple Proteins. *Angew. Chemie Int. Ed. 52*, 13803–13807.

(88) Adelmund, S. M., Ruskowitz, E. R., Farahani, P. E., Wolfe, J. V., et al. (2018) Light-Activated Proteomic Labeling via Photocaged Bioorthogonal Non-Canonical Amino Acids. *ACS Chem. Biol. 13*, 573–577.

(89) Larance, M., and Lamond, A. I. (2015) Multidimensional proteomics for cell biology. *Nat. Rev. Mol. Cell Biol. 16*, 269–280.

(90) Beatty, K. E., Fisk, J. D., Smart, B. P., Lu, Y. Y., et al. (2010) Live-Cell Imaging of Cellular Proteins by a Strain-Promoted Azide-Alkyne Cycloaddition. *ChemBioChem 11*, 2092–2095.

(91) Dieterich, D. C., Hodas, J. J., Gouzer, G., Shadrin, I. Y., et al. (2010) In situ visualization and dynamics of newly synthesized proteins in rat hippocampal neurons. *Nat. Neurosci. 13*, 897–905.

(92) Howden, A. J. M., Geoghegan, V., Katsch, K., Efstathiou, G., et al. (2013) QuaNCAT: quantitating proteome dynamics in primary cells. *Nat. Methods 10*, 343–346.

(93) Roth, S., Drewe, W. C., and Thomas, N. R. (2010) A concise and scalable route to L-azidohomoalanine. *Nat. Protoc. 5*, 1967–1973.

(94) DeForest, C. A., and Tirrell, D. A. (2015) A photoreversible protein-patterning approach for guiding stem cell fate in three-dimensional gels. *Nat. Mater. 14*, 523–531.

(95) Bryant, S. J., Nuttelman, C. R., and Anseth, K. S. (2000) Cytocompatibility of UV and

visible light photoinitiating systems on cultured NIH/3T3 fibroblasts in vitro. *J. Biomater. Sci. Polym. Ed. 11*, 439–457.

(96) DeForest, C. A., Polizzotti, B. D., and Anseth, K. S. (2009) Sequential click reactions for synthesizing and patterning three-dimensional cell microenvironments. *Nat. Mater. 8*, 659–664.

(97) DeForest, C. A., and Anseth, K. S. (2011) Cytocompatible click-based hydrogels with dynamically tunable properties through orthogonal photoconjugation and photocleavage reactions. *Nat. Chem. 3*, 925–931.

(98) Wong, D. Y., Ranganath, T., and Kasko, A. M. (2015) Low-Dose, Long-Wave UV Light Does Not Affect Gene Expression of Human Mesenchymal Stem Cells. *PLoS One 10*, 1–21.

(99) Schwanhäusser, B., Gossen, M., Dittmar, G., and Selbach, M. (2009) Global analysis of cellular protein translation by pulsed SILAC. *Proteomics 9*, 205–209.

(100) Tian, L., Yang, Y., Wysocki, L. M., Arnold, A. C., et al. (2012) Selective esterase-ester pair for targeting small molecules with cellular specificity. *Proc. Natl. Acad. Sci. 109*, 4756–4761.

(101) Lai, Y. T., Chang, Y. Y., Hu, L., Yang, Y., et al. (2015) Rapid labeling of intracellular His-tagged proteins in living cells. *Proc. Natl. Acad. Sci. 112*, 2948–2953.

(102) Bechara, C., and Sagan, S. (2013) Cell-penetrating peptides: 20 years later, where do we stand? *FEBS Lett. 587*, 1693–1702.

(103) Ruskowitz, E. R., and DeForest, C. A. (2019) Proteome-wide Analysis of Cellular Response to Ultraviolet Light for Biomaterial Synthesis and Modification. *ACS Biomater. Sci. Eng. 5*, 2111–2116.

(104) Wienholds, E., Kloosterman, W. P., Miska, E., Alvarez-Saavedra, E., et al. (2005) MicroRNA-Directed Cleavage of HOXB8 mRNA. *Science (80-.). 304*, 594–596.

(105) Lawson, N. D., and Weinstein, B. M. (2002) In Vivo Imaging of Embryonic Vascular Development Using Transgenic Zebrafish. *Dev. Biol. 248*, 307–318.

(106) Wittkopp, N., Huntzinger, E., Weiler, C., Sauliere, J., et al. (2009) Nonsense-Mediated mRNA Decay Effectors Are Essential for Zebrafish Embryonic Development and Survival. *Mol. Cell. Biol. 29*, 3517–3528.

(107) Lieschke, G. J., and Currie, P. D. (2007) Animal models of human disease: zebrafish swim into view. *Nat. Rev. Genet. 8*, 353–367.

(108) Antinucci, P., and Hindges, R. (2016) A crystal-clear zebrafish for in vivo imaging. *Sci. Rep. 6*, 29490.

(109) D'Agati, G., Beltre, R., Sessa, A., Burger, A., et al. (2017) A defect in the mitochondrial protein Mpv17 underlies the transparent casper zebrafish. *Dev. Biol. 430*, 11–17.

(110) Hofsteen, P., Plavicki, J., Johnson, S. D., Peterson, R. E., et al. (2013) Sox9b Is Required for Epicardium Formation and Plays a Role in TCDD-Induced Heart Malformation in Zebrafish. *Mol. Pharmacol. 84*, 353–360.

(111) Cross, L. M., Cook, M. A., Lin, S., Chen, J. N., et al. (2003) Rapid Analysis of Angiogenesis Drugs in a Live Fluorescent Zebrafish Assay. *Arterioscler. Thromb. Vasc. Biol. 23*, 911–912.

(112) Yu, Y. A., Oberg, K., Wang, G., and Szalay, A. A. (2003) Visualization of molecular and cellular events with green fluorescent proteins in developing embryos: a review. *Luminescence 18*, 1–18.

(113) Weber, T., and Köster, R. (2013) Genetic tools for multicolor imaging in zebrafish larvae. *Methods 62*, 279–291.

(114) van Geel, R., Pruijn, G. J. M., van Delft, F. L., and Boelens, W. C. (2012) Preventing Thiol-Yne Addition Improves the Specificity of Strain-Promoted Azide–Alkyne Cycloaddition. *Bioconjug. Chem. 23*, 392–398.

(115) Sun, L., Zhu, G., Zhao, Y., Yan, X., et al. (2013) Ultrasensitive and Fast Bottom-up Analysis of Femtogram Amounts of Complex Proteome Digests. *Angew. Chemie Int. Ed. 52*, 13661–13664.

(116) Zhu, Y., Zhao, R., Piehowski, P. D., Moore, R. J., et al. (2018) Subnanogram proteomics: Impact of LC column selection, MS instrumentation and data analysis strategy on proteome coverage for trace samples. *Int. J. Mass Spectrom. 427*, 4–10.

(117) Ludwig, K. R., Sun, L., Zhu, G., Dovichi, N. J., et al. (2015) Over 2300 Phosphorylated Peptide Identifications with Single-Shot Capillary Zone Electrophoresis-Tandem Mass Spectrometry in a 100 min Separation. *Anal. Chem. 87*, 9532–9537.

(118) Liu, L., Shadish, J. A., Arakawa, C. K., Shi, K., et al. (2018) Cyclic Stiffness Modulation of Cell-Laden Protein–Polymer Hydrogels in Response to User-Specified Stimuli Including Light. *Adv. Biosyst. 2*, 1800240.

(119) Farahani, P. E., Adelmund, S. M., Shadish, J. A., and DeForest, C. A. (2017) Photomediated oxime ligation as a bioorthogonal tool for spatiotemporally-controlled hydrogel formation and modification. *J. Mater. Chem. B 5*, 4435–4442.

(120) Olson, J. P., Kwon, H.-B., Takasaki, K. T., Chiu, C. Q., et al. (2013) Optically Selective Two-Photon Uncaging of Glutamate at 900 nm. *J. Am. Chem. Soc. 135*, 5954–5957.

(121) Blanc, A., and Bochet, C. G. (2002) Wavelength-Controlled Orthogonal Photolysis of Protecting Groups. *J. Org. Chem. 67*, 5567–5577.

(122) Bochet, C. G. (2000) Wavelength-selective cleavage of photolabile protecting groups. *Tetrahedron Lett. 41*, 6341–6346.

(123) Lee, C. H., Wu, S. B., Hong, C. H., Yu, H. S., et al. (2013) Molecular Mechanisms of UV-Induced Apoptosis and Its Effects on Skin Residential Cells: The Implication in UV-Based Phototherapy. *Int. J. Mol. Sci. 14*, 6414–6435.

(124) Kloxin, A. M., Benton, J. A., and Anseth, K. S. (2010) In situ elasticity modulation with dynamic substrates to direct cell phenotype. *Biomaterials 31*, 1–8.

(125) Ibsen, S., Zahavy, E., Wrasdilo, W., Berns, M., et al. (2010) A Novel Doxorubicin Prodrug with Controllable Photolysis Activation for Cancer Chemotherapy. *Pharm. Res. 27*, 1848–1860.

(126) Kaplan, J. H., Forbush, B., and Hoffman, J. F. (1978) Rapid photolytic release of adenosine 5'-triphosphate from a protected analog: utilization by the sodium:potassium pump of human red blood cell ghosts. *Biochemistry 17*, 1929–1935.

(127) Gee, K. R., Wieboldt, R., and Hess, G. P. (1994) Synthesis and Photochemistry of a New

Photolabile Derivative of GABA-Neurotransmitter Release and Receptor Activation in the Microsecond Time Region. *J. Am. Chem. Soc. 116*, 8366–8367.

(128) Breitinger, H. G. A., Wieboldt, R., Ramesh, D., Carpenter, B. K., et al. (2000) Synthesis and Characterization of Photolabile Derivatives of Serotonin for Chemical Kinetic Investigations of the Serotonin 5-HT 3 Receptor †. *Biochemistry 39*, 5500–5508.

(129) Paul, A., Jana, A., Karthik, S., Bera, M., et al. (2016) Photoresponsive real time monitoring silicon quantum dots for regulated delivery of anticancer drugs. *J. Mater. Chem. B 4*, 521–528.

(130) Shi, Y., Truong, V. X., Kulkarni, K., Qu, Y., et al. (2015) Light-triggered release of ciprofloxacin from an in situ forming click hydrogel for antibacterial wound dressings. *J. Mater. Chem. B 3*, 8771–8774.

(131) Kohman, R. E., Cha, S. S., Man, H.-Y., and Han, X. (2016) Light-Triggered Release of Bioactive Molecules from DNA Nanostructures. *Nano Lett. 16*, 2781–2785.

(132) Cabane, E., Malinova, V., Menon, S., Palivan, C. G., et al. (2011) Photoresponsive polymersomes as smart, triggerable nanocarriers. *Soft Matter 7*, 9167.

(133) Huynh, C. T., Nguyen, M. K., Tonga, G. Y., Longé, L., et al. (2016) Photocleavable Hydrogels for Light-Triggered siRNA Release. *Adv. Healthc. Mater. 5*, 305–310.

(134) Sarode, B. R., Kover, K., Tong, P. Y., Zhang, C., et al. (2016) Light Control of Insulin Release and Blood Glucose Using an Injectable Photoactivated Depot. *Mol. Pharm. 13*, 3835–3841.

(135) Hu, X., Tian, J., Liu, T., Zhang, G., et al. (2013) Photo-Triggered Release of Caged Camptothecin Prodrugs from Dually Responsive Shell Cross-Linked Micelles. *Macromolecules 46*, 6243–6256.

(136) Kloxin, A. M., Kasko, A. M., Salinas, C. N., and Anseth, K. S. (2009) Photodegradable hydrogels for dynamic tuning of physical and chemical properties. *Science 324*, 59–63.

(137) DeForest, C. A., Polizzotti, B. D., and Anseth, K. S. (2009) Sequential click reactions for synthesizing and patterning three-dimensional cell microenvironments. *Nat Mater 8*, 659–664.

(138) DeForest, C. A., Sims, E. A., and Anseth, K. S. (2010) Peptide-Functionalized Click Hydrogels with Independently Tunable Mechanics and Chemical Functionality for 3D Cell Culture. *Chem. Mater. 22*, 4783–4790.

(139) DeForest, C. A., and Anseth, K. S. (2012) Photoreversible Patterning of Biomolecules within Click-Based Hydrogels. *Angew. Chemie Int. Ed. 51*, 1816–1819.

(140) Arakawa, C. K., Badeau, B. A., Zheng, Y., and DeForest, C. A. (2017) Multicellular Vascularized Engineered Tissues through User-Programmable Biomaterial Photodegradation. *Adv. Mater. 29*, 1703156.

(141) Il'ichev, Y. V., and Wirz, J. (2000) Rearrangements of 2-Nitrobenzyl Compounds. 1. Potential Energy Surface of 2-Nitrotoluene and Its Isomers Explored with ab Initio and Density Functional Theory Methods. *J. Phys. Chem. A 104*, 7856–7870.

(142) Olson, J. P., Banghart, M. R., Sabatini, B. L., and Ellis-Davies, G. C. R. (2013) Spectral evolution of a photochemical protecting group for orthogonal two-color uncaging with visible light. *J. Am. Chem. Soc. 135*, 15948–15954.

(143) Azagarsamy, M. A., McKinnon, D. D., Alge, D. L., and Anseth, K. S. (2014) Coumarin-Based Photodegradable Hydrogel: Design, Synthesis, Gelation, and Degradation Kinetics. *ACS Macro Lett. 3*, 515–519.

(144) Fournier, L., Gauron, C., Xu, L., Aujard, I., et al. (2013) A blue-absorbing photolabile protecting group for in vivo chromatically orthogonal photoactivation. *ACS Chem. Biol. 8*, 1528–1536.

(145) Umeda, N., Takahashi, H., Kamiya, M., Ueno, T., et al. (2014) Boron Dipyrromethene As a Fluorescent Caging Group for Single-Photon Uncaging with Long-Wavelength Visible Light. *ACS Chem. Biol. 9*, 2242–2246.

(146) Kumari, P., Kulkarni, A., Sharma, A. K., and Chakrapani, H. (2018) Visible-Light Controlled Release of a Fluoroquinolone Antibiotic for Antimicrobial Photopharmacology. *ACS Omega 3*, 2155–2160.

(147) Sunahara, H., Urano, Y., Kojima, H., and Nagano, T. (2007) Design and Synthesis of a Library of BODIPY-Based Environmental Polarity Sensors Utilizing Photoinduced Electron-Transfer-Controlled Fluorescence ON/OFF Switching. *J. Am. Chem. Soc. 129*, 5597–5604.

(148) Akrap, N., Seidel, T., and Barisas, B. G. (2010) Förster distances for fluorescence resonant energy transfer between mCherry and other visible fluorescent proteins. *Anal. Biochem. 402*, 105–106.

(149) Albertazzi, L., Arosio, D., Marchetti, L., Ricci, F., et al. (2009) Quantitative FRET Analysis With the E ^{0} GFP-mCherry Fluorescent Protein Pair. *Photochem. Photobiol. 85*, 287–297.

(150) Burridge, P. W., Matsa, E., Shukla, P., Lin, Z. C., et al. (2014) Chemically defined generation of human cardiomyocytes. *Nat. Methods 11*, 855–860.

(151) Freedman, B. S., Brooks, C. R., Lam, A. Q., Fu, H., et al. (2015) Modelling kidney disease with CRISPR-mutant kidney organoids derived from human pluripotent epiblast spheroids. *Nat. Commun. 6*, 1–13.

(152) Tengood, J. E., Kovach, K. M., Vescovi, P. E., Russell, A. J., et al. (2010) Sequential delivery of vascular endothelial growth factor and sphingosine 1-phosphate for angiogenesis. *Biomaterials 31*, 7805–7812.

(153) Benetatos, C. A., Mitsuuchi, Y., Burns, J. M., Neiman, E. M., et al. (2014) Birinapant (TL32711), a Bivalent SMAC Mimetic, Targets TRAF2-Associated cIAPs, Abrogates TNF-Induced NF- B Activation, and Is Active in Patient-Derived Xenograft Models. *Mol. Cancer Ther. 13*, 867–879.

(154) Assefa, Z., Vantieghem, A., Declercq, W., Vandenabeele, P., et al. (1999) The Activation of the c-Jun N-terminal Kinase and p38 Mitogen-activated Protein Kinase Signaling Pathways Protects HeLa Cells from Apoptosis Following Photodynamic Therapy with Hypericin. *J. Biol. Chem. 274*, 8788–8796.

(155) Krepler, C., Chunduru, S. K., Halloran, M. B., He, X., et al. (2013) The Novel SMAC Mimetic Birinapant Exhibits Potent Activity against Human Melanoma Cells. *Clin. Cancer Res. 19*, 1784–1794.

(156) Pottie, I. R., Nandaluru, P. R., Benoit, W. L., Miller, D. O., et al. (2011) Synthesis of 6 H -

Dibenzo[b , d]pyran-6-ones Using the Inverse Electron Demand Diels–Alder Reaction. *J. Org. Chem. 76*, 9015–9030.

(157) Thaler, F., Colombo, A., Mai, A., Amici, R., et al. (2010) Synthesis and Biological Evaluation of *N* -Hydroxyphenylacrylamides and *N* -Hydroxypyridin-2-ylacrylamides as Novel Histone Deacetylase Inhibitors. *J. Med. Chem. 53*, 822–839.

(158) Nadri, S., Joshaghani, M., and Rafiee, E. (2009) Biphenyl-based phosphine: A well-defined, air-stable, and efficient ligand for the Mizoroki–Heck reaction. *Appl. Catal. A Gen. 362*, 163–168.

(159) Truskey, G. A. (2018) Human Microphysiological Systems and Organoids as in Vitro Models for Toxicological Studies. *Front. public Heal. 6*, 185.

(160) Izumi, H., Ono, M., Ushiro, S., Kohno, K., et al. (1994) Cross Talk of Tumor Necrosis Factor-α and Epidermal Growth Factor in Human Microvascular Endothelial Cells. *Exp. Cell Res. 214*, 654–662.

(161) Modi, S., Kir, D., Banerjee, S., and Saluja, A. (2016) Control of Apoptosis in Treatment and Biology of Pancreatic Cancer. *J. Cell. Biochem. 117*, 279–288.

(162) Son, D. S., Kabir, S. M., Dong, Y., Lee, E., et al. (2013) Characteristics of chemokine signatures elicited by EGF and TNF in ovarian cancer cells. *J. Inflamm. 10*, 25.

(163) McElroy, S. J., Frey, M. R., Yan, F., Edelblum, K. L., et al. (2008) Tumor necrosis factor inhibits ligand-stimulated EGF receptor activation through a TNF receptor 1-dependent mechanism. *Am. J. Physiol. Liver Physiol. 295*, G285–G293.

(164) Smith, J. M., Qin, T., Merchant, R. R., Edwards, J. T., et al. (2017) Decarboxylative Alkynylation. *Angew. Chemie Int. Ed. 56*, 11906–11910.

(165) Berkowski, K. L., Potisek, S. L., Hickenboth, C. R., and Moore, J. S. (2005) Ultrasound-Induced Site-Specific Cleavage of Azo-Functionalized Poly(ethylene glycol). *Macromolecules 38*, 8975–8978.

(166) Wang, J., Pelletier, M., Zhang, H., Xia, H., et al. (2009) High-Frequency Ultrasound-Responsive Block Copolymer Micelle. *Langmuir 25*, 13201–13205.

(167) Fritze, U. F., and von Delius, M. (2016) Dynamic disulfide metathesis induced by ultrasound. *Chem. Commun. 52*, 6363–6366.

(168) Wang, A., Winblade Nairn, N., Johnson, R. S., Tirrell, D. A., et al. (2008) Processing of N-Terminal Unnatural Amino Acids in Recombinant Human Interferon-β inEscherichia coli. *ChemBioChem 9*, 324–330.

(169) Yamagishi, S., Koyama, Y., Katayama, T., Taniguchi, M., et al. (2007) An In Vitro Model for Lewy Body-Like Hyaline Inclusion/Astrocytic Hyaline Inclusion: Induction by ER Stress with an ALS-Linked SOD1 Mutation. *PLoS One* (Li, X.-J., Ed.) *2*, e1030.

(170) Borland, M. K., Trimmer, P. A., Rubinstein, J. D., Keeney, P. M., et al. (2008) Chronic, low-dose rotenone reproduces Lewy neurites found in early stages of Parkinson's disease, reduces mitochondrial movement and slowly kills differentiated SH-SY5Y neural cells. *Mol. Neurodegener. 3*, 21.

(171) Xicoy, H., Wieringa, B., and Martens, G. J. M. (2017) The SH-SY5Y cell line in

Parkinson's disease research: a systematic review. *Mol. Neurodegener. 12*, 1–11.

(172) Cavaliere, F., Cerf, L., Dehay, B., Ramos-Gonzalez, P., et al. (2017) In vitro α-synuclein neurotoxicity and spreading among neurons and astrocytes using Lewy body extracts from Parkinson disease brains. *Neurobiol. Dis. 103*, 101–112.

(173) Compta, Y., and Martí, M. J. (2017) Parkinson disease: What goes around comes around: cognitive impairment as prodromal parkinsonism? *Nat. Rev. Neurol. 13*, 709–710.

(174) Stefanis, L. (2012) alpha-Synuclein in Parkinson's disease. *Cold Spring Harb. Perspect. Med. 2*, 1–23.

(175) Humpel, C. (2015) Organotypic brain slice cultures: A review. *Neuroscience 305*, 86–98.

(176) Chang, P. V, Prescher, J. A., Sletten, E. M., Baskin, J. M., et al. (2010) Copper-free click chemistry in living animals. *Proc. Natl. Acad. Sci. 107*, 1821–1826.

(177) LaFerla, F. M., and Green, K. N. (2012) Animal models of Alzheimer disease. *Cold Spring Harb. Perspect. Med. 2*, 1–13.

(178) Kloxin, A. M., Tibbitt, M. W., and Anseth, K. S. (2010) Synthesis of photodegradable hydrogels as dynamically tunable cell culture platforms. *Nat. Protoc. 5*, 1867–1887.

(179) Kurono, M., Shimomura, A., and Isobe, M. (2004) Synthesis of photoaffinity probes of tautomycin. *Tetrahedron 60*, 1773–1780.

(180) Ma, Y., Zhu, C., Ma, P., and Yu, K. T. (2005) Studies on the Diffusion Coefficients of Amino Acids in Aqueous Solutions. *J. Chem. Engneering Data 50*, 1192–1196.

(181) Kuzmin, A., Poloukhtine, A., Wolfert, M. A., and Popik, V. V. (2010) Surface functionalization using catalyst-free azide-alkyne cycloaddition. *Bioconjug. Chem. 21*, 2076–2085.

(182) Dirksen, A., Hackeng, T. M., and Dawson, P. E. (2006) Nucleophilic catalysis of oxime ligation. *Angew. Chemie Int. Ed. 45*, 7581–7584.

(183) Dirksen, A., and Dawson, P. E. (2008) Rapid oxime and hydrazone ligations with aromatic aldehydes for biomolecular labeling. *Bioconjug. Chem. 19*, 2543–2548.

(184) Rösli, C., Rybak, J. N., Neri, D., and Elia, G. (2008) Quantitative recovery of biotinylated proteins from streptavidin-based affinity chromatography resins. *Methods Mol. Biol. 418*, 89–100.

Appendix A Supplementary Information

General experimental information

Chemical reagents and solvents were purchased from either Sigma-Aldrich or Fisher Scientific and used as received.

Several light sources were used in these experiments. For all single-exposure experiments (kinetics, patterning, release), a Lumen Dynamics OmniCure S1500 Spot UV Curing system with an internal 365 nm filter and an external 360 nm cut-on longpass filter (365 nm) or a Thorlabs M505L3-C1 collimated LED (505 nm) was utilized. Light intensity was measured using a Cole-Parmer Series 9811 radiometer (365 nm) or a Lumen Dynamics Omnicure R2000 radiometer (505 nm). Fluorescence readings were acquired on a SpectraMax M5 spectrophotometer using Thermo Scientific Nunc Black polypropylene 96-well plates.

Rheological measurements of single component materials were performed on a TA Instruments Discovery HR-2 rheometer equipped with a UV curing accessory (365 nm) or a custom-made rheometer stage utilizing an embedded 505 nm LED[118]. The rheological properties of multicomponent samples were analyzed on an Anton Paar MCR-301 rheometer equipped with a parallel-plate geometry (diameter = 8 mm) equipped with a transparent lower geometry. Light was irradiated up through the sample using a Mightex WheeLED Wavelength-Switchable LED Source (505 and 365 nm).

Confocal microscopy was performed at the University of Washington Keck Microscopy Center on a Leica SP8X confocal microscope. Two-photon microscopy and lithography was

performed at the University of Washington Lynn & Mike Garvey Imaging Core on an Olympus FV1000 MPE BX61 Multi-photon Microscope.

Synthesis of previously described compounds utilized in this study

Synthesis of N_3-*o*NB-OSu

N_3-*o*NB-OSu was synthesized as described previously[97,178].

Synthesis of BCN-OSu

(1*R*,8*S*,9*s*)-bicyclo[6.1.0]non-4-yn-9-ylmethyl (2,5-dioxopyrrolidin-1-yl) carbonate (BCN-OSu) was synthesized as described previously[68,94].

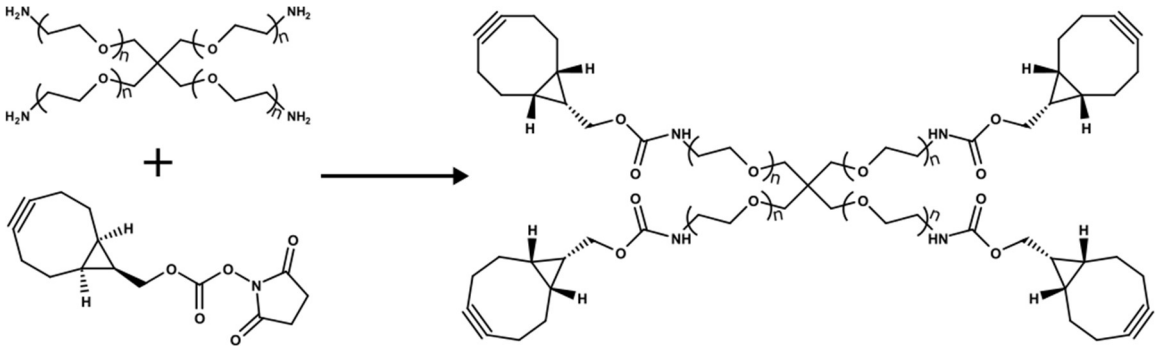

Synthesis of PEG-tetraBCN

4-arm-PEG_{20kDa}-tetrabicyclononyne was synthesized as described previously[94,118].

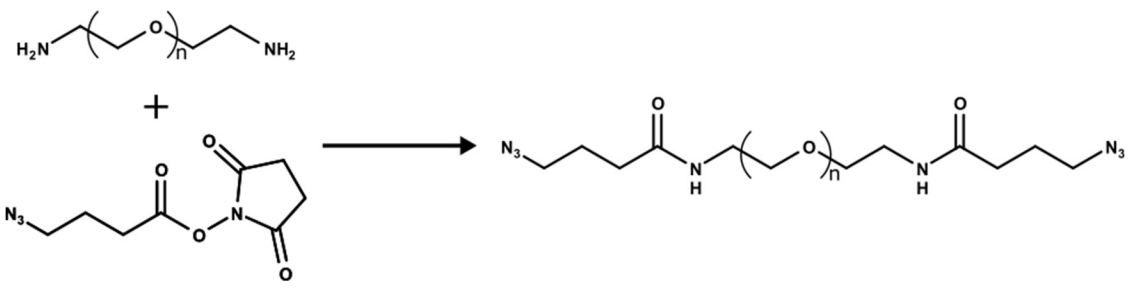

Synthesis of N_3-PEG-N_3

$PEG_{3.5kDa}$diazide was synthesized as described previously[118].

Production of fluorescent proteins

Fluorescent proteins were generated as described previously[119].

FAM-aldehyde, a carboxyfluorescein derivative was graciously provided by Dr. Cole DeForest.

Synthesis of 2,5-dioxopyrrolidin-1-yl 2-[({[2-(2-nitrophenyl)propoxy]carbonyl} amino)oxy]acetate (IV), a 2-(2-nitrophenyl)propyloxycarbonyl NHS activated ester (NPPOC-NHS) photolabile group and 4-azido-2-({[2-(2-nitrophenyl) propoxy]carbonyl}amino)butanoic acid (XV), a photocaged azidohomoalanine (AHA-PL). IV has been synthesized previously by our group[94].

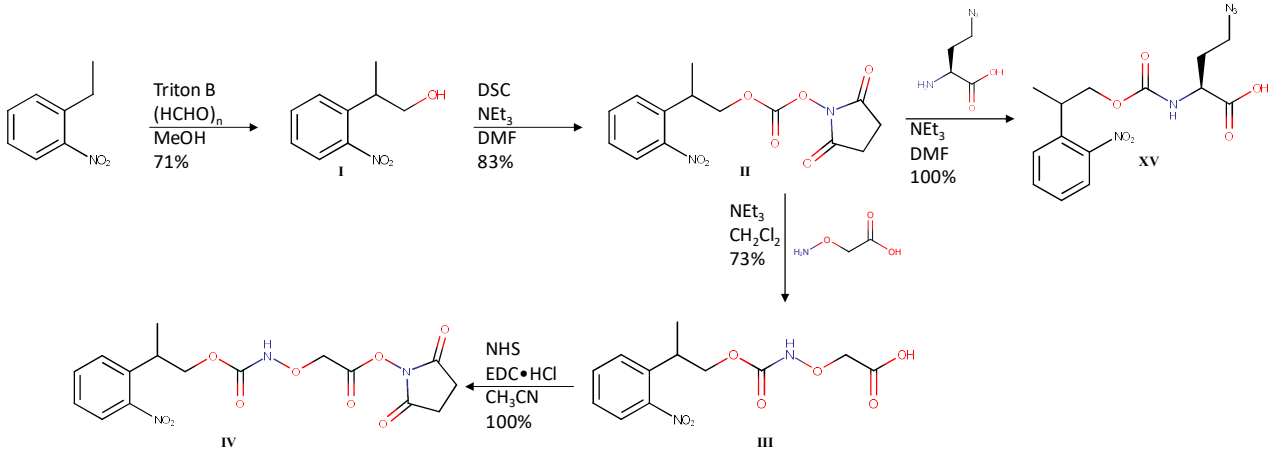

Scheme A1. Synthesis of NPPOC-Aha and NPPOC-NO-NHS.

Synthesis of 2-(2-nitrophenyl)propan-1-ol (I).

618 mg (20.6 mmol) of paraformaldehyde was added to a round bottom flask equipped with a magnetic stirbar. 2 mL (14.9 mmol) of commercially available 1-ethyl-2-nitrobenzene was added followed by 7 mL (15.4 mmol) 40% benzyltrimethylammonium hydroxide in MeOH. The reaction was stirred overnight at 60 °C. The reaction solution was neutralized to pH 7 with 1 N HCl and extracted with 3x30 mL EtOAc. The organic layers were combined, dried with $MgSO_4$, and concentrated. The crude residue was purified by flash column chromatography, eluting with a step gradient 4:1, 3:1, 2:1 hexane:EtOAc. 1.93 g obtained; 71% yield.

Synthesis of 2,5-dioxopyrrolidin-1-yl 2-(2-nitrophenyl)propyl carbonate (II).

4.12 g (16.1 mmol) of disuccinimidyl carbonate were dissolved in 45 mL anhydrous DMF under a N_2 atmosphere. This solution was added to a reaction flask containing 1.93 g (10.7 mmol) of **I**

via syringe. 7 mL (50 mmol) NEt_3 was added via syringe. The reaction was sealed and stirred overnight at room temperature. The solution was concentrated under high vacuum and the residue was purified by flash column chromatography, eluting with a step gradient 4:1, 3:1, 2:1 hexane:EtOAc. 2.83 g obtained; 83% yield. ^{1}H NMR (500 MHz, $CDCl_3$): δ 7.84, (1H, d, J=8.2 Hz), 7.64 (1H, t, J=7.6 Hz), 7.52 (1H, d, J=7.8 Hz), 7.44 (1H, t, J=7.6 Hz), 4.53 (2H, cm), 3.81 (1H, m, J=6.7 Hz), 2.83 (4H, s), 2.06 (2H, s), 1.45 (3H, d, J=6.9 Hz).

Synthesis of 3-({[2-(2-nitrophenyl)propoxy]carbonyl}amino)propanoic acid (III).

3.3 g (10.2 mmol) of commercially available aminooxy acetic acid was dissolved in anhydrous 100 mL CH_2Cl_2 and 12 mL (86 mmol) anhydrous NEt_3 and placed under N_2. Separately, **II** was dissolved in 50 mL anhydrous CH_2Cl_2 under N_2. The solution of aminooxy acetic acid was then added via syringe and the reaction was stirred at room temperature overnight protected from light. Next, the solvent was removed on high vacuum. The residue was redissolved in DI H_2O and washed with 2x100 mL EtOAc. The organic layers were discarded. The aqueous layer was reduced to 0 °C and titrated to pH<1 with 5 M HCl. A white precipitate was observed. The product was extracted from the aqueous phase with 3x100 mL EtOAc, the organic layers were combined, dried with $MgSO_4$, and concentrated under high vacuum. The residue was purified by column flash chromatography, eluting with 20:1 hexane:EtOAc. 2.24 g obtained; 73% yield. ^{1}H NMR (500 MHz, $CDCl_3$): δ 8.04 (1H, s), 7.80 (1H, d, J=8.1 Hz), 7.62 (1H, t, J=7.7 Hz), 7.49 (1H, d, J=8.1), 7.43 (1H, t, J=8.0 Hz), 4.47 (2H, s), 4.40 (1H, cm), 4.31 (1H, cm), 3.78 (1H, m, J=6.1 Hz), 1.40 (3H, d, J=7.0 Hz).

Synthesis of 2,5-dioxopyrrolidin-1-yl 3-({[2-(2-nitrophenyl)propoxy]carbonyl}amino) propanoate (IV).

2.24 g (7.5 mmol) of III, 1.3 g (11.3 mmol) N-hydroxysuccinimide (NHS) and 2.65 g (13.8 mmol) EDC·HCl were added to a reaction flask. 15 mL CH_3CN was added and the reaction was stirred overnight at room temperature protected from light. The reaction solution was concentrated under high vacuum and redissolved in CH_2Cl_2. The solution was then washed with 3x100 mL DI H_2O. The organic layer was collected, dried with $MgSO_4$, and concentrated under high vacuum. 2.92 g obtained; Quantitative yield. ^{1}H NMR (500 MHz, $CDCl_3$): δ 7.79 (1H, cm), 7.62 (1H, cm), 7.52 (1H, cm), 7.42 (1H, cm), 4.49 (4H, cm), 3.75 (1H, cm), 2.87 (4H, cm), 1.74 (1H, br s), 1.41 (3H, cm).

Synthesis of (2S)-4-azido-2-({[2-(2-nitrophenyl)propoxy]carbonyl}amino)butanoic acid (XV).

10 mg (0.055 mmol) of azidohomoalanine (**XIV**) was added to a reaction vial. 21 mg (0.075 mmol) of **II** was dissolved in DMF and added to the reaction via syringe. 0.05 mL (0.36 mmol) NEt_3 was added and the reaction was stirred overnight at room temperature protected from light. The reaction was concentrated under high vacuum and the residue was purified by flash column chromatography eluting with 10:0.5 CH_2Cl_2:MeOH 0.5% AcOH. 17 mg obtained; Quantitative yield. ^{1}H NMR (500 MHz, D_6-DMSO): δ 7.84 (1H, d, J=4.9 Hz), 7.71 (2H, s), 7.46 (1H, d, J=29.0 Hz), 4.19 (2H, cm), 3.98 (1H, s), 3.42 (2H, cm), 3.32 (1H, cm), 1.92 (1H, s), 1.80 (1H, s), 1.29 (3H, s). MS result: 350.087; expected: 350.111.

Synthesis of (2S)-4-azido-2-({[2-(2-nitrophenyl)propoxy]carbonyl}amino)butanoic acid (NPPOC-Aha)

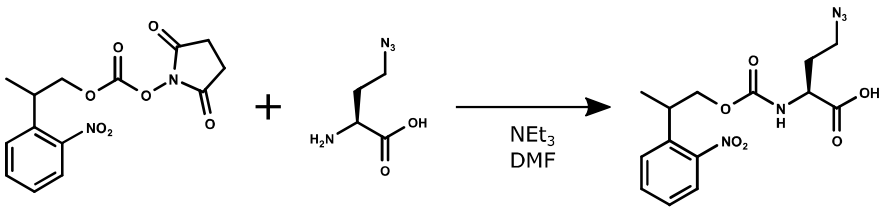

L-Azidohomoalanine (Aha)[93] and NPPOC-NHS[94] were synthesized as described previously. Aha-HCl salt (10 mg, 0.055 mmol) was added to a reaction vial. NPPOC-NHS (20.7 mg, 0.64 mmol) was dissolved in dry dimethylformamide (DMF, 1 mL, Acros, AC326870010) and added to the vial containing Aha-HCl. Dry triethylamine (NEt_3, 0.05 mL, 0.36 mmol; Sigma, 471283) was added *via* syringe, and the components stirred overnight at room temperature. The reaction mixture was then concentrated under reduced pressure and dissolved in 30% acetonitrile (CH_3CN) in deionized water (dH_2O). The product was purified by reverse-phase high-performance liquid chromatography (HPLC), eluting with a CH_3CN/dH_2O gradient ramping from 30% to 100% CH_3CN over 55 minutes. 20 mg of pure product (denoted NPPOC-Aha) was obtained; quantitative yield. ^1H NMR (500 MHz, CD_3OD) δ 7.66 (1H, d, J=8.37 Hz), 7.53 (2H, cm), 7.33 (1H, m, J=4.05 Hz), 4.14 (3H, cm), 3.49 (1H, m, J=6.8 Hz), 3.29 (2H, cm), 1.96 (1H, cm), 1.74 (1H, cm) 1.25 (3H, dd, J=3.3 Hz). HRMS (ESI+) calculated for $C_{14}H_{18}N_5O_6$ [M + 1H]+, 352.1257; observed 352.1259 (Δ = 0.6 ppm).

Synthesis of 5-{[5-({[(1R,8S,9S)-bicyclo[6.1.0]non-4-yn-9-ylmethoxy]carbonyl}amino) pentyl] carbamoyl}-2-(3-hydroxy-6-oxoxanthen-9-yl)benzoic acid (FAM-BCN)

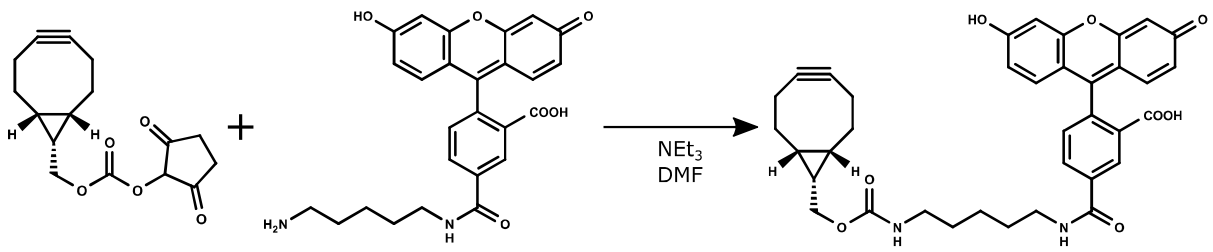

A fluorescent bicyclononyne was necessary for labeling the metabolic incorporation of Aha. (1R,8S,9s)-bicyclo[6.1.0]non-4-yn-9-ylmethyl (2,5-dioxopyrrolidin-1-yl) carbonate[94] (BCN-OSu) was synthesized as described previously.[68] 5(6)-Carboxyfluorescein cadaverine (20 mg, 0.035 mmol; AAT Bioquest, 127) and BCN-OSu (15 mg, 0.052 mmol) were combined in a reaction vial. The reactants were dissolved in dry DMF (1.5 mL) and dry NEt_3 (0.05 mL, 0.36 mmol) was added *via* syringe. The solution was a red suspension until the addition of NEt_3. After one hour, the reaction was dark orange and translucent. The reaction was left stirring overnight at room temperature. The reaction was then concentrated under reduced pressure and dissolved in 50:50 dH_2O:CH_3CN. The product was purified by reverse-phase HPLC, eluting with a CH_3CN/dH_2O gradient ramping from 40% to 80% CH_3CN over 55 minutes. 25 mg of pure product (denoted FAM-BCN) was obtained; quantitative yield. HRMS (ESI+) calculated for $C_{37}H_{37}N_2O_8$ [M + 1H]+, 637.2550; observed 637.2556 (Δ = 0.9 ppm).

Synthesis of Benzaldehyde-functionalized 4-arm PEG.

2,5-dioxopyrrolidin -1-yl 4-formylbenzoate was synthesized as described previously[94].

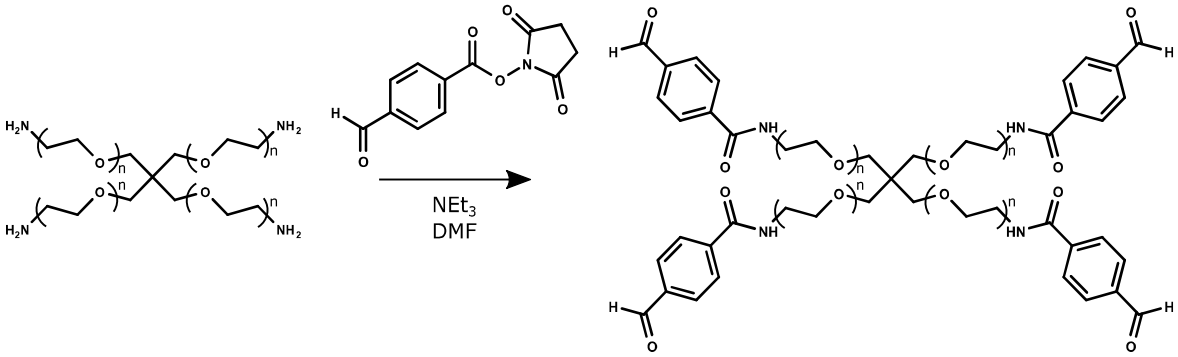

4-arm PEG-amine (524 mg, 0.0524 mmol, Mn ~ 10 kDa) and 2,5-dioxopyrrolidin-1-yl 4-formylbenzoate (78 mg, 0.32 mmol) were added to a round-bottom flask under Ar. The reactants were dissolved in anhydrous DMF (2.62 mL), N,N-diisopropylethylamine (150 µL, 0.86 mmol) was added, and the reaction was stirred overnight at room temperature. dH_2O (9 mL) was added to the reaction and the solution was dialyzed against dH_2O (Spectra/Por 1 kDa molecular weight cut-off [MWCO]) for 24 h. The retentate was filtered (0.2 µm, polyethersulfone [PES]) and lyophilized to yield a white powder (511 mg, 0.0485 mmol, 92.6% yield). ^{1}H NMR (500 MHz, $CDCl_3$) δ 10.1 (s, 2H) 8.14 – 7.74 (m, 12H), 3.84 – 3.76 (m, 6H), 3.65 (d, J = 21.2 Hz, 1020H [PEG backbone]), 3.56 (t, J = 4.7 Hz, 8H), 3.54 – 3.51 (m, 5H), 3.44 (s, 8H). Based on the relative integrations of protons corresponding to the 4-arm PEG core (δ 3.44) and benzaldehyde (δ 8.14-7.74), end-group functionalization was estimated to be ~80%. ^{1}H NMR of benzaldehyde-functionalized 4-arm PEG is given in Figure A1.

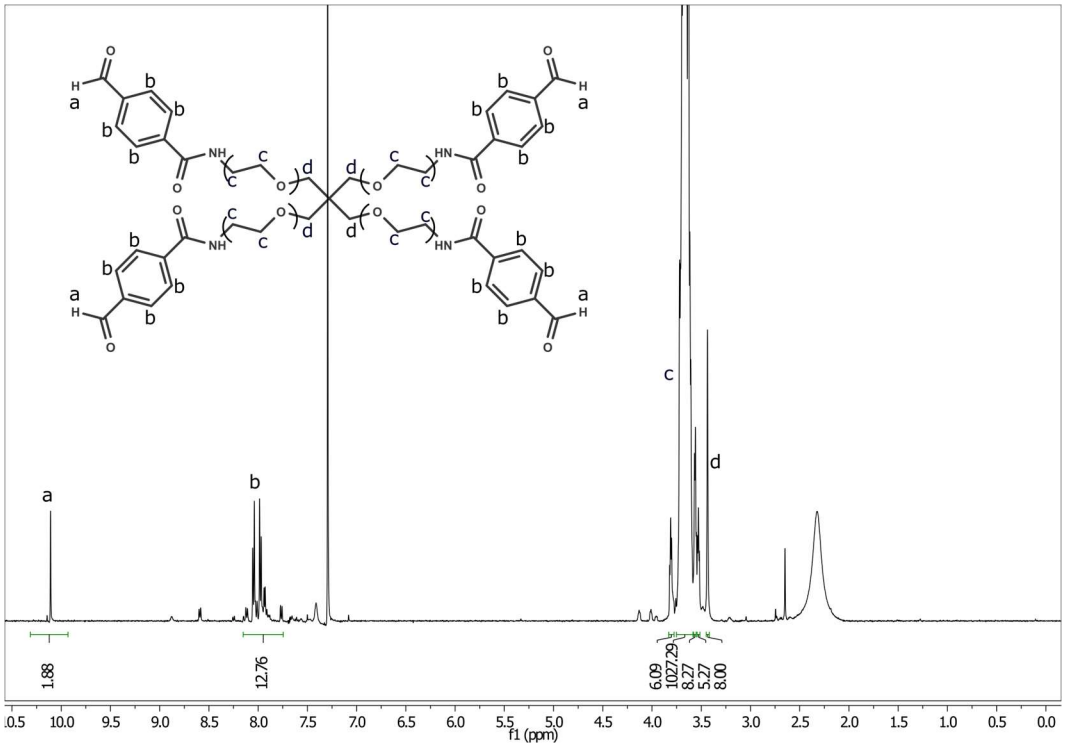

Figure A1. ^{1}H NMR of benzaldehyde-functionalized 4-arm PEG ($CDCl_3$, 500 MHz).

Synthesis of Alkoxyamine-functionalized 4-arm PEG.

2,5-dioxopyrrolidin-1-yl 2-{[(tert-butoxycarbonyl)amino]oxy}acetate was synthesized as described previously[179].

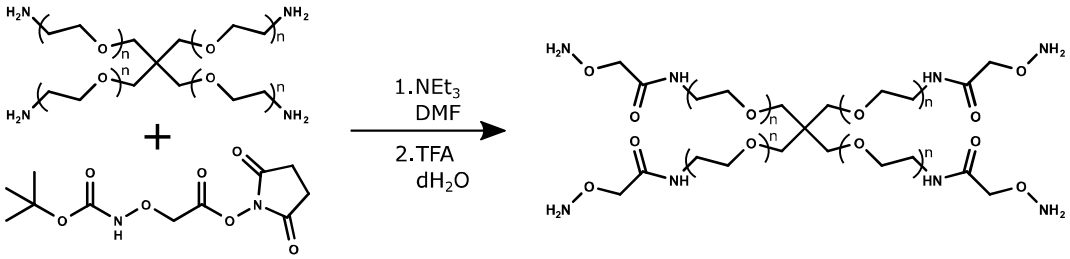

4-arm PEG-amine (110 mg, 0.0110 mmol, Mn ~ 10 kDa) and 2,5-dioxopyrrolidin-1-yl 2-{[(tert-butoxycarbonyl)amino]oxy}acetate (25.4 mg, 0.0882 mmol) were added to a round-bottom flask under Ar. The reactants were dissolved in anhydrous DMF (1.10 mL), NEt_3 (24.5 μL, 0.176 mmol) was added, and the reaction was stirred overnight at room temperature. The reaction was precipitated with diethyl ether (Et_2O, 20 mL), centrifuged, decanted, and re-dissolved in trifluoroacetic acid in dH_2O (5 v/v %, 2 mL). The solution was stirred for 3 h at room temperature. The solution was precipitated with Et_2O (20 mL), centrifuged, decanted, and re-dissolved in dH_2O (9 mL). The solution was dialyzed against dH_2O (Spectra/Por 1 kDa MWCO) for 24 h. The retentate was filtered (0.2 μm, PES) and lyophilized to yield a white powder (59.1 mg, 0.0591 mmol, 53.7% yield). ^{1}H NMR (500 MHz, $CDCl_3$) δ 4.57 (s, 1H), 4.53 (s, 1H), 4.36 (s, 1H), 4.26 (s, 1H), 4.21 (s, 1H), 3.99 (s, 2H), 3.60 – 3.55 (m, 6H), 3.44 (s, 1020H [PEG backbone]), 3.34 – 3.31 (m, 14H), 3.31 – 3.28 (m, 9H), 3.21 (s, 8H). Based on the relative integrations of protons corresponding to the 4-arm PEG core (δ 3.44) and the alkoxyamine α-methylene (δ 4.57-3.99), end-group functionalization was estimated to be ~80%. ^{1}H NMR of alkoxyamine-functionalized 4-arm PEG is given in Figure A2.

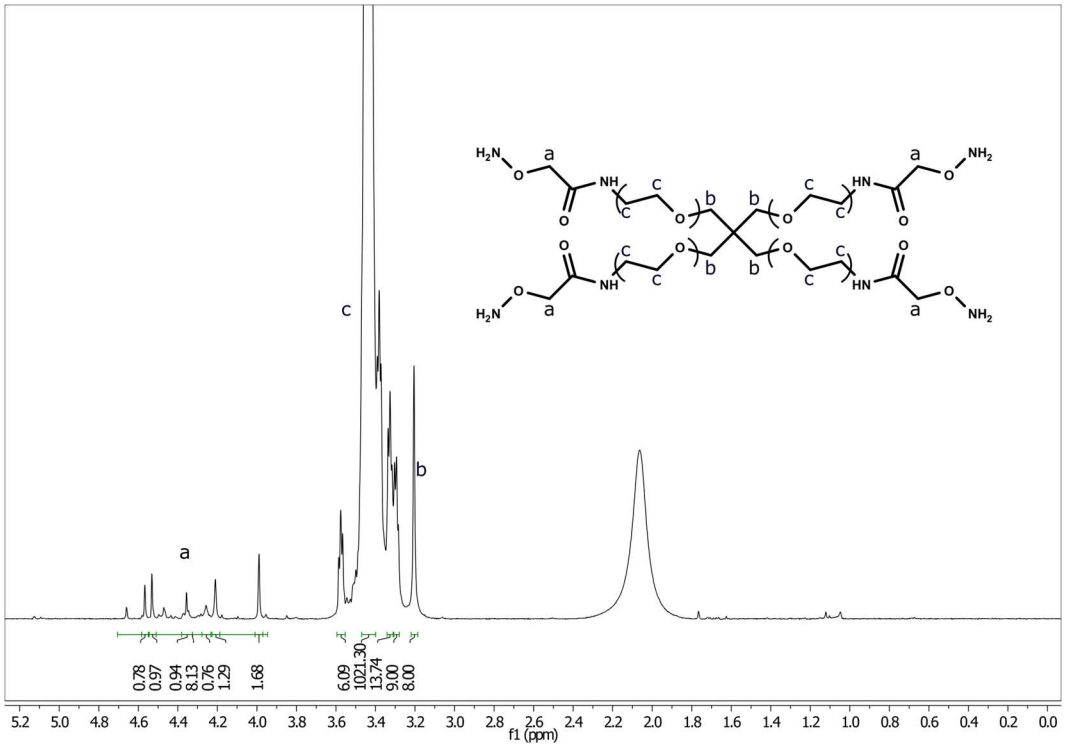

Figure A2. Figure S7. ^{1}H NMR of alkoxyamine-functionalized 4-arm PEG ($CDCl_3$, 500 MHz).

Determination of NPPOC-Aha Photo-uncaging Kinetics

To determine the kinetics of NPPOC-Aha uncaging upon UV light exposure, NPPOC-Aha (3.4 mM dissolved in 50:50 dH_2O:CH_3CN) was placed in quartz NMR tubes and irradiated with collimated UV light (365 nm, 10 mW cm^{-2}) emanating from an OmniCure (series 1500; light intensity measured with Cole-Palmer series 9811 radiometer). Time points were collected every 120 s for a total of 600 s. The resulting degradation products were separated by reverse-phase HPLC, eluting with a CH_3CN/dH_2O gradient ramping from 5% to 100% CH_3CN over 55 minutes. Remaining NPPOC-Aha was identified by HRMS (ESI+). Calculated for $C_{14}H_{18}N_5O_6$

[M + 1H]+, 352.1257; observed 352.1259 (Δ = 0.5 ppm). The HPLC peak corresponding to starting material was integrated and monitored over time.

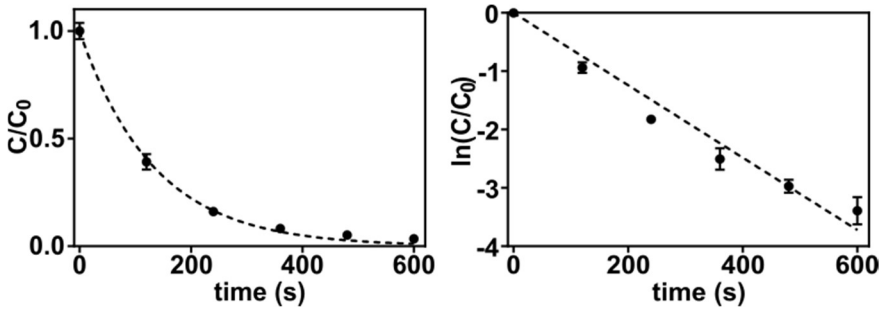

Figure A3. Uncaging kinetics of NPPOC-Aha. Kinetic analysis of NPPOC-Aha photolysis demonstrates rapid uncaging suitable for biological sampling.

Cell Culture, Metabolic Labeling, and Analysis of Aha Incorporation

For *in vitro* work, borosilicate well plates (Mattek, P35G-1.5-14-C) were pretreated with high glucose Dulbecco's Modified Eagle Media (DMEM) supplemented with fetal bovine serum (FBS, 10%) and penicillin-streptomycin (PS, 1%). Plates were incubated at 37 °C for 10 minutes. HeLa cells were cultured on tissue culture polystyrene before seeding on borosilicate glass. After cells reached the desired confluency (50-60% for imaging; 80-90% for lysate analysis), cells were subjected to the following experiments.

Cells were rinsed with warm 1x Dulbecco's phosphate buffered saline (DPBS) and starved of methionine (Met) by the addition of Met-depleted media (1 h, 37 °C). Met-depleted media was prepared by adding L-cystine-2HCl (0.2 mM), L-glutamine (4 mM), and sodium pyruvate (1 mM) to depleted media (Fisher, 21013024). Media was removed and cells were treated with media containing NPPOC-Aha at the desired concentration (0-250 μM). Control

media consisted of Aha or Met in the place of NPPOC-Aha. Cells were then irradiated with light (365 nm, 1-10 mW cm^{-2}, 5 min). The cultures were then incubated (2 h, 37 °C) to promote Aha incorporation. The cells were then washed with 1xDPBS (37 °C).

Samples were prepared for sodium dodecyl sulfate polyacrylamide gel electrophoresis (SDS-PAGE) by lysing cells in lysis buffer (10 mM PO_4, pH 7.0, 0.5% sodium dodecyl sulfate). Proteins were collected and immediately placed on ice. Free thiols were capped by the addition of iodoacetamide (10 mM, 30 min, room temperature). Azide-containing proteins were labeled by treatment with FAM-BCN (10 μM, 5 hours, room temperature). Excess FAM-BCN was removed by precipitating proteins with 4x sample volume of cold acetone (-20 °C). Lysates were incubated in acetone (1 h, -20 °C) and then subjected to centrifugation (14,000xg, 10 min). Proteins were redissolved in lysis buffer with gentle heating (40 °C, 10 min), precipitated once more, and washed with 4x sample volume acetone before drying (20 min). Proteins were then dissolved in SDS-PAGE sample buffer (50 mM Tris-HCl, 2% SDS, 10% glycerol, 12.5% β-mercaptoethanol, 0.025% bromophenol blue). Proteins were electrophoretically separated by a 12% polyacrylamide gel by applying a potential of 105 V. After electrophoresis, gels were scanned on a Typhoon FLA9000 fluorescent gel scanner before being stained with coomassie dye.

Assessing NPPOC-Aha *In Vitro* Stability

The stability of NPPOC-Aha was conducted using the above protocols for cell culture and SDS-PAGE with minor modifications. Instead of irradiating samples immediately following addition

of NPPOC-Aha media, NPPOC-Aha was incubated in the presence of cells for the desired time (0-4 hours) prior to light exposure. Met (3.33 μM) was added to all media, yielding a 30:1 ratio of NPPOC-Aha:Met[72].

Fluorescent Labeling of Activated Cellular Protein

To fluorescently label Aha-tagged proteins for visualization, cells were rinsed with warm 1xDPBS (37 °C) before fixing with formaldehyde (4%, 10 min, room temperature). Fixed cells were rinsed with 1xDPBS, and permeabilized with Triton™ X-100 (Sigma, 0.5%, 2 min, room temperature). Cells were then washed (3x, 5 min each) with 1xDPBS. Azides were labeled by strain-promoted azide-alkyne cycloaddition (SPAAC) with FAM-BCN (100 nM, 30 min, room temperature) in the dark. Next, labeled cells were washed (3x, 5 min each) with 1xDPBS prior to imaging on a Leica SP8X laser scanning confocal microscope.

Spatial Labeling of Activated Cellular Protein in 3D Tissue Culture

HeLa cells were liberated from the tissue culture plate with trypsin, resuspended in FBS-supplemented DMEM, and pelleted by centrifugation. The cells were then gently resuspended in depleted media containing the photocaged Aha. Hydrogel precursors (10k PEG functionalized with alkoxyamines or benzaldehyde) were combined (1:1 benzaldehyde:alkoxyamine stoichiometry) with cells prior to deposition on a glass-bottomed well plate (7 wt%, 10 mM aniline, 5 million cells/mL). After the gel had formed (30 min), it was inundated with depleted media containing Aha (100 μM, 30 min). Excess media was removed by aspiration and a

subsection of the gel was irradiated with light (365 nm, 10 mW cm^{-2}, 5 min) through a slitted photomask. Gels were washed with warm 1xDPBS (37 °C, 15 min) before fixing with formaldehyde (4%, 1 hr, room temperature). Fixed cells were rinsed with 1xDPBS, and permeabilized with Triton™ X-100 (Sigma, 0.5%, 1 hr, room temperature). Cells were then washed (3x, 1 hr each) with 1xDPBS. Azides were labeled by SPAAC with FAM-BCN (100 nM, 6 hrs, room temperature) in the dark. Next, cells were labeled with Alexa Fluor 594 phalloidin (5 units/mL, Thermo Fisher), and Hoechst 33342 (5 µg/mL; 1 hr, room temperature, Thermo Fisher) to act as a counterstain by labeling actin and DNA, respectively. The gels were then washed (3x, 1 hr each) with 1xDPBS prior to imaging on a Leica SP8X laser scanning confocal microscope. Intensity analysis was conducted using the Fiji image processing package. Gels were stored overnight in PBS at 4 °C. Experimental results are provided in Figure A4.

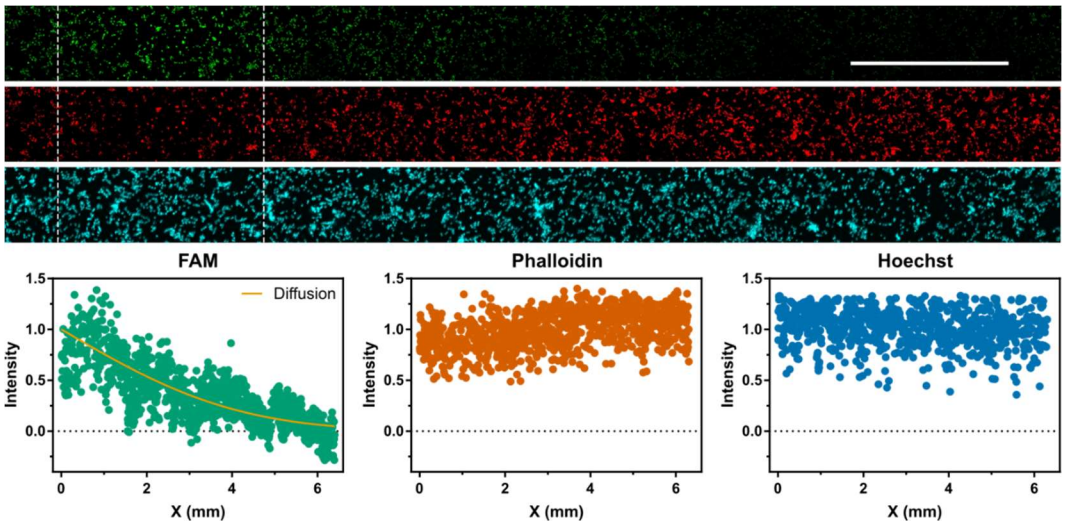

Figure A4. Spatially labeled 3D tissue culture (top, carboxyfluorescein) and counter stains (middle, phalloidin; bottom, Hoechst; scale bar - 1 mm). An intensity profile of carboxyfluorescein staining over the length of the sample

provides the expected patterned response. The result correlated well with the solution to the anticipated diffusion in the system (r^2=0.60). Counterstains consisting of phalloidin (actin) and Hoechst (DNA) demonstrate no substantial patterning.

The approximate diffusion profile was obtained by solving the second-order partial differential equation (A1).

$$\frac{\partial C}{\partial t} = D\left[\frac{\partial^2 C}{\partial x^2}\right] + R \tag{A1}$$

Boundary Conditions

$$C(x \to \infty) = 0$$

$$C(x \to -\infty) = 1$$

Initial Condition

$$C(t = 0) = \begin{cases} 1; x \leq 0 \\ 0; x > 0 \end{cases}$$

Where C is the concentration at time t(s) and position x(m), D(m^2s^{-1}) is the diffusion constant, and R is the consumption rate. The consumption rate was assumed to be negligible, and the diffusion constant of L-isoleucine[180] ($7.32x10^{-10}$ m^2s^{-1}) in aqueous solution was used to approximate the diffusion constant of Aha. The solution to the differential equation assuming infinite sink and infinite source boundary conditions, and the step function initial condition provides equation (A2).

$$C(x,t) = \frac{1}{2} + \frac{1}{2} Erf\left(\frac{x}{\sqrt{4Dt}}\right) \tag{A2}$$

With the origin set to the edge of the photomask, the normalized experimental data was compared to the normalized diffusion profile for t = 2 h and is shown in Figure A4.

Affinity Purification of Activated Cellular Proteins

Aha-tagged proteins were purified through affinity-based enrichment using a modified version of a published protocol.[72] Cells were lysed in 0.5% SDS in 20 mM disodium phosphate. Clarified lysate (500 µL, 0.5 mg/mL total protein content) was heated (90 °C, 10 min) prior to reduction (10 mM dithiothreitol, 25 min, 56 °C) and thiol alkylation (iodoacetamide, 14 mM). DNA was digested with Benzonase® (Thermo Scientific) and cleared by centrifugation. Proteins were biotinylated *via* SPAAC with DBCO-biotin probe (26 µM, Click Chemistry Tools, overnight, 20 °C). Tagged proteins were captured with Streptavidin UltraLink™ Resin (Thermo Scientific), washed with SDS (0.2 mL, 1% in PBS, 6x) followed by urea washing (8 M) and cleavage from resin (70 °C, 5 min, 10 mM biotin, 7.5 M guanidine HCl, pH = 1.5). Eluent buffer was exchanged to 8 M urea, pH = 8, and concentrated on a 30 kDa cut-off centrifugation filter (Millipore). Proteins were separated using 10% polyacrylamide gels and visualized by silver stain. Experimental results are given in Figure A5.

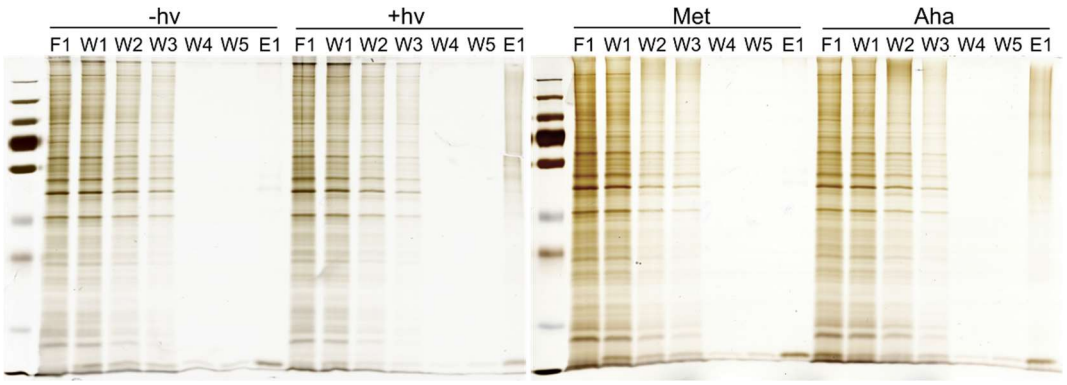

Figure A5. Isolation of proteins by laBONCAT. Following photomediated Aha incorporation, newly synthesized proteins are isolated by affinity purification for

downstream proteomic analysis. From left to right: flow through fraction 1 (F1), wash fractions 1-5 (W1-5), and elution fraction 1 (E1).

Synthesis of **[(1R,8S,9S)-bicyclo[6.1.0]non-4-yn-9-yl]methyl 2,5-dioxopyrrolidin-1-yl carbonate (VII),** a bicyclononyne NHS activated ester (BCN-NHS). This product has been synthesized previously by our group[94].

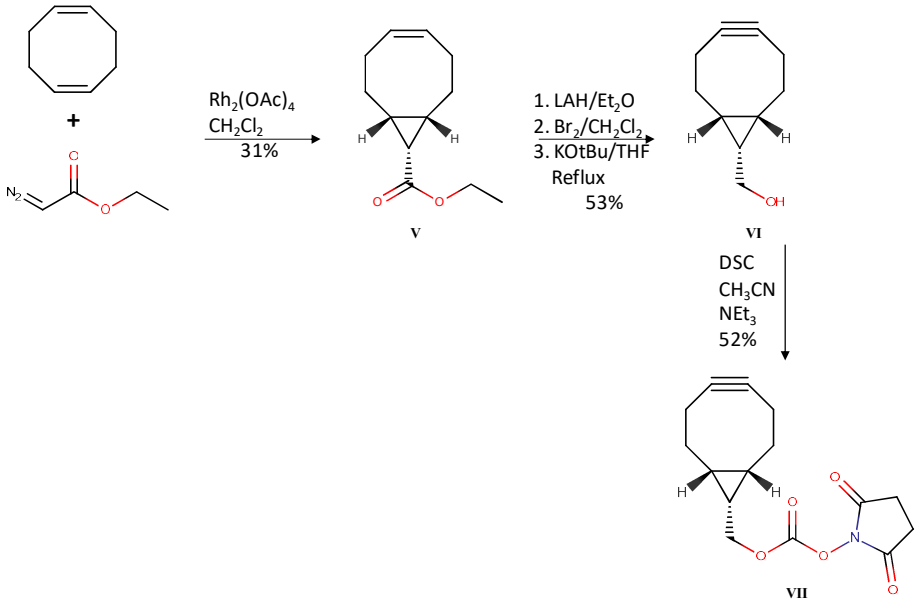

Scheme A2. Synthesis of BCN-NHS.

Synthesis of ethyl (1R,4Z,8S,9S)-bicyclo[6.1.0]non-4-ene-9-carboxylate (V).

All glassware was flame-dried and purged with N_2 before use. 50 mL (407 mmol) of commercially available cyclooctadiene, 1 g Rh(II) acetate dimer catalyst, and 30 mL CH_2Cl_2 were added to a dried reaction flask. The reaction was brought to 0 °C. 7 mL (62 mmol) ethyl

diazoacetate in 35 mL CH_2Cl_2 was added to the reaction flask dropwise over an hour, using an addition funnel. The reaction was brought to room temperature and stirred over 72 hours. The solution was filtered to remove the catalyst and the solution was concentrated. Excess cyclooctadiene is removed using a high vacuum. The product was purified by flash column chromatography using a gradient from 0 to 1% EtOAc in hexane. 3.7 g of the endo stereoisomer was obtained; 31% yield. Another 5.62 g of the exo product was also obtained. ^{1}H NMR (500 MHz, $CDCl_3$): δ 5.64 (2H, cm), 4.14 (2H, q, J=7.1 Hz), 2.53 (2H, cm), 2.23 (2H, cm), 2.08 (2H, cm), 1.86 (2H, cm), 1.73 (1H, t, J=8.8 Hz), 1.42 (2H, cm), 1.29 (3H, t, J=7.1 Hz).

Synthesis of [(1R,8S,9S)-bicyclo[6.1.0]non-4-yn-9-yl]methanol (VI).

3.7 g (19 mmol) of **V** was dissolved in 65 mL anhydrous ether. 750 mg (19.8 mmol) LAH was added to a flame dried flask and dissolved in anhydrous ether. Both solutions were brought to 0 °C and stirred. The LAH solution was added to the ester dropwise over 15 minutes. The reaction was stirred at room temperature for 20 minutes. A minimal amount of water was added to quench the solution. Hydrogen was observed evolving and light grey clumps formed as the solution cleared. The solution was dried with $MgSO_4$, filtered, and the solvent removed under high vacuum. 2.91 g crude product obtained; quantitative crude yield. This intermediate was dissolved in CH_2Cl_2, and brought to 0 °C. 1 mL Br_2 was dissolved in 13 mL CH_2Cl_2 and added dropwise until a yellow color persisted. The reaction was quenched with 50 mL 10% $Na_2S_2O_2$ in DI H_2O and the solution cleared upon mixing. The product was extracted with 2x70 mL CH_2Cl_2, dried with $MgSO_4$, and concentrated under vacuum. 5.8 g of crude product obtained; quantitative crude yield. This intermediate is then dissolved in 120 mL anhydrous THF and brought to 0 °C.

52 mL 1 M KOtBu in THF was added dropwise and the solution was brought to 75 °C. The reaction was stirred at reflux for 2.5 hours. After bringing the solution to room temperature, the solution was quenched with 150 mL saturated NH_4Cl. The THF was removed under vacuum and remaining aqueous layer was extracted with 3x70 mL CH_2Cl_2. The solution was dried with $MgSO_4$, filtered, and concentrated under vacuum. The product was purified using a gradient from 0-20% EtOAc in hexane. 1.48 g of a yellow oil was obtained; 53% yield over 3 steps. ^{1}H NMR (500 MHz, $CDCl_3$): δ 3.62 (2H, d, J=7.7 Hz), 2.59 (1H, brs), 2.16 (6H, cm), 1.50 (2H, cm), 1.22 (1H, cm), 0.84 (1H, cm).

Synthesis of [(1R,8S,9S)-bicyclo[6.1.0]non-4-yn-9-yl]methyl 2,5-dioxopyrrolidin-1-yl carbonate (VII)

1.48 g (9.9 mmol) of **VI** and 5.1 g (19.9 mmol) disuccinimidyl carbonate (DSC) were combined in a reaction flask and placed under N_2. The compounds were dissolved in 75 mL CH_3CN and 4.5 mL (32 mmol) NEt_3 was added and the reaction was stirred overnight at room temperature. The reaction was diluted with 200 mL EtOAc:ether 1:1 and washed with 6x100 mL DI H_2O and 2x50 mL brine. The organic layer was dried with $MgSO_4$, filtered, and concentrated under vacuum. The residue was purified by flash column chromatography eluting with 3:1 hexane:EtOAc. 1.72 g of a white solid obtained; 52% yield. ^{1}H NMR (500 MHz, $CDCl_3$): δ 4.48 (2H, d, J=8.4 Hz), 2.87 (4H, s), 2.30 (6H, cm), 1.57 (3H, cm), 1.09 (2H, cm).

Synthesis of 2-(2-nitrophenyl)propyl N-({[2-(2-{2-[({[(1R,8S)-bicyclo[6.1.0]non-4-yn-9-yl]methoxy}carbonyl)amino]ethoxy}ethoxy)ethyl]carbamoyl}methoxy)carbamate (IX), a photocaged hydroxylamine bicyclononyne (NPPOC-NHO-BCN).

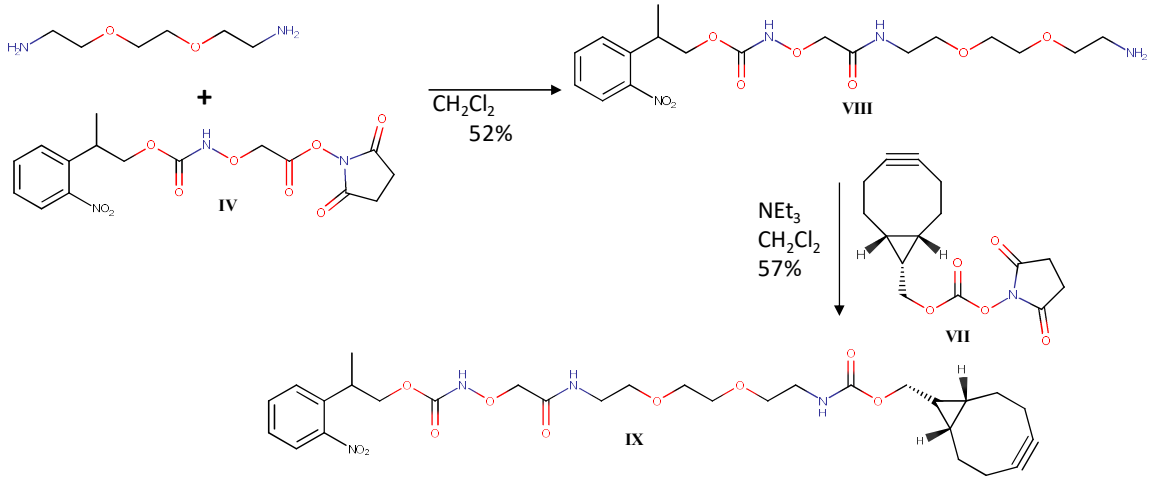

Scheme A3. Synthesis of the heterobifunctional probe (NPPOC-NO-BCN).

Synthesis of 2-(2-nitrophenyl)propyl N-[({2-[2-(2-aminoethoxy)ethoxy]ethyl}carbamoyl)methoxy] carbamate (VIII).

250 mg (0.63 mmol) IV was dissolved in 25 mL anhydrous CH_2Cl_2. 0.5 mL (3.4 mmol) of commercially available 1,8-diamino-3,6-dioxaoctane was added and the reaction was left stirring at room temperature overnight. The solvent was removed under reduced pressure and the residue was purified by flash column chromatography, eluting with 5:2:0.1 CH_2Cl_2:EtOH:NH_4OH. 140 mg obtained; 52% yield. ^1H NMR (500 MHz, D_2O): δ 7.64 (1H, cm), 7.53 (1H, cm), 7.49 (1H, cm), 7.31 (1H, t, J=7.8 Hz), 4.14 (4H, cm), 3.54 (13H, cm), 2.92 (2H, s), 1.18 (3H, d, J=7.0 Hz).

HRMS (ESI+) Calculated for $C_{18}H_{29}N_4O_8$ [M+H]+, 429.1985; observed: 429.1993 (Δ = 1.86 ppm).

Synthesis of 2-(2-nitrophenyl)propyl N-({[2-(2-{2-[({[(1R,8S)-bicyclo[6.1.0]non-4-yn-9-yl]methoxy}carbonyl)amino]ethoxy}ethoxy)ethyl]carbamoyl}methoxy)carbamate (IX).

140 mg (0.33 mmol) **VIII** and 120 mg (0.41 mmol) **VII** were combined and dissolved in 15 mL anhydrous CH_2Cl_2. 0.25 mL (1.8 mmol) NEt_3 was added *via* syringe. The reaction was stirred overnight at room temperature. 0.25 mL DI H_2O was added to quench any remaining NHS carbonate and the solution was stirred for 30 minutes at room temperature. The solution was washed with 20 mL DI H_2O followed by 20 mL $NaHCO_3$. The organic layer was then dried with $MgSO_4$, filtered, and the solvent was removed under reduced pressure. The residue was purified by flash column chromatography, eluting with 2% MeOH in CH_2Cl_2. 60 mg obtained; 52% yield. ^{1}H NMR (500 MHz, $CDCl_3$): δ 7.68 (1H, dd, J=8.2 Hz), 7.51 (1H, t, J=7.7 Hz), 7.39 (1H, d, J=7.9 Hz), 7.32 (1H, t, J=7.7 Hz), 4.23 (3H, cm), 4.07 (2H, d, J=7.7 Hz), 3.65 (1H, m, J=6.9 Hz), 3.54 (4H, brs), 3.49 (4H, cm), 3.43 (2H, q, J=5.3 Hz), 3.28 (2H, t, J=5.0 Hz), 2.18 (5H, cm), 1.98 (1H, br s), 1.50 (2H, cm), 1.29 (3H, d, J=7.0 Hz), 1.21 (2H, cm), 0.84 (3H, cm). HRMS (ESI+) Calculated for $C_{18}H_{29}N_4O_8$ [M+H]+, 605.2823; observed: 605.2828 (Δ = 0.82 ppm)

Synthesis of **L-azidohomoalanine** (XIV), a non-canonical amino acid and methionine surrogate that has been synthesized previously[93].

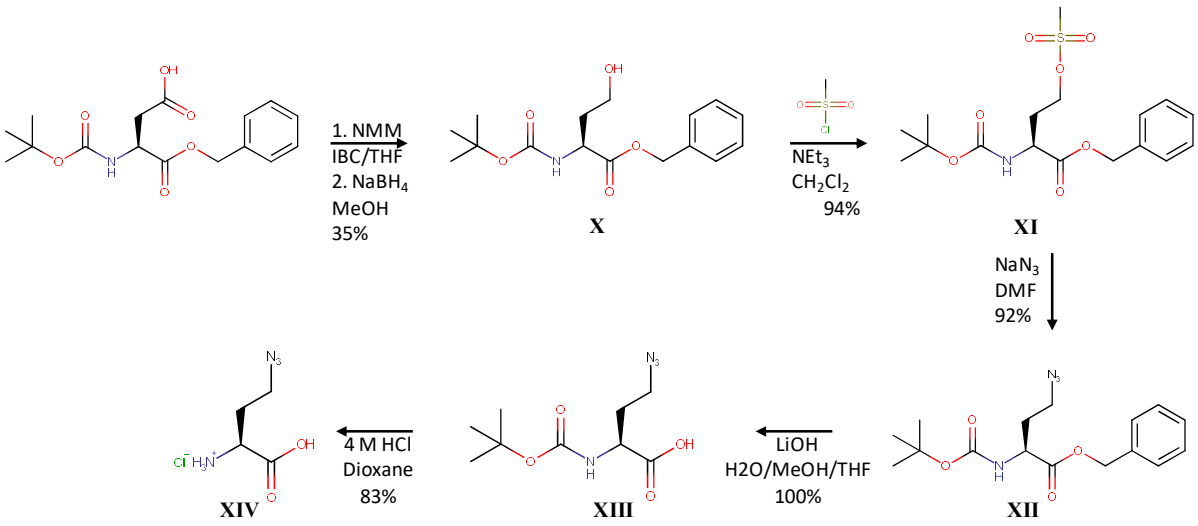

Scheme A4. Synthesis of L-azidohomoalanine.

Synthesis of benzyl (2S)-2-{[(tert-butoxy)carbonyl]amino}-4-hydroxybutanoate (X).

5 g (15.5 mmol) of commercially available N-Boc-O-Bn-L-aspartic acid was dissolved in 60 mL anhydrous THF and placed under an atmosphere of N_2. The solution was brought to -10C° using an ethylene glycol cold bath. 1.7 mL (15.5 mmol) *N*-methyl morpholine was added *via* syringe. Over 15 minutes 2 mL (15.3 mmol) isobutyl chloroformate was added *via* syringe and the solution was stirred for an additional 10 minutes. 3.5 g (92.5 mmol) $NaBH_4$ was added to the reaction. 150 mL MeOH was added over 45 minutes using an addition funnel and the reaction was stirred for another 20 minutes. A large amount of gas is evolved during the first few minutes of addition. Next, 40 mL 1 M HCl was added using an addition funnel. The organic solvent is then removed under reduced pressure. The remaining aqueous phase was extracted with 3x120 mL EtOAc. The organic layers were combined and washed with 100 mL 1 M HCl, 2x100 mL DI

H_2O, 100 mL saturated $NaHCO_3$, and 2x100 mL brine. The organic layer was then dried with $MgSO_4$, filtered, and the solvent was removed under reduced pressure. The residue was then purified by flash column chromatography, eluting with 1% MeOH in CH_2Cl_2. 1.76 g obtained; 35% yield.

Synthesis of benzyl (2S)-2-{[(tert-butoxy)carbonyl]amino}-4-(methanesulfonyloxy) butanoate (XI).

1.76 g (5.7 mmol) of **X** was dissolved in 30 mL anhydrous CH_2Cl_2 and 1.6 mL (11.5 mmol) anhydrous NEt_3 was added *via* syringe. The solution was then brought to 0 °C using an ice bath. 0.5 mL (6.5 mmol) MsCl was added. The reaction was brought back to room temperature and stirred for 1.5 hours. The reaction was quenched with 20 mL saturated NH_4Cl and the organic layer was then washed with 2x20 mL brine. The aqueous layers were then combined and back extracted with 2x70 mL CH_2Cl_2. The organic layers were then combined, dried with $MgSO_4$, filtered, and concentrated under reduced pressure. The residue was purified by flash column chromatography, eluting with 1% MeOH in CH_2Cl_2. 2.1 g obtained; 94% yield.

Synthesis of benzyl (2S)-4-azido-2-{[(tert-butoxy)carbonyl]amino}butanoate (XII).

2.01 g (5.2 mmol) **XI** was dissolved in 20 mL DMF and placed under a N_2 atmosphere. 0.5 g (7.7 mmol) NaN_3 was added and the solution was heated to 40 °C. The reaction was stirred for 4 hours at 40 °C. The solvent was removed under reduced pressure and the residue purified by

flash column chromatography, eluting with 4:1 petroleum ether:EtOAc. 1.6 g obtained; 92% yield.

Synthesis of (2S)-4-azido-2-{[(tert-butoxy)carbonyl]amino}butanoic acid (XIII).

0.8 g (2.4 mmol) of **XII** was dissolved in 30 mL 50:50 THF:MeOH and 15 mL 3 M aqueous LiOH was added. The reaction was stirred for 4 hours at room temperature. The organic solvents were removed under reduced pressure. 25 mL DI H_2O was added, and the solution titrated to pH 7 with $KHSO_4$. The solution was extracted with 2x15 mL CH_2Cl_2 and the organic layers were discarded. Next the solution was titrated to pH 2 with $KHSO_4$ and the solution was extracted with 5x20 mL CH_2Cl_2. The organic layers were combined, dried with $MgSO_4$, filtered, and concentrated under reduced pressure. The product was used without further purification. 0.58 g obtained; quantitative yield.

Synthesis of L-azidohomoalanine (XIV).

500 mg (2.2 mmol) **XIII** was dissolved in 9 mL 4 M HCl in dioxane and the solution was stirred vigorously for 4 hours. The solvent was then removed under reduced pressure and the residue was suspended in cold (-20 °C) acetone. White crystals are visible, and these are collected using a fritted funnel. After washing thoroughly with cold acetone, the crystals are dissolved in D H_2O and the solution is collected. The product is then dried under reduced pressure. 300 mg obtained; 83% yield. HRMS (ESI+) Calculated for $C_{18}H_{29}N_4O_8$ [M+H]+, 145.0726; observed: 145.0726

(Δ = 0 ppm). ^{1}H NMR (500 MHz, D_2O): δ 3.99 (1H, t, J=6.3 Hz), 3.54 (2H, t, J=6.5 Hz), 2.12 (2H, cm).

Synthesis of Benzaldehyde-Functionalized Resin

The storage solution for a crosslinked agarose resin bearing an amine functional group (250 μL resin, 60 mM -NH_2) was removed by centrifugation and replaced with DI H_2O. 4-formyl benzoic acid (18.5 mg, 0.075 mmol, 8 eq) and EDAC (2.4 mg, 1 eq) were dissolved (20 mM NaOH), added to the resin, and the mixture was stirred (1 hr, RT). Excess reagents were removed by dilution with water, centrifugation and decanting (5x). The extent of functionalization was determined to be 95% by quantitative ninhydrin test. Add 1x sample volume to 2x ninhydrin solution (1 M NaOAc, 110 mM ninhydrin, 75% DMSO, 10 min, 95 °C) and quantify against a standard curve of unfunctionalized resin.

Photopatterning of NPPOC-NHO-BCN on a glass slide

An azide-functionalized glass slide[181] was treated with a droplet of 50 mM of **IX** in DMSO for 1 hour. The slide was then rinsed with thoroughly with DI H_2O. Next, the slide was protected with a photomask (400 μm chrome lines on a glass substrate spaced 400 μm apart) and irradiated with cytocompatible UV light (365 nm, 10 mW cm^{-2}, 10 min). Next, the slide was treated with a droplet of 1 mM **FAM-aldehyde** in PBS for 1 hour. The slide was then rinsed thoroughly with DI H_2O and the slide was imaged with a fluorescent microscope at λ=475 nm.

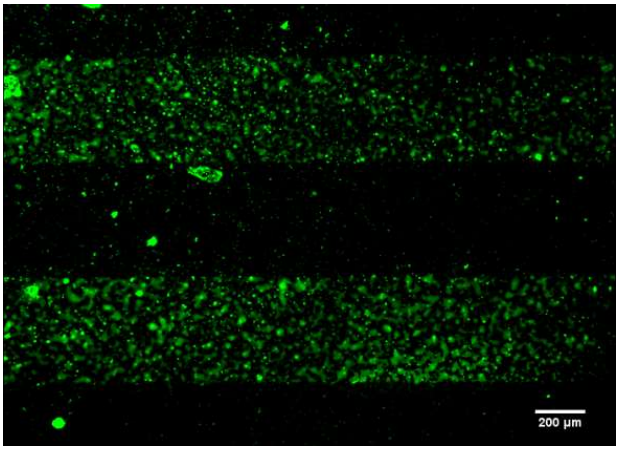

Figure A6. Photopatterning on a glass slide. An azide-functionalized glass slide was treated with NPPOC-NHO-BCN, and the probe was photoactivated (λ=365 nm) through a slitted photomask with features of parallel lines 400 µm wide separated by gaps of 400 µm. The slide was treated with FAM-BA to fluorescently label the activation. The spatial resolution achieved appears consistent with the expected activation.

Lysate treatments for SDS-PAGE Gels

Mouse fibroblast 3T3 cells were cultured in FBS supplemented DMEM media. At roughly 60% confluence cells were subjected to a media swap. Briefly, cells were gently rinsed with warm 1xPBS solution, and subjected to methionine starvation by incubating cells for 1 hour in methionine depleted media. Media was then aspirated and replaced with methionine free Aha doped media (containing no FBS). Cells were incubated in Aha media for 4 hours. Control cells were starved then given methionine doped media instead of Aha. No morphological changes were observed throughout starvation and Aha replacement. Next, media is aspirated and cells are lysed with 10 mM Na_3PO_4, 5% SDS solution at 0 °C for 10 minutes. No cells were visible after

lysis. Lysates were collected using a cell scrapper and micropipette. Lysates were denatured at 100 °C for 5 minutes. A bicinchoninic acid assay (BCA) was conducted in accordance with the manufacturer's protocol to determine protein concentrations in lysate. Typical lysate concentrations were 0.2-0.4 mg/mL. From here lysates were split into subvolumes for treatment experiments and kept in the dark whenever possible. There are 4 treatments (Aha, NPPOC-NHO-BCN, light, FAM-aldehyde) for a total combination of 16 unique treatment conditions. Next, lysates were treated to a final concentration of 100 μM NPPOC-NHO-BCN (or an equal volume 1xPBS for the control) and the copper-free click reaction was allowed to proceed for 1 hour. Lysates were then irradiated with 365 nm light at 10 mW cm^{-2} for 5 minutes or kept in the dark for the control. Next the samples were treated to a final concentration of 10 μM FAM-aldehyde (or an equal volume 1xPBS for the control), 100 mM final concentration of aniline[182,183] was added to each sample and the oxime ligation was allowed to progress for 20 hours. Proteins were precipitated using acetone to remove excess FAM-aldehyde, NPPOC-NHO-BCN, and aniline. Briefly, 4xlysate volumes of acetone at -20 °C was added to each sample and samples were incubated at -20 °C for 1 hour. Proteins were pelleted by centrifugation at 14,000xg for 10 minutes and the supernatant was removed by micropipette. Samples were rinsed with another volume of acetone, incubated, centrifuged, and the supernatant was removed. Then proteins were resuspended in lysis buffer and subjected to another round of precipitation as described. Pellets were then resuspended in SDS buffer (50 mM Tris-Cl, 2% sodium dodecyl sulfate, 0.1% bromophenyl blue, 10% glycerol). Around 5 μg total protein was loaded into each well of a polyacrylamide and the gel was developed. Fluorescence images were generated on a GE Typhoon FLA 9000 with an excitation wavelength of 473 nm and a filter at 500 nm. The gel

was then immersed in a coomassie stain solution (0.1% coomassie brilliant blue, 50% ethanol, 40% DI H_2O, 10% AcOH), and imaged on an Epson scanner.

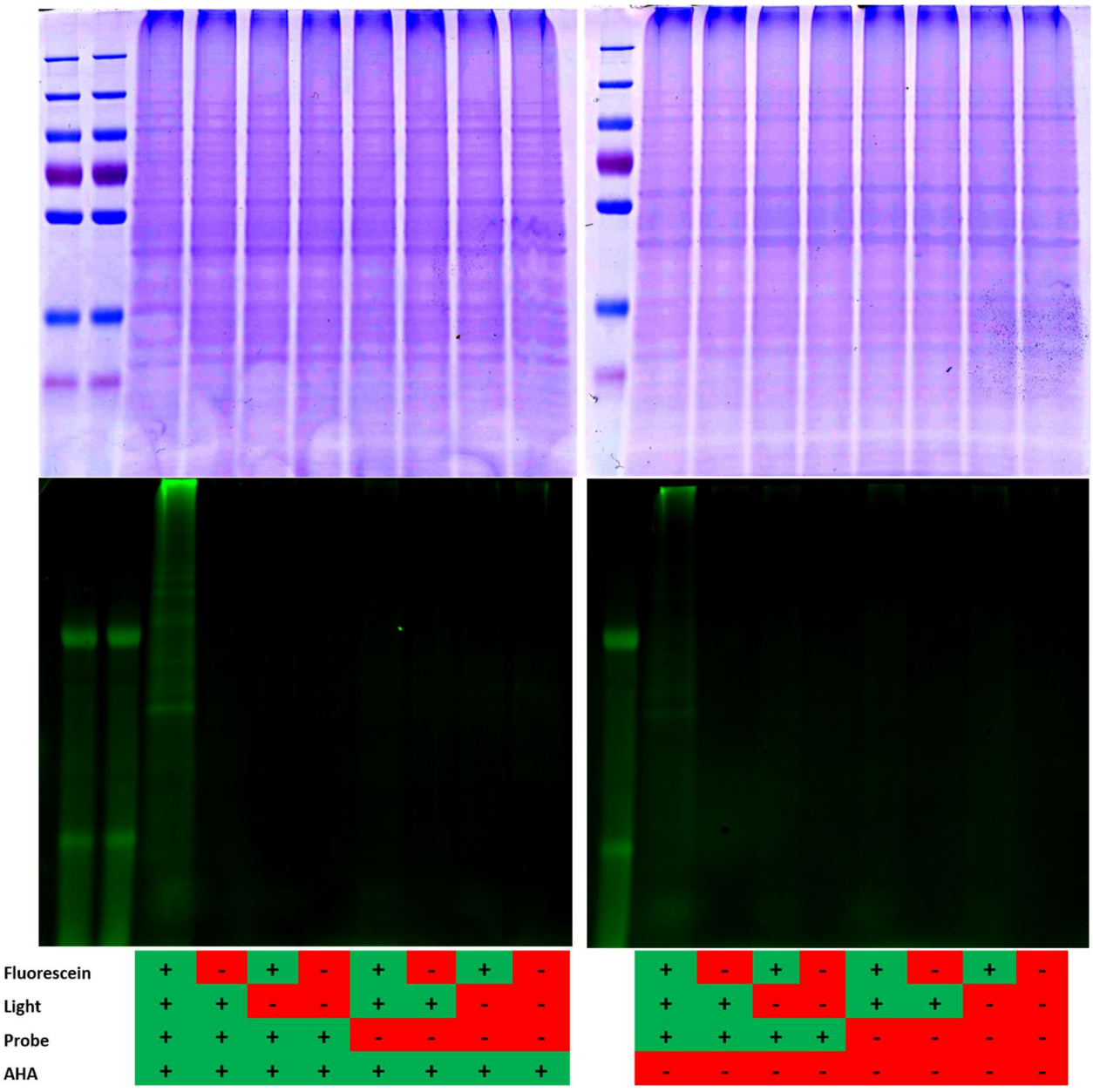

Figure A7. Activation and fluorescent labeling of proteins by PAINT.

Labeling and Photoactivation of Tissue Culture

To facilitate light irradiation of tissue culture, HeLa cells were grown on 1.5 μm borosilicate glass bottom dishes (Cellvis, D35-20-1.5-N). Cells were grown to the desired confluency (50-100% for imaging; 100% for quantification). Media was aspirated from the cell culture and it was washed (1xPBS; 37 °C). Cells were then starved of methionine, by incubating with unsupplemented, methionine depleted media (1 hr) and labeled with Aha (2 hr, 1 mM). The culture was then rinsed (1xPBS; 37 °C) and treated with NPPOC-NHO-BCN (100 μM in DMEM, 2 hr). Cells were then fixed (MeOH, -20 °C, 10 min) Activation was achieved either by using a photomask or a two-photon (2P) microscope (Olympus FV1000 MPE BX61 Multi-photon Microscope). For the former, a chrome photomask was placed between the light source (OmniCure series 1500) and the labeled cell culture. The cells were irradiated (10 mW cm^{-2}; 5 min; light intensity measured with Cole-Palmer series 9811 radiometer) and rinsed (1xPBS). For the latter, labeled cells were activated by irradiation (770 nm, 85% laser power). Activated proteins were then coupled to FAM-BA (100 nM, 100 mM aniline, RT, 1 hr, in the dark), rinsed (1xPBS; 3 times), and imaged by confocal microscopy.

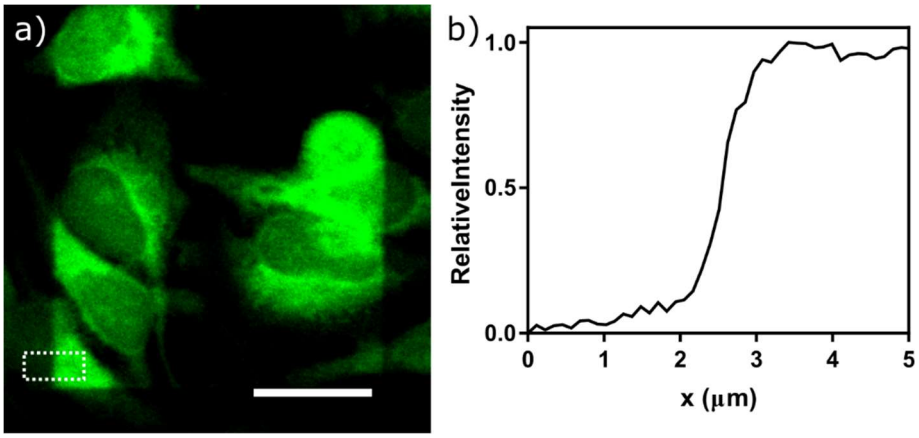

Figure A8. Resolution of protein activation by 2P microscopy. (a) two-photon (λ = 730 nm) activation of proteins visualized by FAM-BA (scale bar = 10 µm). (b) Plot profile of white inset of (a) demonstrates ~1 µm patterning resolution.

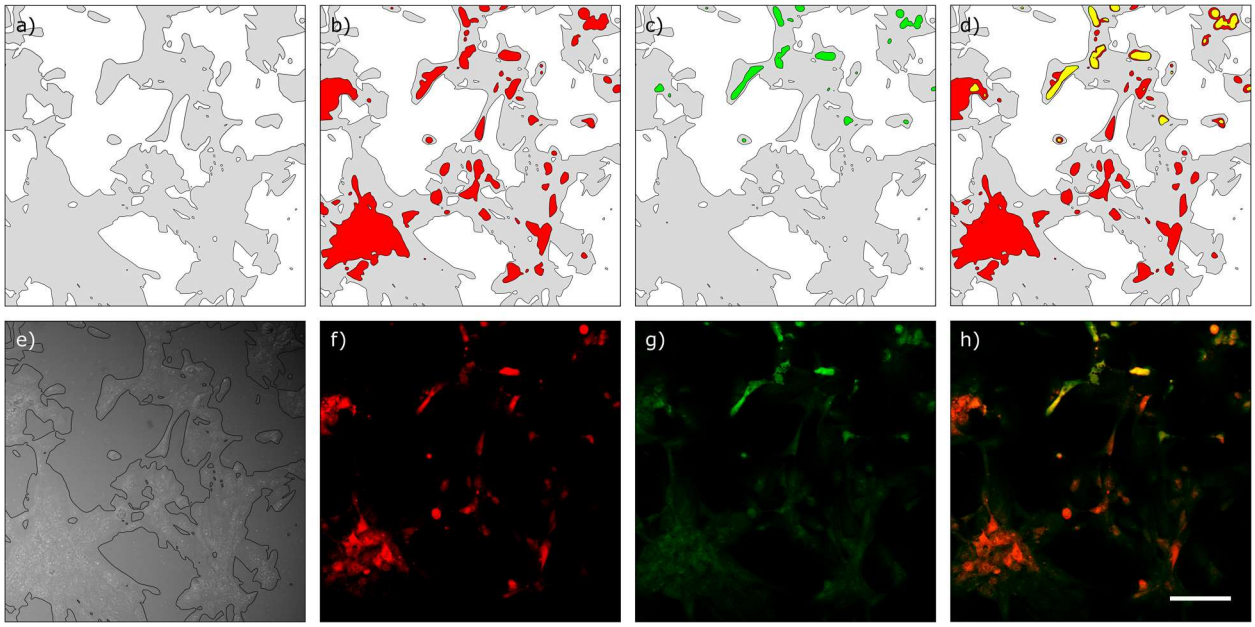

Figure A9. Background staining of image-guided photoactivation in mixed cell culture. An offset of Figure 13 that demonstrates labeling only in the activated areas. The total cell area (a) of an HS5a coculture brightfield image (e; perimeter indicated for emphasis). Cells endogenously express either GFP or mCherry. (b,f)

A fluorescent image is generated using immunohistochemistry against mCherry. The photomask (Figure 13c) is imparted by two-photon lithography to activate metabolically labeled proteins in those areas. The activation is visualized by coupling through an oxime condensation between activated proteins and FAM-BA (c,g). (d) A comparison of (b) and (c) illustrates the intersection (yellow) of the areas of interest and the labeled areas demonstrating that areas outside the irradiation window are not activated. FAM-BA labeling occurs only in irradiated areas and is not simply co-localized with mCherry immunohistochemistry. (h) Overlay of (f) and (g). (Scale bar (a-h) = 50 μm)

Isolation of Activated Proteins by Affinity Column Chromatography

Cells were cultured and their proteins were labeled as described above. Instead of coupling to the fluorescent FAM-BA proteins were condensed with biotin-BA (100 μM, 100 mM aniline, 5 hr, RT). Unreacted biotin-BA was removed by centrifugal desalting column (ThermoFisher, 89882). Streptavidin resin (300 uL; Fisher, PI20347) was pretreated by removing the storage solution (all centrifugations 1000xg, 120s) replacing with coupling buffer (1xPBS, 2 M NaCl, 0.5% SDS, 3x). The resin was then incubated with biotinylated protein (500 μL, 3 mg/mL, overnight, RT). The loaded resin was then washed once with 5 different washing solutions (binding buffer, 2 M NaCl, 6 M urea, 80% CH_3CN/1%TFA, 25 mM HEPES). The immobilized streptavidin was then denatured in elution buffer (2% SDS, 30 mM biotin, 50 mM PO_4, 100 mM NaCl, 6 M urea, 2 M thiourea, pH 12[184]) for 15 minutes at room temperature followed by 15 minutes at 90 °C. Proteins were eluted by centrifugation (1000xg, 120 s) and the resin was washed once with binding buffer. The eluted protein solution was then neutralized (1 M HCl), concentrated with a centrifugal filter (3000 kDa MWCO, 15,000xg, 30 min), and salts were diluted by the addition of

binding buffer and centrifugation (3x). The concentrated protein solutions were then added to and equal volume of 2xSDS sample buffer (100 mM Tris-Cl, 4% sodium dodecyl sulfate, 0.2% bromophenyl blue, 20% glycerol) and a PAGE gel was run as described previously. Gels were stained with silver, and imaged. Alternatively, protein solutions (1 μL) are blotted directly on nitrocellulose and visualized with appropriate antibodies. Images were quantified in FIJI.

Labeling and Photoactivation of Zebrafish

Zebrafish larvae were generated as described. After 30 hpf-7 dpf zebrafish were immersed in NCAA larvae media (0.1 mg methylene blue, 1.2 g Instant Ocean®, 1 L DIH_2O, 4 mM Aha, 72 hrs). Larvae were then anesthetized (1xPBS; 0 °C) and fixed (MeOH, 0 °C, 3x5 min; MeOH, -20 °C, overnight). After rehydration with successive washes of decreasing methanol concentration (75, 50, 25, 0% MeOH in PBST; 5 min each, RT), the larvae is reduced (DTT, 10 mM, 5 hrs) to prevent undesired labeling, then treated with the primary antibody (anti-α-tubulin, 0.3 μg/mL, 16 hrs, RT; Cell Signaling, 5335S; or anti-FLK1 1 μg/mL, Kerafast, ES1003) and rinsed (1xPBST; 3x5 min). Larvae are then treated simultaneously with the small molecule probe (100 μM, PBST, 5 hrs) and secondary antibody (anti-rabbit-Alexa 594, 1 μg/mL; Invitrogen, A11037) then rinsed (1xPBST; 3x5 min). Labeled proteins are activated either by using a photomask or a 2P microscope. For the former, a photomask was placed between the light source (OmniCure series 1500) and the labeled cell culture then the cells were irradiated (10 mW cm^{-2}; 5 min; light intensity measured with Cole-Palmer series 9811 radiometer). For the latter, labeled cells were activated by 2P irradiation (770 nm, 60% laser power; Olympus FV1000 MPE BX61 Multi-photon Microscope). Activated proteins were then coupled to FAM-BA (100 nM, 100 mM

aniline, RT, PBST, 2 hr, in the dark), rinsed (1xPBST; 3x5 min), and imaged by confocal or 2P microscopy.

Alternatively, zebrafish embryos (24 hpf) can be injected with Aha (10 nL, 70 mM) and immersed in Aha embryo media until after emergence (72 hpf). The larvae are then fixed, reduced, and labeled with NPPOC-NHO-BCN as described above. Larvae must be placed in agar (1.4%) to immobilize them during 2P irradiation (770 nm, 60% laser power). Larvae are then removed from agar so that activated proteins can be coupled to FAM-BA (100 nM, 100 mM aniline, RT, PBST, 2 hr, in the dark), before rinsing (1xPBST; 3x5 min), and returning them to agar (1.4%). Fish are then imaged by confocal or 2P microscopy.

Background staining in zebrafish

Although no signal was observed for any other negative control, a significant level of background staining was observed for the methionine negative control with all other positive treatments (+Met, +NPPOC-NHO-BCN, 2 hrs, +hν, +FAM-BA, 12 hrs). It was hypothesized that this background was the result of undesired thiol-yne condensations between thiols present on proteins and the bicyclononyne functional group of the probe. To overcome this, an experiment testing combinations of reducing (DTT, BME, GSH, 10 mM, overnight), alkylating (IAM, NEM, 20 mM, overnight), and blocking conditions was conducted (Figure A10). Treating with the blocking solution (10% goat serum, 5% BSA, PBDTT) did not provide any benefit. Treatment with DTT alone appeared to provide the best results affording a signal to noise of 2:1 of the treatment compared to the control, while significantly reducing non-irradiated background.

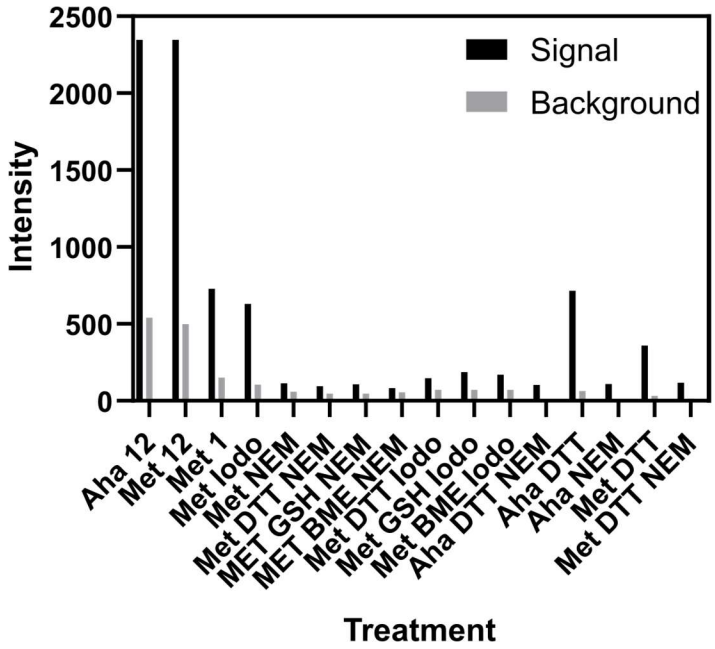

Figure A10. Treatments to reduce background labeling.

Range 1: 10 to 151 Graphics — Next Match, Previous Match

Score	Expect	Method	Identities	Positives	Gaps
74.7 bits(182)	7e-21	Compositional matrix adjust.	43/144(30%)	75/144(52%)	7/144(4%)

```
Query  15   ILVELDGDVNGHKFSVSGEGEGDATYGKLTLKFICTTGK-LPVPWPTLVTTLTYGVQCFS  73
            I + ++G VNGHKF + G+G+G    G  ++      G  LP  +  L T   YG + F+
Sbjct  10   IKLRMEGAVNGHKFVIEGDGKGKPFEGTQSMDLTVKEGAPLPFAYDILTTVFDYGNRVFA  69

Query  74   RYPDHMKQHDFFKSAMPEGYVQERTIFFKDDGNYKTRAEV---KFEGDTLVNRIELKGID  130
            +YP  +   D+FK    PEGY  ER++ ++D G      ++   K   D  V +I   G++
Sbjct  70   KYPQDIP--DYFKQTFPEGYSWERSMTYEDQGICVATNDITLMKGVDDCFVYKIRFDGVN  127

Query  131  FKEDGNILGHK-LEYNYNSHNVYI  153
            F  +G ++  K L++  ++  +Y+
Sbjct  128  FPANGPVMQKKTLKWEPSTEKMYV  151
```

Range 2: 179 to 204 Graphics — Next Match, Previous Match, First Match

Score	Expect	Method	Identities	Positives	Gaps
15.8 bits(29)	0.83	Compositional matrix adjust.	8/26(31%)	12/26(46%)	0/26(0%)

```
Query  66   TYGVQCFSRYPDHMKQHDFFKSAMPE  91
            TY  + F + PD     D+ K  + E
Sbjct  179  TYKAKKFVQLPDLSHDKDYNKVKLYE  204
```

Range 3: 212 to 227 Graphics — Next Match, Previous Match, First Match

Score	Expect	Method	Identities	Positives	Gaps
13.1 bits(22)	4.8	Compositional matrix adjust.	4/16(25%)	9/16(56%)	0/16(0%)

```
Query  138  LGHKLEYNYNSHNVYI  153
            L  + +Y++  H + I
Sbjct  212  LPRQAKYHFVDHRIEI  227
```

Range 4: 191 to 198 Graphics — Previous Match, First Match

Score	Expect	Method	Identities	Positives	Gaps
12.7 bits(21)	6.4	Compositional matrix adjust.	4/8(50%)	5/8(62%)	0/8(0%)

```
Query  138  LGHKLEYN  145
            L H  +YN
Sbjct  191  LSHDKDYN  198
```

Figure A11. BLAST comparison of EGFP and GRCFP.

Range 1: 8 to 225 Graphics Next Match Previous Match

Score	Expect	Method	Identities	Positives	Gaps
210 bits(535)	1e-73	Compositional matrix adjust.	109/219(50%)	142/219(64%)	15/219(6%)

```
Query  4    IKPDMKIKLRMEGAVNGHKFVIEGDGKGKPFEGTQSMDLTVKEGAPLPFAYDILTTVFDY  63
            +K +M +K  MEG VNGHKFVI G+G G PF+G Q+++L V EG PLPF+ DIL+  F Y
Sbjct  8    LKEEMTMKYHMEGCVNGHKFVITGEGIGYPFKGKQTINLCVIEGGPLPFSEDILSAGFKY  67

Query  64   GNRVFAKYPQDIPDYFKQTFPEGYSWERSMTYEDQGICVATNDITLMKGVDDCFVYKIRF  123
            G+R+F +YPQDI DYFK + P GY+W RS  +ED  +C+   DIT+    ++C  +K  F
Sbjct  68   GDRIFTEYPQDIVDYFKNSCPAGYTWGRSFLFEDGAVCICNVDITVSVK-ENCIYHKSIF  126

Query  124  DGVNFPANGPVMQKKTLKWEPSTEKMY--VRDGVLKGDVNMALLLEGGGHYRCDFKTTYK  181
            +GVNFPA+GPVM+K T  WE S EK+    + G+LKGDV+M LLL+ GG YRC F T YK
Sbjct  127  NGVNFPADGPVMKKMTTNWEASCEKIMPVPKQGILKGDVSMYLLLKDGGRYRCQFDTVYK  186

Query  182  AKK---------FVQLPDLSHDKD---YNKVKLYEHAEA  208
            AK          F+Q   L  D+      K +L EHA A
Sbjct  187  AKSVPSKMPEWHFIQHKLLREDRSDAKNQKWQLTEHAIA  225
```

Figure A12. BLAST comparison of zsYellow and GRCFP.

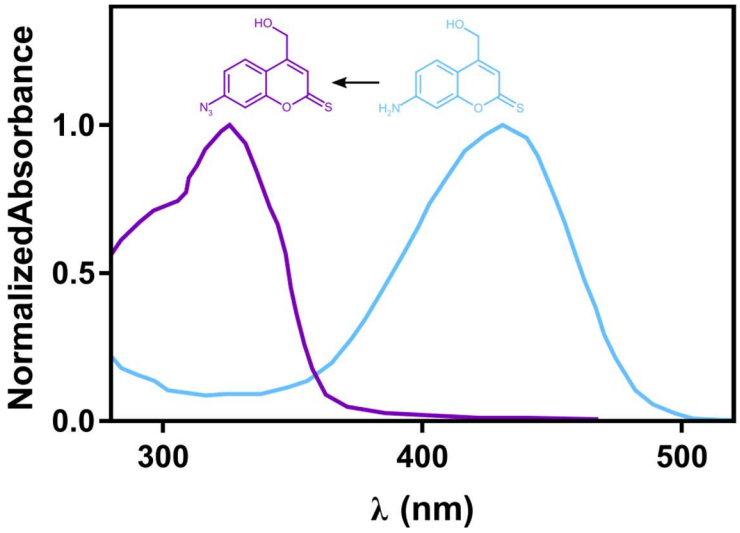

Figure A13. Absorbance shift of NH_2-tCM-OH upon installation of the azide at position 7.

Synthesis of N_3-*o*NB-NHS

N_3-*o*NB-NHS was synthesized as described previously[97].

Synthesis of N_3-BODIPY-OSu[145]

Synthesis of 2,2-difluoro-8-(4-hydroxyphenyl)-4,6,10,12-tetramethyl-1lambda5,3-diaza -2-boratricyclo[7.3.0.0^{3,7}]dodeca-1(12),4,6,8,10-pentaen-1-ylium-2-uide (HO-BODIPY)*:*

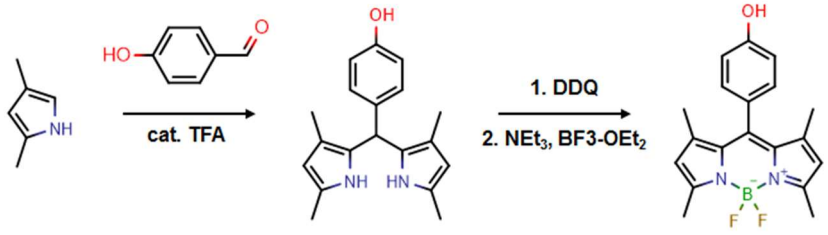

2,4-Dimethylpyrrole (1.5 mL, 1.34 g, 14.13096 mmol, 2x) and 4-hydroxybenzaldehyde (0.87155 g, 7.06548 mmol, 1x) were dissolved in 120 mL DCM and degassed by Argon for 20 min. A catalytic amount of TFA (4 drops) was added and stirred overnight (15 h) at room temperature. Then a solution of DDQ (1.6509 g, 7.06548 mmol, 1x) in 150 mL DCM was added dropwise and the mixture was stirred for 0.5 h. Triethylamine (10 mL, 71.7462 mmol, 10x) was then added. Finally, BF_3OEt_2 (10 mL, 81.0258 mmol, 10x) were added, and the mixture was stirred for 1 h at room temperature. After the reaction, the mixture was evaporated under reduced pressure. The dried crude was dissolved in DCM and washed with brine, sat. $NaHCO_3$, and water. The organic layer was dried over $MgSO_4$, filtered, and evaporated under reduced pressure. The obtained crude was purified by flash column chromatography, eluting with DCM followed by an additional purification by using CombiFlash with 10% methanol gradient in DCM and collected fractions to give red crystal sample (630 mg, 26.3 % yield). ^{1}H NMR (500 MHz, CDCl3) δ 7.11 (d, J=8.26 Hz, 2H), 6.95 (d, J=8.26 Hz, 2H), 5.98 (s, 2H), 4.76 (d, J=1.36 Hz, 2H), 2.55 (s, 6H),

1.44 (s, 6H). ^{13}C NMR (300 MHz, CDCl3) δ 156.29, 155.30, 143.13, 141.74, 131.83, 129.41, 127.21, 121.11, 116.09, 68.76, 46.92, 14.49, 8.67. HRMS (ESI+) Calculated for $C_{19}H_{19}BF_2N_2O$ [M+H]+, 341.1635; observed 341.1631 (Δ = 1.21 ppm).

Synthesis of 2,2-difluoro-4,6,10,12-tetramethyl-8-[4-(prop-2-yn-1-yloxy)phenyl]-1lambda 5,3-diaza-2-boratricyclo[7.3.0.0^{3,7}]dodeca-1(12),4,6,8,10-pentaen-1-ylium-2-uide (Alkyne-BODIPY)*:*

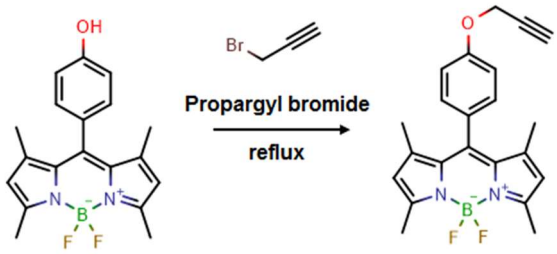

BODIPY-Ph-OH (0.41 g, 1.20524 mmol), K_2CO_3 (0.8433 g, 15.27 mmol, 5x) and 80 wt% Propargyl bromide (1.2 mL,1.8 g, 11.04 mmol, 9x) were dissolved in 20 mL acetone and refluxed (60 °C) for 6 h. The reaction mixture was then evaporated under reduced pressure. The residue was re-dissolved in Ethyl acetate and washed with water (3x). The organic layer was dried over $MgSO_4$, filtered, and evaporated under reduced pressure. The crude product was purified by flash column chromatography eluting with ethyl acetate/hexanes (1/9). Evaporation under reduced pressure provided a red crystal (470 mg, quantitative yield). ^{1}H NMR (500 MHz, $CDCl_3$) δ 7.19 (d, J=8.33 Hz, 2H), 7.09 (d, J=8.30 Hz, 2H), 6.52 (q, J = 6.4 Hz, 1H), 5.98 (s, 2H), 4.76 (d, J=1.36 Hz, 2H), 2.62 (td, J=7.36, 2.30 Hz, 1H), 2.56 (s, 1H), 2.55 (s, 6H), 1.42 (s,

6H). ^{13}C NMR (300 MHz, $CDCl_3$) δ158.15, 155.37, 143.08, 141.49, 131.79, 129.26, 128.06, 121.12, 115.66, 69.10, 56.05, 17.85, 14.52, 14.46. HRMS (ESI+) Calculated for $C_{22}H_{21}BF_2N_2O$ [M+H]+, 379.1792; observed 379.1801 (Δ = 2.44 ppm).

Synthesis of 2,5-dioxopyrrolidin-1-yl 3-(4-hydroxyphenyl)propanoate (HO-Ph-OSu)*:*

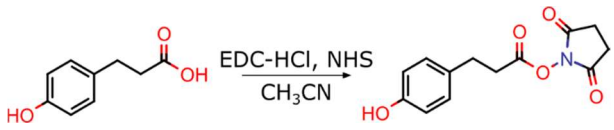

3-(4'-hydroxyphenyl)propionic acid (4.9959 g, 29.9429 mmol, 1x), N-hydroxysuccinimide (5.2901 g, 45.0456 mmol, 1.5x), and N-(3-dimethylaminiopropyl)-N'-ethylcarbodiimide hydrochloride (EDC-HCl, 8.7159 g, 45.0113 mmol, 1.5x) were dissolved in anhydrous acetonitrile (100 mL) and stirred overnight at room temperature (15 h). Next, the solvent was evaporated under reduced pressure, and the crude was re-dissolved in DCM. The organic layer was washed with dH_2O (6x), dried over $MgSO_4$, filtered, and evaporated under reduced pressure. The crude product was purified by flash column chromatography using a solvent gradient of Ethyl acetate in Hexane (0-60%) to obtain a white solid (4.30 g. 52.5% yield). ^{1}H NMR (500 MHz, $CDCl_3$) δ 7.07 (d, J=8.10 Hz, 2H), 6.76 (d, J=8.10 Hz, 2H), 2.96 (t, J=7.82 Hz, 2H), 2.85 (m, 6H). ^{13}C NMR (300 MHz, $CDCl_3$) δ169.09, 154.34, 129.43, 115.47, 32.91, 29.63, 25.56.

Synthesis of 2-(4-{3-[(2,5-dioxopyrrolidin-1-yl)oxy]-3-oxopropyl}phenoxy)-2-fluoro-4,6,10,12-tetramethyl-8-[4-(prop-2-yn-1-yloxy)phenyl]-1lambda5,3-diaza-2-boratricyclo[7.3.0.0^{3,7}]dodeca-1(12),4,6,8,10-pentaen-1-ylium-2-uide (Alkyne-BODIPY-OSu)*:*

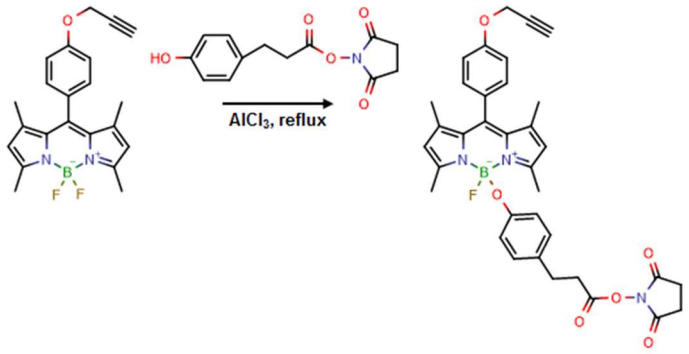

BODIPY-Ph-Alkyne (670 mg, 1.7714 mmol) and $AlCl_3$ 177.1 mg,1.3286 mmol, 0.75x) were dissolved in anhydrous DCM (40 mL) and the reaction mixture was refluxed (60oC) for 15 min. After cooling to room temperature, NHS-activated 3-(4'-hydroxyphenyl) propionic acid (HO-Ph-OSu, 441.5 mg, 1.7714 mmol, 1x) in DCM (80 mL) was added and refluxed for 60 min. The reaction mixture was then evaporated under reduced pressure. The crude product was re-dissolved in ethyl acetate and filtered through a pad of aluminum oxide. The solvent was removed under reduced pressure. The crude product was purified by flash column chromatography eluting with a solvent gradient of Ethyl acetate in hexane (0-50%). In addition to the desired product, the starting material and doubly substituted products were also isolated (data not shown). Evaporation under reduced pressure provided the product (239.6 mg, 21.7% yield). ^{1}H NMR (500 MHz, $CDCl_3$) δ 7.23 (d, J=8.45 Hz, 1H), 7.17 (d, J=8.11 Hz, 1H), 7.12 (m, 2H), 6.92 (d, J=8.41, 2H), 6.48 (m, 2H), 5.93 (dd, J=95.5, 8.43 Hz, 2H), 4.77 (d, J=1.93 Hz, 2H), 2.90(m, 2H), 2.84 (m, 6H), 2.57, (s, 1H), 2.51 (s, 6H), 1.43 (s, 6H). ^{13}C NMR (300 MHz, $CDCl_3$) δ169.06, 167.91, 154.43, 131.19, 129.40, 128.91, 115.50, 69.05, 56.06, 32.92, 32.84, 29.63, 25.55, 14.82, 14.59.

Synthesis of 1-azido-2-{2-[2-(2-azidoethoxy)ethoxy]ethoxy}ethane (N_3-TEG-N_3)*:*

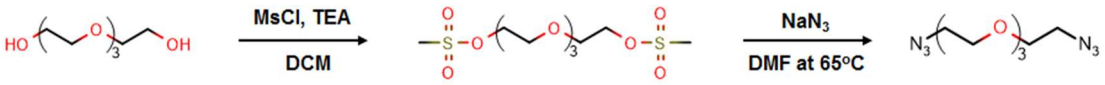

Tetraethylene glycol (TEG, 9 mL, 10 g, 51.4835mmol) and triethylamine (TEA, 21.53 mL, 154.456 mmol, 3x) were dissolved in anhydrous DCM (210 mL) and placed in an ice bath. Methanesulfonyl chloride (MsCl, 12.0 mL, 154.456 mmol) was added to the mixture and stirred at 0 °C for 2.5 h and then at room temperature for 4 h. The reaction mixture was evaporated under reduced pressure. The reaction crude was dissolved in DCM (200 mL) washed with 3% HCl (200 mL) and water (400 mL) twice. The organic layer was dried over $MgSO_4$, filtered, and evaporated under reduced pressure. The product was used without additional purification.

The mesylated TEG was reacted with NaN_3 (16.7353 g, 257.42676 mmol, 5x) in DMF (200 mL) at 65 oC for 18 h. The solvent was evaporated under reduced pressure and then excess NaN_3 was removed by filtration through a pad of Celite, washing with ether (Et_2O). Finally, Et_2O was evaporated under reduced pressure. The reaction crude was dissolved in DCM (200 mL) washed with 3% HCl (200 mL) and water (400 mL) twice. The organic layer was dried over $MgSO_4$, filtered, and evaporated under reduced pressure. The product was a pale yellow oil (12.35 g, 97.2 % yield). ^{1}H NMR (500 MHz, $CDCl_3$) δ 3.70 (m, 12H), 3.42 (t, J=4.93 Hz, 4H). ^{13}C NMR (300 MHz, $CDCl_3$) δ 70.70, 70.01, 50.70. HRMS (ESI+) Calculated for $C_8H_{16}N_6O_3$ $[M+NH_4]^+$, 262.1622; observed 262.1627 (Δ = 1.7 ppm).

Synthesis of 8-(4-{[1-(2-{2-[2-(2-azidoethoxy)ethoxy]ethoxy}ethyl)-1,2,3-triazol-4-yl] methoxy}phenyl)-2-(4-{3-[(2,5-dioxopyrrolidin-1-yl)oxy]-3-oxopropyl}phenoxy)-2-fluoro-4, 6,10,12-tetramethyl-1lambda5,3-diaza-2-boratricyclo[7.3.0.0^{3,7}]dodeca-1(12),4,6,8,10-penta en-1-ylium-2-uide (N_3-BODIPY-OSu)*:*

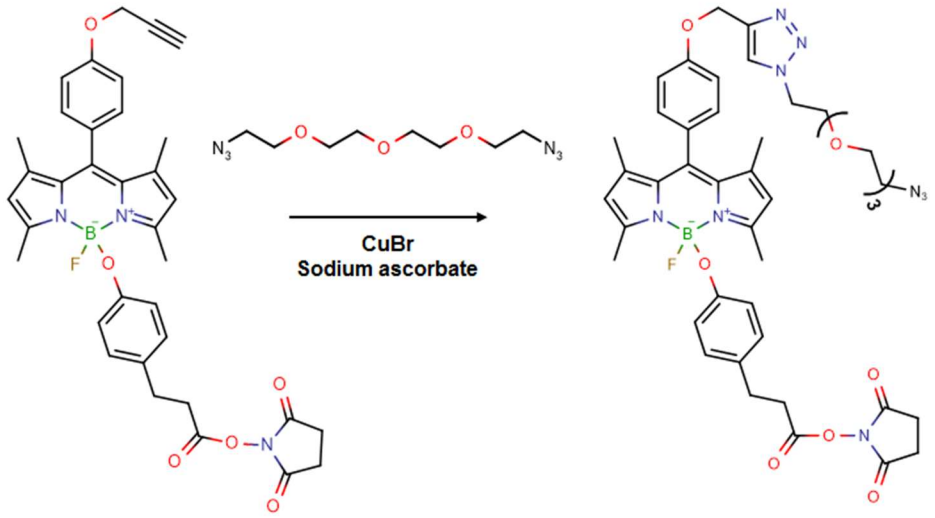

Alkyne-BODIPY-OSu (359.6 mg, 0.58 mmol, 1x) and N_3-tetraethyleneglycol (TEG)-N_3 (2.5 mL, 11.6 mmol, 20x) were dissolved in 10 mL DMF and resultant mixture was degassed by N_2 for 30 min. CuBr (127 mg, 0.87 mmol, 1.5 x) and sodium L-ascorbate (258 mg, 1.3 mmol, 2.2x) were added and allowed to stir for 1 day under a N_2 atmosphere. The reaction mixture was then evaporated under reduced pressure and the residue was re-dissolved in 10% MeOH in DCM and filtered through neutral aluminum oxide with 5-10% MeOH in DCM. The solvent was evaporated under reduced pressure and the product was purified by two automated flash columns in series (0-10% MeOH in DCM 0-5% MeOH in DCM). Obtained 57.0 mg of a bright orange wax (11% yield). ^{1}H NMR (500 MHz, $CDCl_3$) δ 7.95 (s, 1H), 7.23 (d, J=8.07 Hz, 1H), 7.15 (cm, 3H), 6.92 (d, J=8.15 Hz), 6.49 (d, J=7.99 Hz, 2H), 5.92 (s, 2H), 5.28 (s, 2H), 4.61 (s, 2H), 3.91

(cm, 2H), 3.65 (cm, 10H), 3.37 (cm, 2H), 2.90 (cm, 2H), 2.84 (cm, 6H), 2.50 (s, 6H), 1.43 (s, 6H). ^{13}C NMR (300 MHz, $CDCl_3$) δ 176.25, 168.98, 167.88, 131.10, 129.38, 128.88, 115.60, 115.48, 70.70, 70.59, 70.04, 61.74, 57.03, 50.69, 32.94, 29.65, 25.88, 14.62, 14.51.

Synthesis of N_3-PEG-*o*NB-N_3

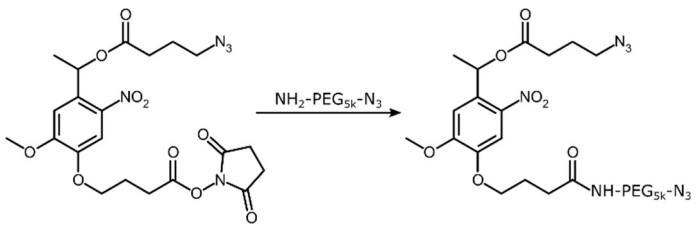

N_3-*o*NB-NHS (24.3 mg, 47.9 μmol, 1.5x) and NH_2-PEG-N_3 (164.5 mg, 32.9 μmol, 1x) were added to a vial and dissolved in DMF (2 mL). DIPEA (30 μL) was added via syringe and the reaction was stirred overnight (16 h) at room temperature. The reaction solution was dialyzed against dH_2O (1 kDa cellulose MWCO filter, 48 h). The solvent was then removed under reduced pressure and the product was used without additional purification. A white solid was obtained (177 mg, quantitative yield).

Synthesis of N_3-PEG-BODIPY-N_3

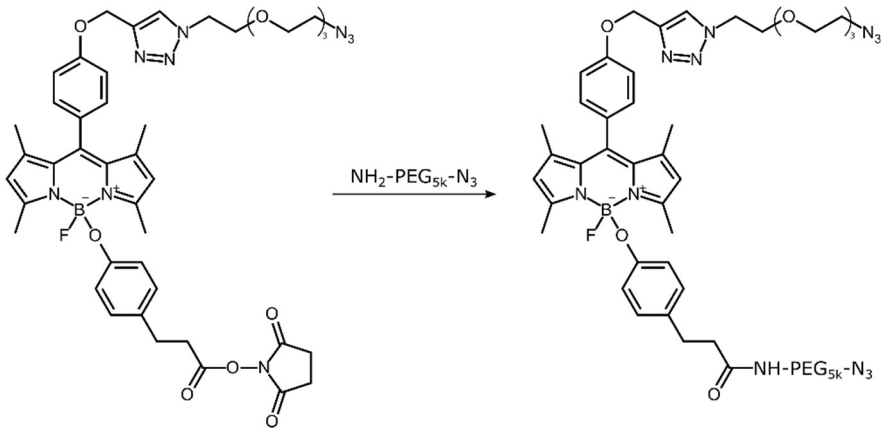

N_3-BODIPY-OSu (10.8 mg, 12.5 μmol, 1x) was dissolved in DMF and added to vial containing NH_2-PEG_{5k}-N_3 (58.8 mg, 11.8 μmol, 1x). Anhydrous NEt_3 was added via syringe and the reaction was stirred overnight (16 h) at room temperature. The solvent was then removed under reduced pressure and the product was used without additional purification. An orange solid was obtained (152 mg, quantitative yield).

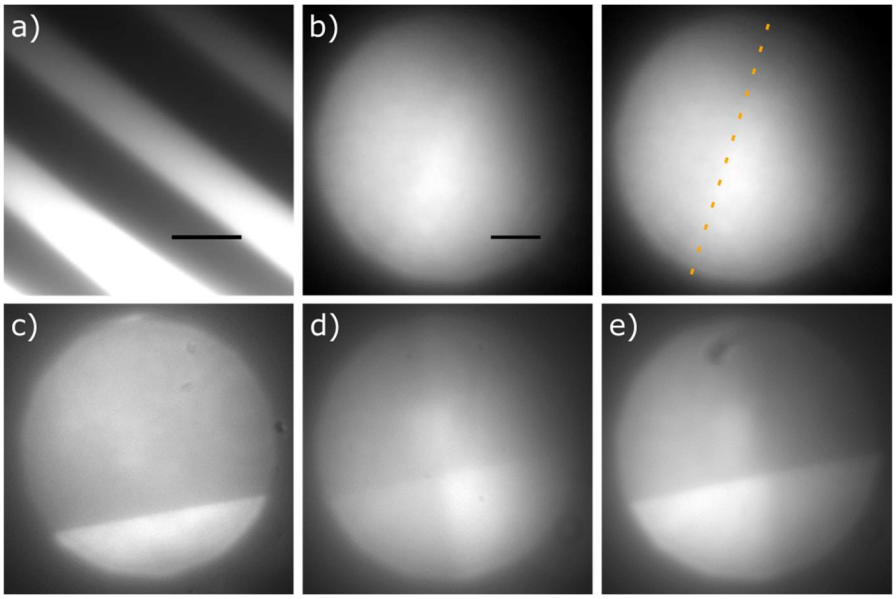

Figure A14. Photopatterning of fluorescent small molecules (*o*NB-Cy5 and BODIPY-Cy7) by selective light irradiation of BODIPY and *o*NB coupled PEG-based hydrogels. (a) Irradiation of *o*NB-Cy5 coupled hydrogels with light (λ = 365 nm) through a photomask with horizontal parallel lines (400 μm spacing) releases Cy5 (Scale bar = 400 μm). (b) Irradiation of BODIPY-Cy7 coupled hydrogels with green light (λ = 505 nm) through a photomask with vertical parallel lines releases Cy7 in select regions. (c) and (d) Images of a multicomponent gel subjected to sequential light exposure (505 nm followed by 365 nm) prior to imaging. (e) Overlay image of (c) and (d) (Scale bar (b)=(c)=(d)=(e)= 100 μm).

Kinetic analysis of N_3-BODIPY-OSu

The photodegradable N_3-BODIPY-OSu was dissolved in DMSO (0.01 mM) in centrifuge tubes. The solution was exposed to light at 505 nm, and intensities of 5, 10, 20 mW cm^{-2} for various amounts of time (Figure A15). The solution was collected at each predetermined time point, and

fluorescence was measured using a spectrophotometer (Molecular Devices SpectraMax M5) for each time point. Fluorescence was measured in triplicates (λ_{ex} = 503 nm, λ_{em} = 520 nm).

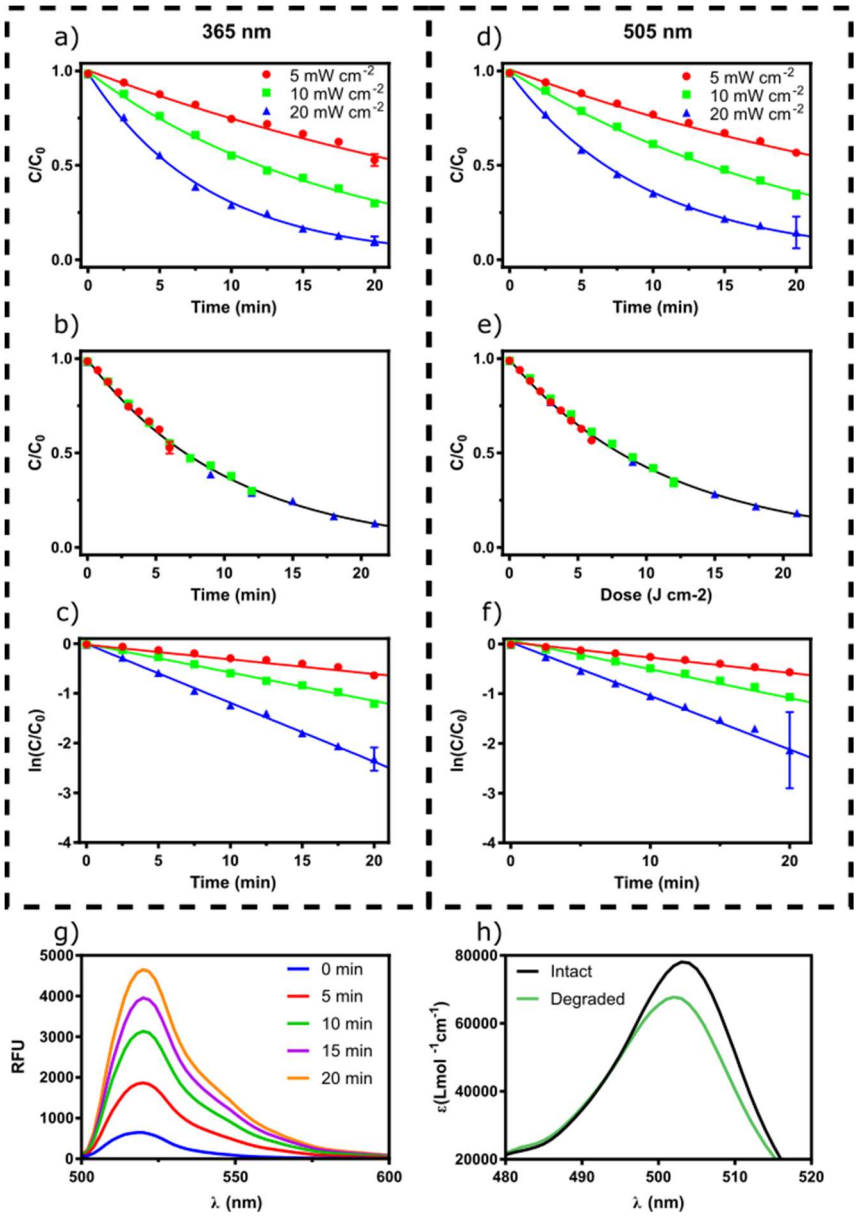

Figure A15. Kinetic analysis of N_3-BODIPY-OSu under 365 and 505 nm irradiation. (a,d) Light irradiation under increasing light intensity results in faster degradation as expected. The data are fit, separately, to exponential decay curves. (b,e) When the light intensities are converted to light dosages, representing the

total energy imparted by the incident light, the data aligns on a single logarithmic curve. (c,f) The data is transformed by plotting the natural log of the ratio of concentration at time *t* to initial concentration produces data that is fit to a linear curve to find the rate constant, *k*. (g) A dramatic increase in fluorescence is observed over the course of 20 minutes (h) UV-Vis of BODIPY before and after irradiation at 505 nm results in slight reduction in absorptivity.

Kinetic analysis of N_3-*o*NB-OSu

Data for *o*NB degradation under 365 nm irradiation was collected previously and used here with permission[97].

To determine *o*NB reactivity under 505 nm light, a solution of N_3-*o*NB-OSu in MeOD (70 mM) was prepared. The solution (0.5 mL) was drawn into a syringe and injected between two parallel glass plates sealed with a rubber gasket. The sample was irradiated (505 nm, 20 mW cm^{-2}) for the predetermined time (0-120 min) before being drawn out *via* syringe for analysis by ^1H NMR. By closely monitoring the hydrogens corresponding to the methyl group vicinal to the ester (δ1.57) as the molecule transitions to the ketone (δ4.05) the reaction progress was determined. Since, no reaction was observed for the duration of the experiment (120 min), a single data point was collected under irradiation at 365 nm. The result matched the previously determined kinetics[97] (data not shown).

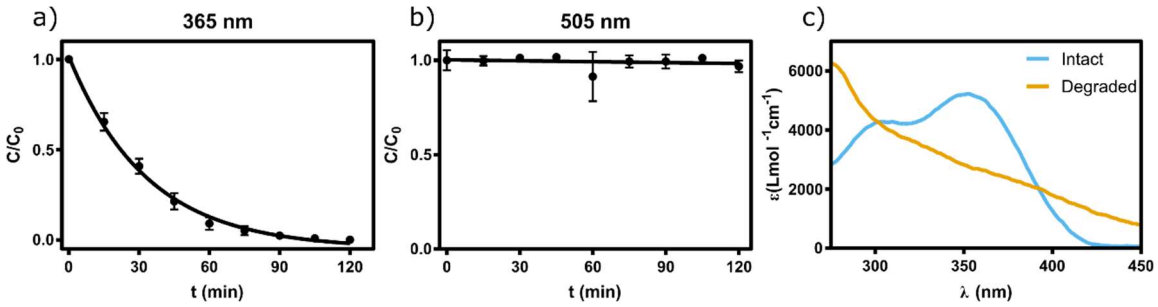

Figure A16. Kinetic analysis of N_3-*o*NB-OSu under 365 and 505 nm irradiation. (a) Irradiation of *o*NB under 365 nm results in photo-cleavage over several minutes. The data is fit to an exponential decay curve (reproduced with permission[97]) (b) Irradiation of *o*NB under 505 nm results in no observable photocleavage. (c) UV-Vis absorbance of *o*NB before and after irradiation at 365 nm results in a dramatic change to its absorption profile.

First-order degradation with a rate constant (k) that can be expressed as:

$$k = \frac{\varphi \varepsilon I}{N_A \hbar \nu}$$

where ϕ is the quantum yield, ε is the molar absorptivity of the sample, I is the intensity of light, N_A is Avogadro's number, h is the Planck constant, and ν is the frequency of the associated electromagnetic wave.

Table A1. Photokinetic properties of *o*NB and BODIPY.

Compound	ε (λ = 365 nm)	ϕ (λ = 365 nm)	εϕ (λ = 365 nm)	ε (λ = 505 nm)	ϕ (λ = 505 nm)	εϕ (λ = 505nm)
*o*NB	4780 M^{-1} cm^{-1}	0.02	9.50 M^{-1} cm^{-1}	0	0	0
BODIPY	7100 M^{-1} cm^{-1}	4.49 x 10^{-3}	31.9 M^{-1} cm^{-1}	76000 M^{-1} cm^{-1}	3.00 x 10^{-4}	22.8 M^{-1} cm^{-1}
BODIPY-mCherry	7100 M^{-1} cm^{-1}	1.71 x 10^{-6}	0.01 M^{-1} cm^{-1}	76000 M^{-1} cm^{-1}	6.43 x 10^{-6}	0.49 $M^{-1}cm^{-1}$

ε – molar absorptivity

ϕ – quantum yield

λ – wavelength

Synthesis of N_3-BODIPY-mCherry

To mCherry (300 µL, 1.924 mg/mL, 2 nmol, 1x) in carbonate buffer (0.1 M, pH = 8.3) was added N_3-BODIPY-OSu (17 µg, 20 nmol, 10x) dissolved in DMF (30 µL). The reaction was allowed to progress at room temperature for 2.5 hours before dilution with 1xPBS and dialysis (1 kDa) against 1xPBS for 48 hours. After dialysis the complex was concentrated by centrifugal filtration (3 kDa, 4000 rpm, 15 min).

Synthesis of N_3-*o*NB-mCerulean

N_3-*o*NB-mCerulean was synthesized as described above for N_3-BODIPY-mCherry substituting N_3-*o*NB-OSu for N_3-BODIPY-OSu and mCerulean for mCherry.

Estimation of protein functionalization

Since each fluorescent protein has multiple lysine residues and the terminal amine (mCherry: 24 K; mCerulean: 21 K), there is some interest in estimating the degree of functionalization, after protein coupling of the small photo-labile groups for calculations involving their inclusion in materials. Since the molar absorptivity of both photocages and proteins are known, a UV-Vis spectrum of the coupled proteins provides the relevant information for these calculations (Figure A17). It is important to subtract any native absorbance of the protein at the absorption maximum of the photocage in the coupled spectrum. Likewise, any absorbance from the photocage at the maximum absorbance of the protein should be subtracted. Then by comparing the adjusted maximum molar absorptivity of the individual components to the absorption of the final constructs the number of photocage (BODIPY or *o*NB) units per protein can be estimated. It was determined that an average of 4 BODIPY molecules were coupled to each mCherry, and 5 *o*NB molecules were coupled to each mCerulean.

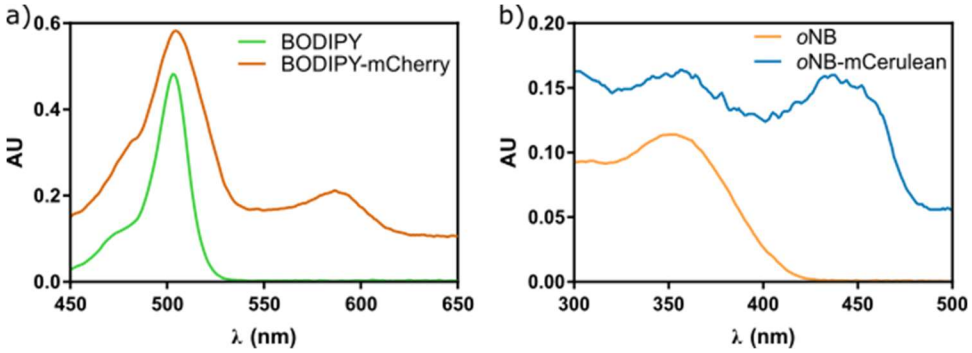

Figure A17. UV-vis of photocages and photocaged coupled proteins. a) UV vis of BODIPY and BODIPY-mCherry. b) UV vis of *o*NB and *o*NB-mCerulean. Since the molar absorptivity of both photocages and proteins are known, the degree of functionalization can be estimated.

Discovery of a potential FRET pair: BODIPY-mCherry:

During the photochemical experiments an interesting observation was made about the BODIPY-mCherry construct. The construct displayed two fluorescence peaks that corresponded to BODIPY (520 nm) and mCherry (610 nm) as expected (Figure A17). During light exposure (505 nm) over 60 minutes the fluorescence of BODIPY increased as molecule is cleaved, and, unexpectedly, the fluorescence of mCherry decreased (Figure A18). This is not simply a product of mCherry photobleaching as the protein does not appear to respond to extended irradiation at 505 nm (Figure A20). It is therefore hypothesized that this represents a FRET pair between BODIPY and mCherry, since the fluorescence of mCherry appears to be enhanced when bound to BODIPY. Although not the focus of this work this pair warrants further exploration.

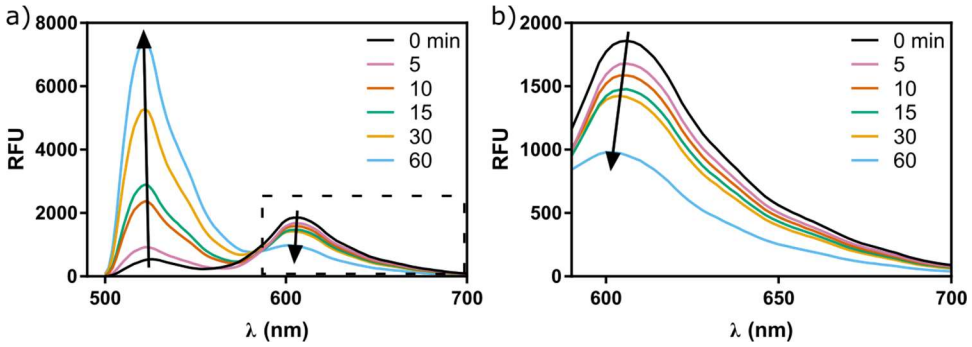

Figure A18. Solution-based photocleavage of N_3-BODIPY-mCherry. (a) With increasing irradiation time, the fluorescence of BODIPY (λ_{max}=520 nm) increases as expected. Interestingly, the fluorescent intensity of the coupled mCherry (λ_{max}=610 nm) decreases over time, indicating a potential FRET coupling between BODIPY and mCherry. (b) inset of a).

Photopatterning of single-protein materials

PEG_{20k}-tetraBCN (2 mM) was reacted with N_3-BODIPY-mCherry (0.1 mM) dissolved in DMSO in PBS with shaking at room temperature for 1 h. $PEG_{3.5k}$-diazide crosslinker (4 mM) were then added and vortexed to make homogeneous solution. The gels were formed between two Rain-X® coated glass slides with 1 mm rubber spacers (2 hr). The gels were then placed into glass scintillation vials and washed (1xPBS, pH 7.2, 48 hrs) to remove any unbound protein. Next photocage-protein coupled hydrogels were irradiated with light (BODIPY-mCherry:505 nm, 20 mW cm^{-2}, 1 hr) to release protein into the solution.

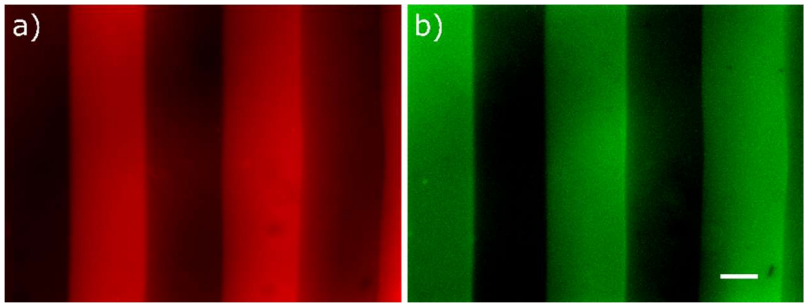

Figure A19. Gel photopatterning of N_3-BODIPY-mCherry under 505 nm irradiation using a photomask with features of 400 μm parallel lines. (a) mCherry is released from the material after light exposure and diffusion. (b) The fluorescence of BODIPY is no longer suppressed after light exposure, providing a unique indicator for where molecules have been cleaved out of the material. Scale bar = 200 μm.

Exploration of fluorescent protein photobleaching

Non-modified mCherry and mCerulean proteins were dissolved in PBS to be 0.1 mM, and the solutions were irradiated with light (365 nm and 505 nm, 20 mW cm^{-2}, 5, 10, 15, 30, 60 min) to check the photobleaching of protein itself. The solutions were collected at predetermined time point, and fluorescence experiment using plate reader were performed for each time point in triplicates (mCherry: λ_{ex} =590 nm, λ_{em} = 614 nm, mCerulean: λ_{ex} =433 nm, λ_{em} = 478 nm).

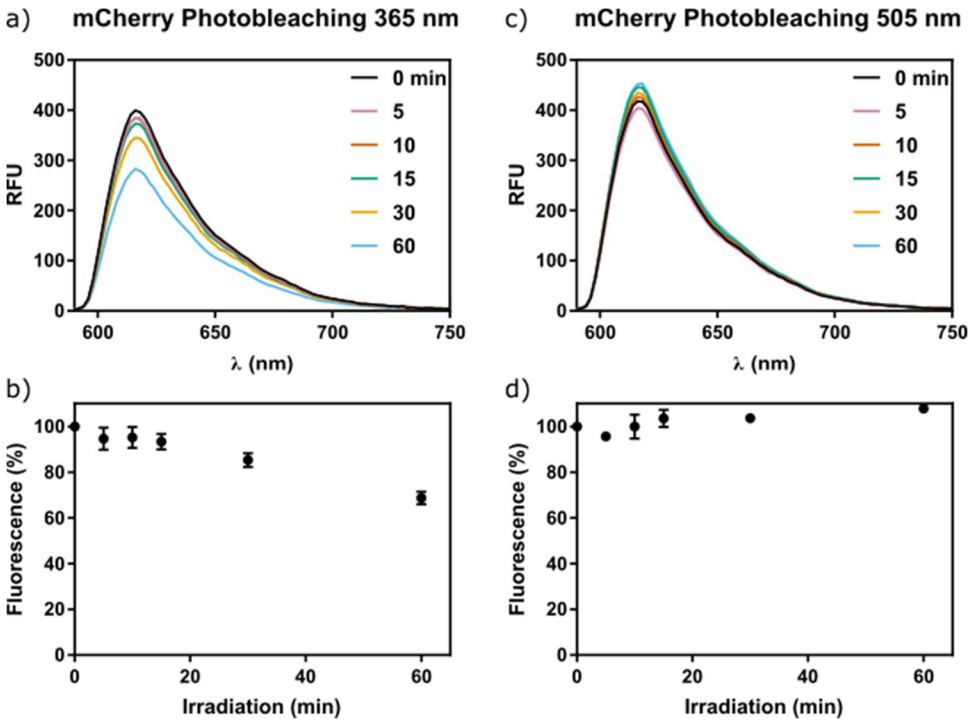

Figure A20. Photobleaching of mCherry at 365 and 505 nm. (a) Fluorescence spectra of mCherry after irradiantion at 365 nm over the course of 60 minutes. (b) Maximum fluorescent intensity of mCherry during 365 nm irradiation. (c) Fluorescence spectra of mCherry after irradiation at 505 nm over the course of 60 minutes. (d) Maximum fluorescent intensity of mCerulean during 505 nm

irradiation. Irradiation under 365 nm lead to a moderate decrease in fluorescent intensity of roughly 30% after a 60 minute exposure. Irradiation under 505 nm lead to a slight increase in fluorescent intensity of roughly 10% after a 60-minute exposure.

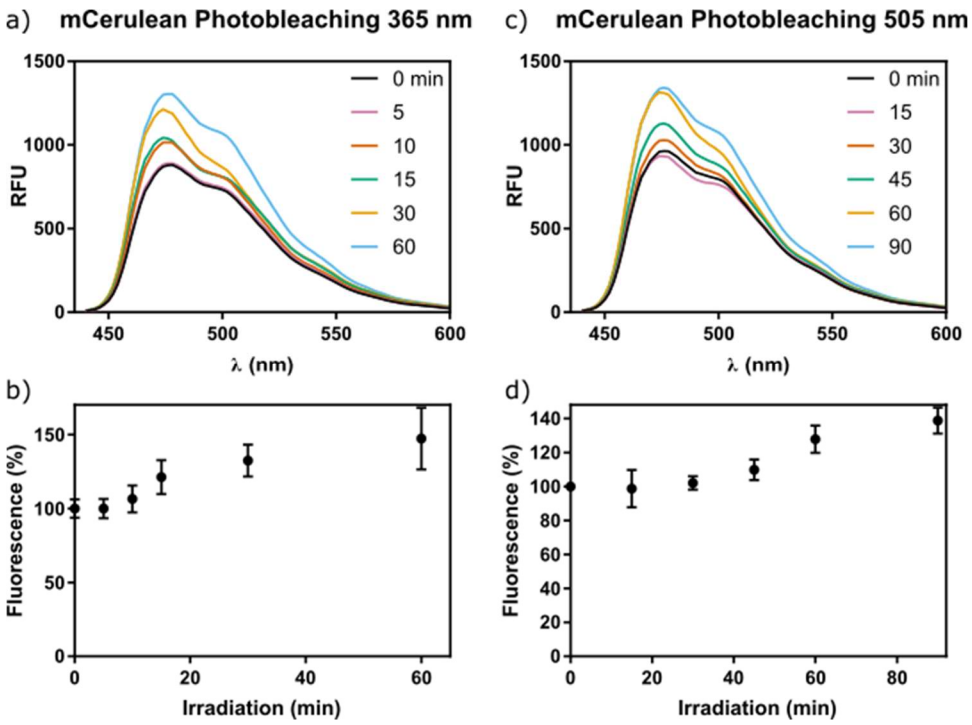

Figure A21. Photobleaching of mCerulean at 365 and 505 nm. (a) Fluorescence spectra of mCerulean after irradiantion at 365 nm over the course of 60 minutes. (b) Maximum fluorescent intensity of mCerulean during 365 nm irradiation. (c) Fluorescence spectra of mCerulean after irradiation at 505 nm over the course of 90 minutes. (d) Maximum fluorescent intensity of mCerulean during 505 nm irradiation. Irradiation under both light conditions led to an increase in fluorescent intensity between 40-50% after 60-minute exposures.

Formation and release from protein-coupled hydrogels

Single-component hydrogels were created containing either BODIPY-mCherry or *o*NB-mCerulean. BODIPY-mCherry [(35 μL, 0.484 mg/mL, 1xPBS) or *o*NB-mCerulean (9 μL, 0.293 mg/mL, 1xPBS)] was added to the PEG-tetraBCN (20 μL, 10 mM, 1xPBS) and allowed to react at room temperature for 1 hour. Next, the diazide-PEG (10 μL, 40 mM, 1xPBS) was added along with additional 1xPBS (mCherry: 0 μL, mCerulean: 26 μL) to provide 10 wt% gels. The gels were formed between two Rain-X® coated glass slides with 1 mm rubber spacers (1.5 hr) before being placed into glass scintillation vials and washed (1xPBS, pH 7.2, 48 hrs) to remove any unbound protein. Photocage-protein coupled hydrogels were then irradiated with light (BODIPY-mCherry:505 nm, 20 mW cm^{-2}, 1 hr; *o*NB-mCerulean: 365 nm, 10 mW cm^{-2}, 4 min) to release protein into the solution. The proteins were allowed to diffuse out of the hydrogels over the next 4 hours and the fluorescence of the solutions was monitored with a spectrophotometer.

Gels containing both BODIPY-mCherry and *o*NB-mCerulean were formed much in the way described above but substituting BODIPY-mCherry for 1xPBS (26 μL) in the mCerulean only gels. Photocage-protein coupled hydrogels were then irradiated with light (505 nm, 20 mW cm^{-2}, 1 hr or 365 nm, 10 mW cm^{-2}, 4 min) to release protein into the solution. The gels were then subjected to additional irradiation with the other wavelength (505 nm then 365 nm or 365 nm then 505 nm) under the same irradiation conditions (505 nm, 20 mW cm^{-2}, 1 hr or 365 nm, 10 mW cm^{-2}, 4 min). The proteins were allowed to diffuse out of the hydrogels over a total of 8 hours and the fluorescence of the solutions was monitored with a spectrophotometer.

It would be advantageous to continue selective release of biomolecules from these materials to continue providing controlled biological cues over an extended period. It was demonstrated that this sequential release process could be extended to a third irradiation event (505 nm, 20 mW cm^{-2}, 1 hr or 365 nm, 10 mW cm^{-2}, 4 min) and the material would continue releasing the corresponding protein (Figure A22). The proteins were allowed to diffuse out of the hydrogels over a total of 12 hours and the fluorescence of the solutions was monitored with a spectrophotometer.

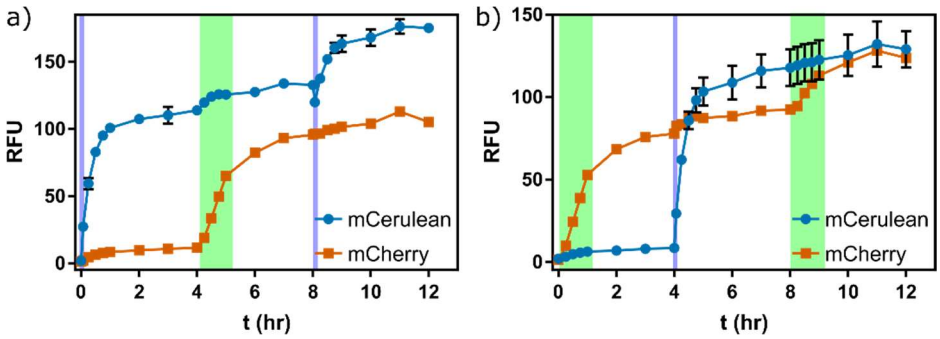

Figure A22. Multiple release of fluorescent proteins from PEG-based hydrogels upon light exposure. (a) and (b) Multiple component gels selectively release the desired fluorescent protein after light irradiation. Subsequent light irradiation selectively releases the other protein from the hydrogel. The system operates as expected irrespective of the light exposure order and can be repeated several times to release additional protein; (a) 365 nm, followed by 505 nm, followed by a final exposure at 365 nm; (d) 505 nm, followed by 365 nm, followed by a final exposure at 505 nm.

Appendix B MATLAB® Code for Photomask Generation

These scripts were developed by Dr. Ivan Batalov (Postdoctoral Research Scholar in the DeForest lab at the University of Washington) with some iteration based on input to facilitate the production of 3D photomasks from biological samples.

The MATLAB® (version 9.6) scripts are divided into 3 sections. The first is for converting a single image into a photomask. A single image, typically used in tissue culture, was generated by collecting a zstack of the cell monolayer and converting it to a single, binary image through a sum of the slices. The second is for converting a zstack image into a series of photomasks, which can be fed directly into the script. The third converts these masks into a region of interest file (ROI) that the Olympus software can read. The scripts below can be pasted directly into MATLAB® and are annotated in **blue** by IB and SMA.

2D photomask

```
%size of the scan field in microscope
area_size_x = 1024; %in pixels
area_size_y = 1024;
laser_power = 100; %percentage laser intensity for all ROIs
sampling_dist = 2; %how many points to skip in the path

%open the original roi file
file_name = 's_261714864-527330.roi'; %this value must be consistent throughout
fileID1 = fopen(file_name,'r', 'n', 'unicode');
roi_template = textscan(fileID1, '%s', 'delimiter', '\n');
roi_template = roi_template{1}; %basic irradiation settings; must match number in line 8
%split the roi file into sections:
%header, reference squares, and the polygon
```

```
n = 0; %number of '2D' encounters
last_i = 1;
for i = 1 : length(roi_template)
        if  strcmp(roi_template{i}, '[2D]')
                switch n
                        case 0 %header
                                header = roi_template(1:i-1);
                        case 1 %first refecence square
                                ref_square_1_part_1 = roi_template(last_i:i-1);
                        case 2 %second reference square
                                ref_square_2_part_1 = roi_template(last_i:i-1);
                        case 3 %polygon to be used as the template for generated polygons
                                poly_template_part_1 = roi_template(last_i:i-1);
                        case 4 %first refecence square
                                ref_square_1_part_2 = roi_template(last_i:i-1);
                        case 5 %second reference square
                                ref_square_2_part_2 = roi_template(last_i:i-1);
                                %the last part goes till the end of the file
                                poly_template_part_2 = roi_template(i:end);
                end
                last_i = i;
                n = n + 1;
        end
end

%open the image, convert to border image
[pic_name, pic_path] = uigetfile({'*.*'; '*.bmp'; '*.png'; '*.tif'; '*.tiff'; '*.jpg'; '*.jpeg'}, 'Open the
binary image');
path_name = pic_path;

% re-run starting from this line if need to readjust image processing
```

```
% parameters
image = imread([pic_path, pic_name]);
image = image/max(image(:));
image = image > 0.2;%apply this threshold
image = image(:,:,1);

%Image processing tools use as needed
%showing the image before processing
figure; imshow(image);

%invert image; 1 is no inversion, 0 is inverted
image = image == 1;

%removing holes up to the size dilate_dist*2 pixels
dilate_dist = 2;
disk = strel('disk', dilate_dist);
image = imdilate(image, disk);
image = imerode(image, disk);

image = imerode(image, disk);
image = imdilate(image, disk);

% shrinking the shapes by shrink_dist pixels
shrink_dist = 1;
shrink_disk = strel('disk', shrink_dist);
image = imerode(image, shrink_disk); %change imerode to imdilate for expansion

% showing the image after the processing
figure; imshow(image);

%find image border
```

```
image_size_x = size(image, 2);
image_size_y = size(image, 1);
max_image_size = max(image_size_x, image_size_y);

traced_border_paths = trace_binary(image);

final_paths = cell(length(traced_border_paths),1);
image_border = zeros(size(image));

for i = 1 : length(traced_border_paths)
        path = traced_border_paths{i};
        path = path(:,1:2);
        temp = [path(2:end,:); path(1,:)];
        repeats = find(max(abs(temp - path), [], 2));
        path = path(repeats,:);
        final_paths{i} = path(:,1:2);
        image_border(sub2ind(size(image), path(:,1), path(:,2))) = 1;
end

%remove empty paths and paths with less than 3 points
final_paths(cellfun(@(x) length(x) <= 2, final_paths)) = [];
%sort paths in the descending order based on the area they enclose
[final_paths, path_colors, paths_inner_pixels] = sort_paths(final_paths, image);

%smooth polygons
sigma = 3;
sz = 20;    %length of gaussFilter vector
x = linspace(-sz / 2, sz / 2, sz);
gaussFilter = exp(-x .^ 2 / (2 * sigma ^ 2));
gaussFilter = gaussFilter / sum (gaussFilter); % normalize
gaussFilter = gaussFilter(:);
```

```
107
108 path_test_image = zeros(size(image));
109 final_overlay = zeros([size(image) 3]);
110 final_overlay(:,:,1) = image_border;
111
112 smoothed_final_paths = cell(size(final_paths));
113 final_paths_for_removal = [];
114
115 for i = 1 : length(final_paths)
116         path = final_paths{i};
117         smoothed_path = imfilter(path, gaussFilter, 'circular');
118         %smoothed_path = path;
119         %for short paths decrease sampling distance to have at least 3 points
120         %in the path
121         curr_smapling_dist = max(1, min(floor(size(smoothed_path, 1)/3), sampling_dist));
122
123         smoothed_path = smoothed_path(1:curr_smapling_dist:end, :);
124
125         % convert row/col to x/y. Fortunately, the microscope considers (0,0) as the top left
126         corner
127         %also, adjust the scale
128         smoothed_final_path = [(smoothed_path(:,2) - 1)*(area_size_x-1)/(max_image_size-1),
129 (smoothed_path(:, 1) - 1)*(area_size_y-1)/(max_image_size-1)];
130         smoothed_final_paths{i} = smoothed_final_path;
131         path_test_image(sub2ind(size(image), round(smoothed_path(:,1)),
132 round(smoothed_path(:,2)))) = 1;
133 end
134
135 final_overlay(:,:,2) = path_test_image;
136 figure; imshow(final_overlay);
137
138 %generate multiphoton file pieces for each path
```

```
roi_text_1 = [];
%header and the first 2 shapes don't need to be modified
roi_text_1 = [roi_text_1, generate_shape_config_text(header)];
roi_text_1 = [roi_text_1, generate_shape_config_text(ref_square_1_part_1)];
roi_text_1 = [roi_text_1, generate_shape_config_text(ref_square_2_part_1)];

shape_number = 2;
for i = 1 : length(final_paths)
        path = smoothed_final_paths{i};
        shape_number = shape_number + 1;
        name_1 = [num2str(shape_number), 'S'];
        text_1 = generate_shape_config_text(poly_template_part_1, 'Name', name_1, 'ID',
name_1, 'LASERPOWER', 100*path_colors(i), 'SHAPE', 8, 'X', path(:, 1), 'Y', path(:,2));
        roi_text_1 = [roi_text_1, text_1];
end

%second piece of text for the ROIs
roi_text_2 = [];
shape_number = shape_number + 1;
name = num2str(shape_number);
roi_text_2 = [roi_text_2, generate_shape_config_text(ref_square_1_part_2, 'Name', name, 'ID',
name)];
shape_number = shape_number + 1;
name = num2str(shape_number);
roi_text_2 = [roi_text_2, generate_shape_config_text(ref_square_2_part_2, 'Name', name, 'ID',
name)];

for i = 1 : length(final_paths)
        path = smoothed_final_paths{i};
        if size(path, 1) > 0
                shape_number = shape_number + 1;
                name_2 = num2str(shape_number);
```

```
171                     text_2 = generate_shape_config_text(poly_template_part_2, 'Name', name_2, 'ID',
172 name_2, 'LASERPOWER', 100*path_colors(i), 'SHAPE', 8, 'X', path(:, 1), 'Y', path(:,2));
173                     roi_text_2 = [roi_text_2, text_2];
174             end
175 end
176
177 %create file for results
178 filename_index = 0;
179 final_file_name = file_name;
180 while(exist([path_name final_file_name], 'file') == 2)
181             filename_index = filename_index + 1;
182             final_file_name = [file_name(1:end-4), '_', num2str(filename_index), '.roi'];
183 end
184
185 fileID = fopen([path_name, final_file_name], 'a');
186 fprintf(fileID, roi_text_1);
187 fprintf(fileID, roi_text_2);
188 fclose(fileID);
189
190 %draw the final path the way it should be seen in multiphoton software
191 %to draw correctly, need to transpose the image to convert (x,y) to (row,col)
192 image_to_show = zeros([area_size_y, area_size_x, 3]);
193 background = imresize(image_border, max(area_size_x, area_size_y)/max_image_size);
194 shape_layer = zeros(area_size_y, area_size_x);
195 image_dims = size(shape_layer);
196 for i = 1 : length(smoothed_final_paths)
197             path = smoothed_final_paths{i};
198             path = round(path);
199             path = [path(:,2), path(:,1)];
200
201     range = [1, area_size_x; 1, area_size_y]; %+ [-1, 1; -1, 1]*padding;
```

```
            [curr_shape, converted_polygon] = draw_path(path+1, 'fill', false, 'range', range,
'fill_color', path_colors(i));
    dim = size(curr_shape);
    inner_px = get_closed_shape_inner_pixels(curr_shape(:,:,2), converted_polygon);

    if ~isempty(inner_px)
        %inner_px = inner_px + image_dims(1)*image_dims(2); % shift linear indices  so they
correspond to the second channel
        shape_layer(inner_px) = path_colors(i);
                    %shape_layer(inner_px) = 1;
    end

            %shape_image = curr_shape(:,:,2);
            %inner_indices = get_closed_shape_inner_pixels(shape_image);
            %[inner_rows, inner_cols] = ind2sub(size(shape_image), inner_indices);
            %new_inner_indices = sub2ind(size(shape_layer), inner_rows, inner_cols);
            %shape_layer(new_inner_indices) = path_colors(i);
            %shape_layer(1:dim(1), 1:dim(2)) = shape_layer(1:dim(1), 1:dim(2)) | curr_shape(:,:,2);

            image_to_show(1:dim(1), 1:dim(2), 3) = image_to_show(1:dim(1), 1:dim(2), 3) |
curr_shape(:,:,3);
end

image_to_show(:,:,2) = shape_layer;
figure; imshow(image_to_show);
```

3D photomask

```
%remove 's_' from file number
final_file_number = '261126096-183770238';
sampling_dist = 1;
```

```
area_size_x = 1024;%in pixels
area_size_y = 1024;
laser_power = 100;%fractional laser intensity for all ROIs

if exist('folder', 'var') && ischar(folder) && exist(folder, 'dir')
        [names, temp_folder] = uigetfile(['*.*'], 'open image', folder, 'multiselect', 'on');
else
        [names, temp_folder] = uigetfile(['*.*'], 'open image', 'multiselect', 'on');
end

if ischar(temp_folder) && exist(temp_folder, 'dir')
        folder = temp_folder;
        full_names = strcat(folder, names);

        if ~isa(full_names, 'cell')
                full_names = {full_names};
        end

        slices = cell(length(full_names),1);
        for i = 1 : length(full_names)
                full_name = full_names{i};
                slice = bfopen(full_name);
                slices{i} = slice;
        end
end

metadata = slices{1}{1,4};
%n_channels = metadata.getChannelCount(0);
stack = double(cat(3, slices{1}{1}{:,1}));

size_X = metadata.getPixelsSizeX(0).getValue();
```

```
size_Y = metadata.getPixelsSizeY(0).getValue();
size_Z = metadata.getPixelsSizeZ(0).getValue();
n_channels = metadata.getPixelsSizeC(0).getValue();

stack = reshape(stack, size_Y, size_X, n_channels, size_Z);
stack = squeeze(stack(:,:,3,:)); %channel number increments from the first used
stack = stack / max(stack(:));
mip = squeeze(max(stack, [], 3));
%figure; imshow(mip/prctile(mip(:), 99.9999999));
thresh = 0.5;%apply this threshold to the image
figure; imshow(mip > thresh);%show the image with the threshold applied

%stack = imgaussfilt(stack, 7);
stack = stack / max(stack(:));

binary_stack = stack > thresh;
implay(binary_stack) %display the sum of the binary images

path_name = [full_names{1}(1:end-4) '_roi_files\'];
if exist([full_names{1}(1:end-4) '_roi_files\'], 'dir')
        folder_index = 1;
        path_name = [full_names{1}(1:end-4) '_roi_files_' num2str(folder_index) '\'];
        while exist(path_name, 'dir')
                folder_index = folder_index + 1;
                path_name = [full_names{1}(1:end-4) '_roi_files_' num2str(folder_index) '\'];
        end
end
mkdir(path_name);

file_generator = olympus_converter();

```

```
final_overlays = zeros(size_Y, size_X, 3, size_Z);

for slice_num = 1 : size(binary_stack,3)
        image = squeeze(binary_stack(:,:,slice_num));
   shrink_distance = 2;
        disk = strel('disk', shrink_distance);
   image = imerode(image, disk);

        max_image_size = max(size_X, size_Y);

        traced_border_paths = trace_binary(image);

        final_paths = cell(length(traced_border_paths),1);
        image_border = zeros(size(image));

        for i = 1 : length(traced_border_paths)
                path = traced_border_paths{i};
                path = path(:,1:2);
                temp = [path(2:end,:); path(1,:)];
                repeats = find(max(abs(temp - path), [], 2));
                path = path(repeats,:);
                final_paths{i} = path(:,1:2);
                image_border(sub2ind(size(image), path(:,1), path(:,2))) = 1;
        end

        %remove empty paths and paths with less than 3 points
        final_paths(cellfun(@(x) length(x) <= 2, final_paths)) = [];
        %sort paths in the descending order based on the area they enclose
        [final_paths, path_colors, paths_inner_pixels] = sort_paths(final_paths, image);

        %smooth polygons
```

```
97          sigma = 0;
98          sz = 20;    %length of gaussFilter vector
99          x = linspace(-sz / 2, sz / 2, sz);
100         if sigma > 0
101                 gaussFilter = exp(-x .^ 2 / (2 * sigma ^ 2));
102                 gaussFilter = gaussFilter / sum (gaussFilter); %normalize
103                 gaussFilter = gaussFilter(:);
104         end
105
106         path_test_image = zeros(size(image));
107         final_overlay = zeros([size(image) 3]);
108         final_overlay(:,:,1) = image_border;
109
110         converted_final_paths = cell(size(final_paths));
111         final_paths_for_removal = [];
112
113         for i = 1 : length(final_paths)
114                 path = final_paths{i};
115
116                 if sigma > 0
117                         path = imfilter(path, gaussFilter, 'circular');
118                 end
119
120                 %smoothed_path = path;
121                 %for short paths decrease sampling distance to have at least 3 points
122                 %in the path
123                 curr_smapling_dist = max(1, min(floor(size(path, 1)/3), sampling_dist));
124
125                 path = path(1:curr_smapling_dist:end, :);
126
```

```
                % convert row/col to x/y. Fortunately, the microscope considers (0,0) as the
                top left corner
                % also, adjust the scale
                smoothed_final_path = [(path(:,2) - 1)*(area_size_x-1)/(max_image_size-1),
(path(:, 1) - 1)*(area_size_y-1)/(max_image_size-1)];
                converted_final_paths{i} = smoothed_final_path;
                path_test_image(sub2ind(size(image), round(path(:,1)), round(path(:,2)))) = 1;
        end

        final_overlay(:,:,2) = path_test_image;
        %figure; imshow(final_overlay);
        final_overlays(:,:,:,slice_num) = final_overlay;

        file_name = sprintf(['s_' final_file_number '_s_%i.roi'], slice_num);

        file_generator.write_microscope_files(converted_final_paths, path_colors, [path_name,
file_name])

        fprintf('slice %i / %i processed.\n', slice_num, size_Z);
end

implay(final_overlays)%display a
```

Olympus conversion

```
classdef olympus_converter

        properties
                laser_power = 100;%for all ROIs
                file_name = 's_261714864-527330.roi';%this number must be consistent
                header = []
```

```
        ref_square_1_part_1 = []
        ref_square_2_part_1 = []
        poly_template_part_1 = []
        ref_square_1_part_2 = []
        ref_square_2_part_2 = []
        poly_template_part_2 = []

    end

    methods
        function obj = olympus_converter(varargin)
            for i = 1 : length(varargin)/2
                switch varargin{2*i-1}
                    case 'template'
                        obj.file_name = varargin{2*i};
                    case 'laser_power'
                        obj.laser_power = varargin{2*i};
                end
            end

            obj = obj.load_files();
        end

        function obj = load_files(obj)
            %open the template roi file

            fileID1 = fopen(obj.file_name,'r', 'n', 'unicode');
            roi_template = textscan(fileID1, '%s', 'delimiter', '\n');
            roi_template = roi_template{1};

            %split the roi file into sections:
```

```
38                          %header, reference squares, and the polygon
39                          n = 0; % number of '2D' encounters
40                          last_i = 1;
41                          for i = 1 : length(roi_template)
42                                  if  strcmp(roi_template{i}, '[2D]')
43                                          switch n
44                                                  case 0 %header
45                                                          obj.header = roi_template(1:i-1);
46                                                  case 1 %first refecence square
47                                                          obj.ref_square_1_part_1 =
48  roi_template(last_i:i-1);
49                                                  case 2 %second reference square
50                                                          obj.ref_square_2_part_1 =
51  roi_template(last_i:i-1);
52                                                  case 3 %polygon to be used as the template for
53  generated polygons
54                                                          obj.poly_template_part_1 =
55  roi_template(last_i:i-1);
56                                                  case 4 %first refecence square
57                                                          obj.ref_square_1_part_2 =
58  roi_template(last_i:i-1);
59                                                  case 5 %second reference square
60                                                          obj.ref_square_2_part_2 =
61  roi_template(last_i:i-1);
62                                                          %the last section is the rest of the file
63                                                          obj.poly_template_part_2 =
64  roi_template(i:end);
65                                          end
66                                          last_i = i;
67                                          n = n + 1;
68                                  end
69                          end
70                  end
```

```
71
72                  function write_microscope_files(obj, paths, path_colors, output_file)
73                      %generate multiphoton file pieces for each path
74                      roi_text_1 = [];
75                      %header and the first 2 shapes don't need to be modified
76                      roi_text_1 = [roi_text_1, generate_shape_config_text(obj.header)];
77                      roi_text_1 = [roi_text_1,
78  generate_shape_config_text(obj.ref_square_1_part_1)];
79                      roi_text_1 = [roi_text_1,
80  generate_shape_config_text(obj.ref_square_2_part_1)];
81                      shape_number = 2;
82                      for i = 1 : length(paths)
83                          path = paths{i};
84                          shape_number = shape_number + 1;
85                          name_1 = [num2str(shape_number), 'S'];
86                          text_1 = generate_shape_config_text(obj.poly_template_part_1,
87  'Name', name_1, 'ID', name_1, 'LASERPOWER', 100*path_colors(i), 'SHAPE', 8, 'X', path(:, 1),
88  'Y', path(:,2));
89                          roi_text_1 = [roi_text_1, text_1];
90                      end
91
92                      %second piece of text for the ROIs
93                      roi_text_2 = [];
94                      shape_number = shape_number + 1;
95                      name = num2str(shape_number);
96                      roi_text_2 = [roi_text_2,
97  generate_shape_config_text(obj.ref_square_1_part_2, 'Name', name, 'ID', name)];
98                      shape_number = shape_number + 1;
99                      name = num2str(shape_number);
100                     roi_text_2 = [roi_text_2,
101 generate_shape_config_text(obj.ref_square_2_part_2, 'Name', name, 'ID', name)];
102
103                     for i = 1 : length(paths)
```

```
104                                     path = paths{i};
105                                     if size(path, 1) > 0
106                                             shape_number = shape_number + 1;
107                                             name_2 = num2str(shape_number);
108                                             text_2 =
109 generate_shape_config_text(obj.poly_template_part_2, 'Name', name_2, 'ID', name_2,
110 'LASERPOWER', 100*path_colors(i), 'SHAPE', 8, 'X', path(:, 1), 'Y', path(:,2));
111                                             roi_text_2 = [roi_text_2, text_2];
112                                     end
113                             end
114
115                             %create file for results
116                             filename_index = 0;
117                             final_file_name = output_file;
118                             while(exist(final_file_name, 'file') == 2)
119                                     filename_index = filename_index + 1;
120                                     final_file_name = strjoin([output_file(1:end-4), '_',
121 num2str(filename_index), '.roi'], '');
122                             end
123
124                             fileID = fopen(final_file_name, 'a');
125                             fprintf(fileID, roi_text_1);
126                             fprintf(fileID, roi_text_2);
127                             fclose(fileID);
128                     end
129             end
130 end
```

Vita

Soon after starting his undergraduate degree at Washington State University, Steven Adelmund discovered his passion for chemistry and teaching. It was there that, with little supervision, he explored the chemistry laboratory under the guise of creating new curriculum for the organic chemistry courses. He made many mistakes, but he learned from them. After moving to Louisiana to serve in the U.S Air Force, he found himself with decidedly too much free time, so what began as a volunteering engagement in the chemistry lab quickly became a master's program in biological science. He quickly discovered that his earlier distaste for biology had been misplaced. In fact, chemistry and biology, it seemed, were just two sides of the same coin. Bridging these two ostensibly disparate worlds became a major feature of his research while pursuing his doctorate at the University of Washington. Fortunately for Steve his advisor, Cole DeForest, provided him wide latitude to explore these realms. Eventually, his endeavors bore fruit, the results of which are presented here. In the future, Steve promises to use his powers for good, to the benefit of humanity.